AD-A187 266   PRELIMINARY STUDIES FOR A DRILLING ROBOT FIREFIGHTER   1/2
(U) NAVAL POSTGRADUATE SCHOOL MONTEREY CA
D L SMITH ET AL. 01 SEP 87 NPS-69-87-005

UNCLASSIFIED   F/G 13/12   NL
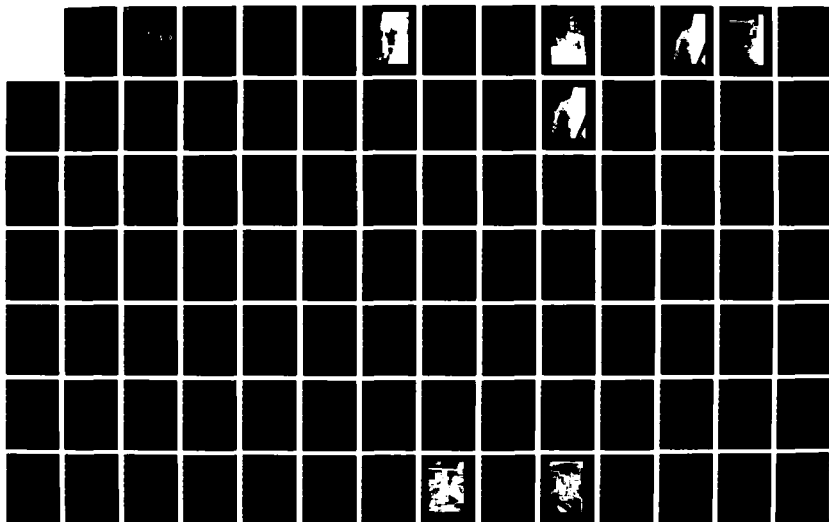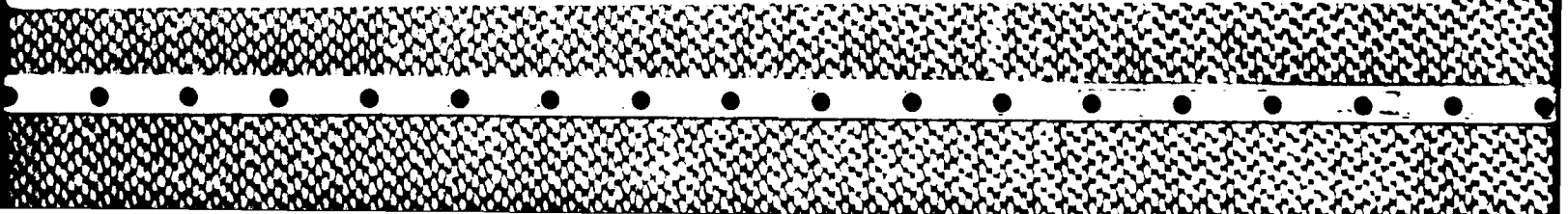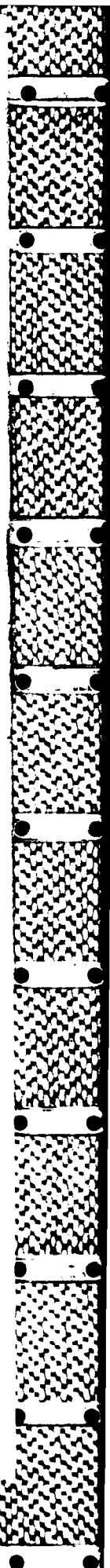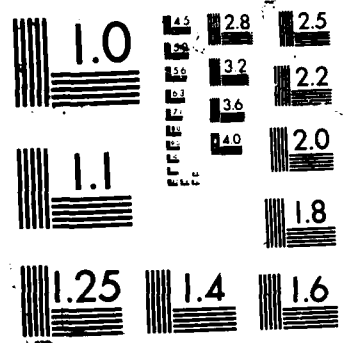
②

NPS 69-87-005

AD-A187 266

NAVAL POSTGRADUATE SCHOOL
Monterey, California

DTIC
ELECTE
JAN 0 4 1988
S
H
D

PRELIMINARY STUDIES FOR A
DRILLING ROBOT FIREFIGHTER

by

D.L. Smith
J.P. Harris
D.A. Lawrence

August 1987

Approved for Public Release; Distribution Unlimited

87 12 22 036

REPORT DOCUMENTATION PAGE

1a REPORT SECURITY CLASSIFICATION	1b RESTRICTIVE MARKINGS
UNCLASSIFIED	

2a SECURITY CLASSIFICATION AUTHORITY	3 DISTRIBUTION/AVAILABILITY OF REPORT
2b DECLASSIFICATION/DOWNGRADING SCHEDULE	Approved for public release; distribution is unlimited.

4 PERFORMING ORGANIZATION REPORT NUMBER(S)	5 MONITORING ORGANIZATION REPORT NUMBER(S)
NPS 69-87-005	

6a NAME OF PERFORMING ORGANIZATION	6b OFFICE SYMBOL (If applicable)	7a. NAME OF MONITORING ORGANIZATION
Naval Postgraduate School	Code 69Sm	Naval Surface Weapons Center

6c ADDRESS (City, State, and ZIP Code)	7b. ADDRESS (City, State, and ZIP Code)
Monterey, CA 93943	10901 New Hampshire Ave. Silver Spring, MD 20903-5000

8a. NAME OF FUNDING/SPONSORING ORGANIZATION	8b OFFICE SYMBOL (If applicable)	9 PROCUREMENT INSTRUMENT IDENTIFICATION NUMBER
Naval Surface Weapons Ctr	Code R402	

8c. ADDRESS (City, State, and ZIP Code)	10 SOURCE OF FUNDING NUMBERS			
	PROGRAM ELEMENT NO	PROJECT NO	TASK NO	WORK UNIT ACCESSION NO
White Oak Silver Spring, MD 20910	6326ZN		S1819	

11 TITLE (Include Security Classification)

Preliminary studies for a Drilling Robot Firefighter

12 PERSONAL AUTHOR(S) Smith, D.L., Harris, J.P., Lawrence, D.A.

13a TYPE OF REPORT	13b TIME COVERED	14 DATE OF REPORT (Year, Month, Day)	15 PAGE COUNT
Final	FROM Jan 85 TO Aug87	87 Sept. 01	

16 SUPPLEMENTARY NOTATION

COSATI CODES			18 SUBJECT TERMS (Continue on reverse if necessary and identify by block number)
FIELD	GROUP	SUB-GROUP	Firefighting, Robotics, Drilling Machines, Drills

19 ABSTRACT (Continue on reverse if necessary and identify by block number)

The USAF has produced a firefighter's drill to be used for aircraft fires. This report describes preliminary studies which were conducted to establish a data base for the design of a robotic manipulator for the drill. The loads associated with drilling of aircraft skins are measured and characterized. Link flexibility effects are studied and manipulator modeling and control issues are identified. Keywords:

20 DISTRIBUTION/AVAILABILITY OF ABSTRACT	21 ABSTRACT SECURITY CLASSIFICATION
☒ UNCLASSIFIED/UNLIMITED ☐ SAME AS RPT ☐ DTIC USERS	UNCLASSIFIED

22a NAME OF RESPONSIBLE INDIVIDUAL	22b TELEPHONE (Include Area Code)	22c OFFICE SYMBOL
David L. Smith	(408) 646-3383	Code 69Sm

DD FORM 1473, 84 MAR 83 APR edition may be used until exhausted
All other editions are obsolete

Table of Contents

I. Introduction

The NSWC Firefighter Project was aimed at demonstration of a Remotely Controlled Firefighting Platform (RCFP). This goal was achieved in April of 1987. Upon review of larger NSWC objectives, NSWC decided to cancel further work on the RCFP in September 1987. Nevertheless, while the RCFP program was operating, a preliminary effort was also conducted at the NPS to develop a data base for a supplemental, more autonomous firefighting vehicle. The NPS project concept was to evaluate design options for autonomously manipulating a firefighting tool which was previously designed by the USAF (Fig. 1). The air powered tool shown on its "H" support bracket in Figure 1 was designed to drill through the fuselage of an aircraft in order to pump inerting gas into the interior through a hollow drill bit. However, it was also designed to be hand-held, thus exposing the human operator to great risk from burning fuel or ordance. Consequently, the design of a more-or-less autonomous manipulator for the USAF tool seemed like a viable concept and the NPS research effort was stared.

An unfunded, unofficial NPS/NSWC Robotic Firefighter Project was begun in Jan 1985 at the encouragement of Mr. Russ Werneth of NSWC and LCDR Bart Everett, then of NAVSEA 90G. The project was initiated by directing an existing NPS Research Foundation program on optimal control into these applicational lines of investigation. It was fostered as the ME Department successfully strengthened the supportive course work in the Dynamic Systems and Controls specialty area. It was developed through a large student interest (11 student theses) in a wide variety of pertinent fundamental problem areas. Shortly after the unofficial project beginning, Ms. Mary Lacey of NSWC responded with the funded support discussed in the front matter and her personal encouragement and advice.

1
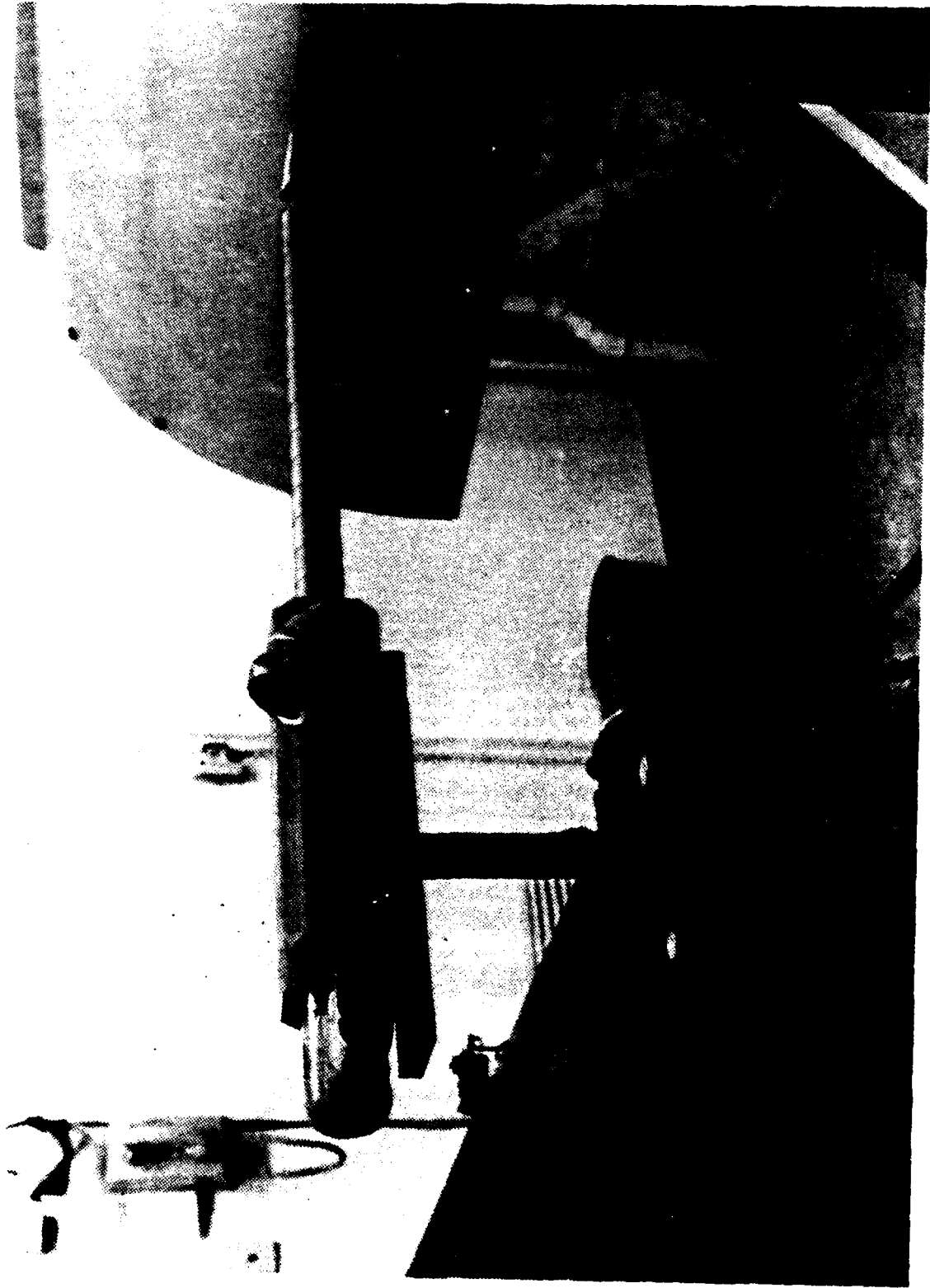
Figure 1. USAF Firefighters Drill.

The autonomous firefighter manipulation problem has two main areas: design of a manipulator mechanism and controller design for that mechanism. In addressing these problem areas the following assumptions were made:

1. The manipulator must manipulate the USAF tool shown in Figure 1.

2. The manipulator must be as autonomous as possible.

3. Due to (2), the maniplator must be as power efficient as possible in order to conserve on-board power supplies.

4. The tool positioning requirement would be approximately $\pm$ 0.10 in and $\pm$ 5 deg at the drill tip.

The mechanism design must first be concerned with the expected loads associated with the drilling process. Since these are, in general, widely variable depending on the type of drill, type of material to be drilled, incidence angle, reinforcements, and many other parameters, we were not surprized to find very litle published material on the drilling process in the open literature. To remedy this we undertook several experimental projects to measure and characterize the particular process of drilling aircraft skins. Given the measured drilling load characteristics, the manipulator mechanism and actuators could be designed or selected.

The manipulator controller is concerned with guiding the manipulator from point-to-point in a power efficient manner, and maintaining a tool orientation while a hole is drilled. The following discussion is about the first part of the controller problem, the point-to-point control and the tasks associated with solving this problem. Clearly, the manipulation requirements outlined in assumption 4 above could not be considered high performance specifications. Instead, the controller of interest was one aimed at effective coordination of movement and was therefore called a low performance controller.

3

The remainder of this report is divided into three sections: the next section summarizes the major results acheived to data; the following section describes the most recent mainpulator controller development project; the last section discusses final drilling load measurement studies.

II. Results

A. Facilities Developed

Perhaps the most important facility that has been developed for this project is the Low Performance Control (LPC) Lab. This test bed facility consists of a computer based controller system designed to be used to investigate the merits of various candidate controller and sensor philosophies for low performance plants. The next section of this report describes the LPC Lab in more detail when coupled to a manipulator so it will only be mentioned briefly here. The Lab presently consists of an IBM PC-AT connected to a rigid, revolute robot (Neptune by Alan Hayes Corp.). The Computer/manipulator interaction is accomplished via LABPAC hardware and software. In addition, hardware for optical encoding of joint data, and an improved data taking and display system, including direct memory access, will be purchased and installed in the next few months. This facility has been, and will be, a valuable and necessary tool for research into computer based control of low performance machinery at the Naval Postgraduate School.

The LPC testbed is shown in Figure 2. The Controller (IBM PC-AT) is at the left in the figure, the Data System (IBM PC-XT) is at the right, and the external patch rack is in the center. The Data system can be run independently of the controller to generate plant modeling data, or the Data System and the controller can be run simultaneously through a XENIX

4

Figure 2. Computers For the Low Performance Control Lab.

5

operating system. Maximum bandwidth is about 100 Hz for single input single output operation.

The Neptune manipulator is shown in Figure 3 mounted on its support stand. The hydraulic pump is to the right of the stand, the hydraulic accumulator is beneath the stand, and the bottom shelf holds the valves and a hydraulic manifold. The manipulator has six revolute degrees of freedom, operates on a water based fluid at 120 psig, and can be configured for solenoid ar servovalue operation.

Besides the LPC Lab, two more or less temporary experimental facilities have developed out of the NPS Robot Firefighter Project, these are the drilling apparatus and the flexible link facility. Key features of the drilling apparatus were shown in Figure 1. The USAF drill was mounted on an "H" mounting and afixed to a movable milling bed platform. The vertical support in the "H" mounting was a steel cylinder of 1 inch diameter which was instrumented for strain in order to estimate the loads incurred by the drillnig process. The use and analysis of the drilling apparatus is described in detail in Section IV of this report.

The flexible link facility is shown in Figure 4. The facility consists of a hydraulic pressure source (2000 psig, shown at left), a support platform and control box shown at the center, a one degree of freedom hydraulic motor actuator at right, and a flexible box beam shown vertically upwards. The beam was designed to flex in one plane only in order to study distributed dynamic structural flexibility. This facility was designed and implemented based upon our desire to use the firefighter mechanism to accomplish a range of tasks-expecially the heavy lifting associated with manipulating bombs, rockets, or large aircraft parts. Consequently, if the mechanism is not to become ridiculously bulky and

6
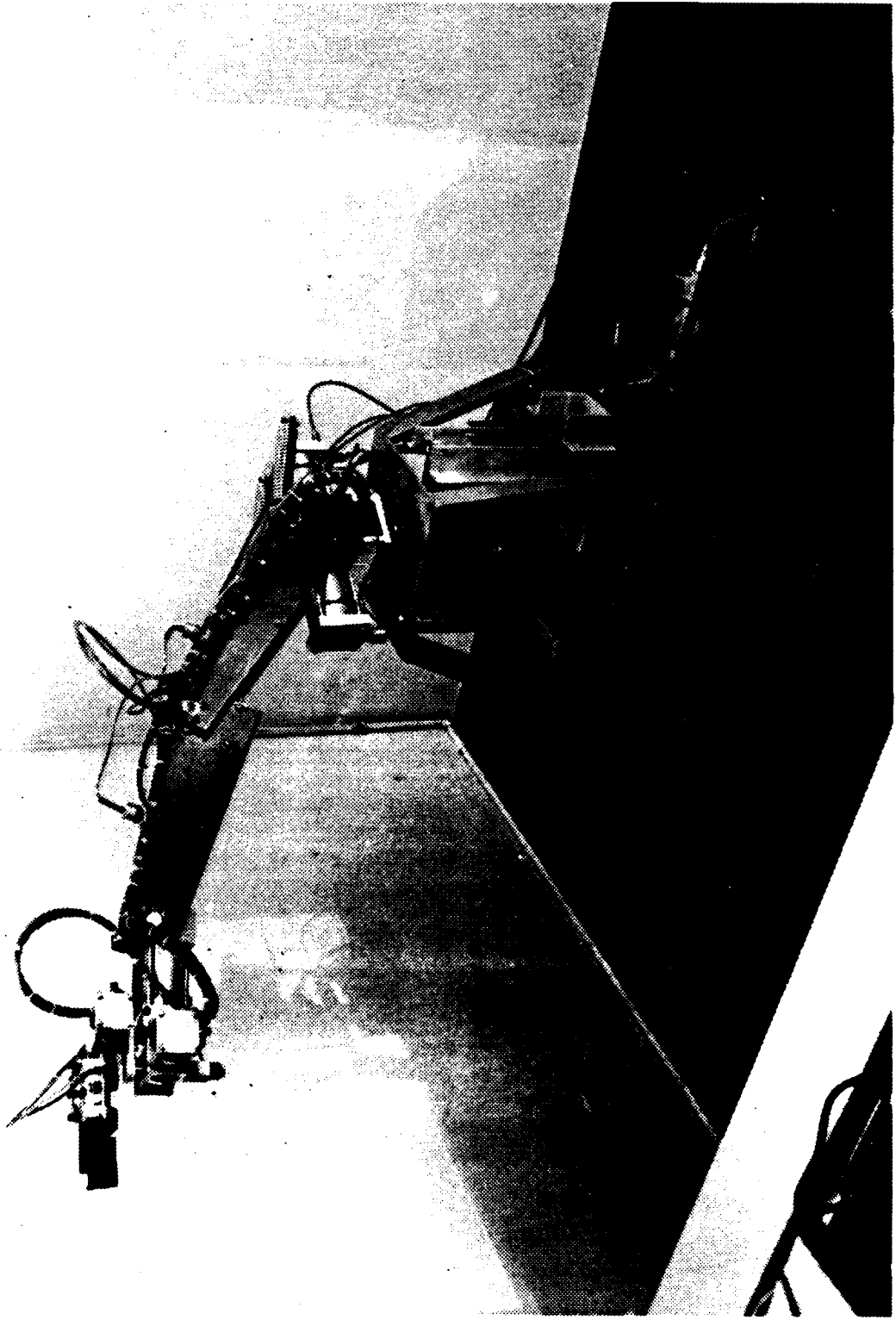
Figure 3. The Neptune Manipulator
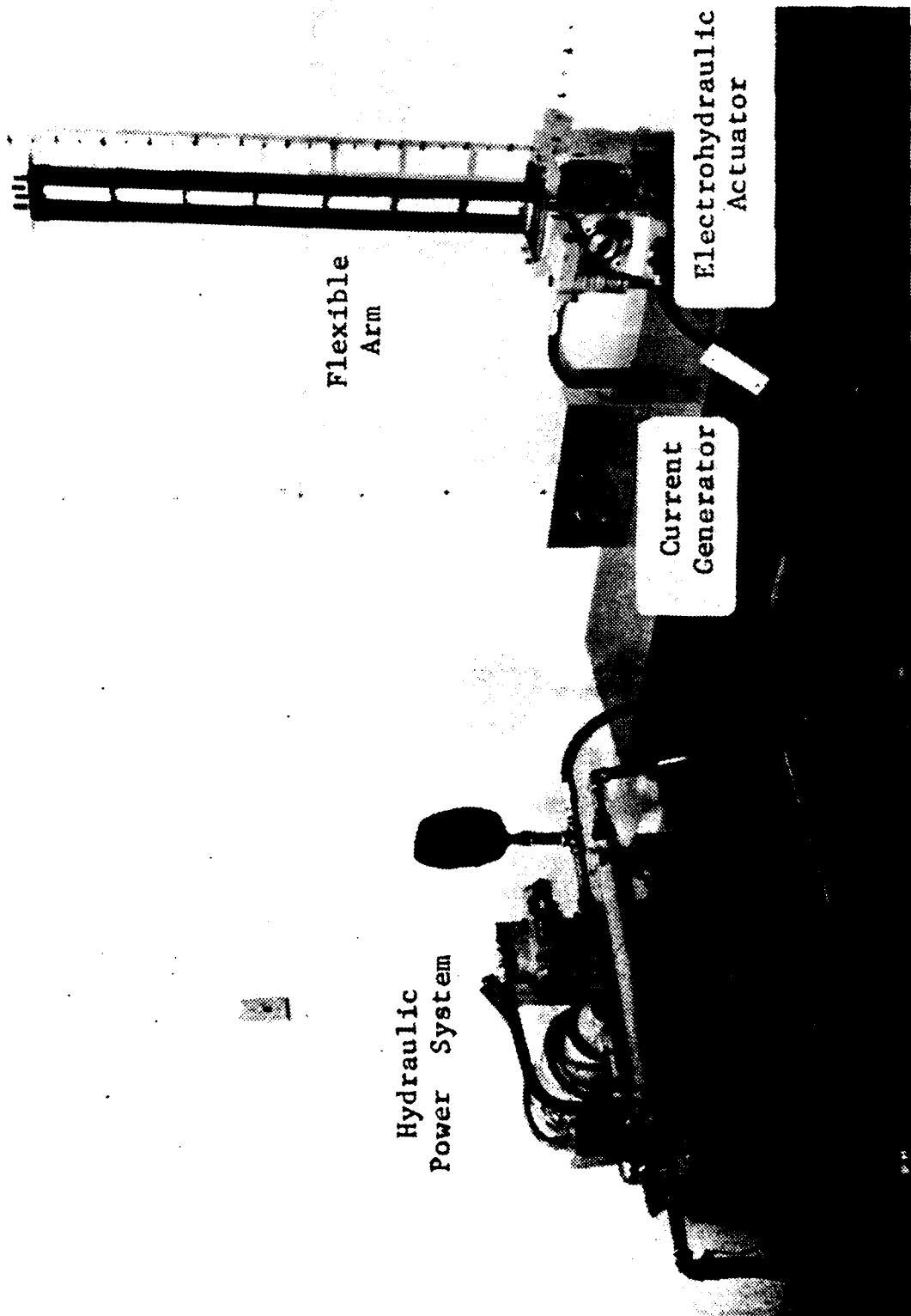
Figure 4. The Flexible Link Facility.

heavy, it can be expected to be flexible; that is, it should be designed to be flexible. Such a flexible mechanism poses interesting problems in terms of modelling and control. Much of what we have learned in the flexible link studies is being incorporated into space-based manipulator analysis at the time of this writing.

B. Major Conclusions

The conclusions which follow are referenced to the theses in which they were first mentioned. The theses are listed in the next portion of this report.

1. Manipulator Design for the USAF Drill

(a) Drill walking at the inception of drilling can lead to large lateral forces and corresponding twisting moments being exerted on the manipulator support structure (Lawrence). This can be largely avoided by pilot hole drilling or drill tip redesign.

(b) Manipulator load forces vary significcnatly as the drill tip wears (Lawrence). Design of the manipulator must account for the worst case to be expected. At some point the drill becomes so worn that it is unable to penetrate the skin (Yobs). A means for sensing the onset of this condition should be provided in the system design and utilization.

(c) The drill tip loads have been characterized for both the worn drill (Yobs) and the new drill (Lawrence). Dynamic and peak loads have been measured. This data will allow the subsequent design of mechanism and acutator components for a drill manipulator.

(d) Flexibility effects are difficult to predict and measure (Petroka). This conclusion suggests that two manipulators may be a good idea: one being ridid, low powered, and low performance to

9

manipulate lightweight tools such as the USAF drill; and one being strong, high powered, and perhaps high performance to manipulate heavy objects. The strong manipulator may be flexible and would, consequently, require a very sophisticated control system, perhaps even a vision-based controller.

2. Rigid Manipulator Modeling

    (a) Simulation of robot motions should be done in global coordinates to avoid singularity problems associated with local, or joint coordinate formulations (McCarthy). Such global simulations are easier to formulate and understand than local, recursive forms (Mohammed).

    (b) For motions less than 30 degrees, the Neptune robot appears to be a very nearly linear machine (Harris, Lewis). This result has strong implications in the design of controllers for low speed manipulators such as the Neptune.

3. Rigid Manpulator Control

    (a) The USAF drill should not be used at incidence angles greater than about 12 degrees from the local normal, or at locations which are supported by stiffners beneath the skin (Yobs).

    (b) Optimal Control (LQR) has been demonstrated as an appropriate means of achieving effective coordinated control of rigid link motions (Harris).

C. Thesis Advised

1. McGalliard, G. R., "A General Simulation Program for Robot Manipulator Arm Dynamics," NPS MSME Thesis, Sept. 1984.

2. MaCarthy, W. F., "Simulation of High Speed Motion of Rigid, Revolute Mechanisms," NPS MSME Thesis, Dec. 1985.

10

3. Lewis, D. R., "Modelling of a Low Performance Rigid Revolute Robot Arm," NPS MSME Thesis, Dec. 1985.

4. Yobs, R. L., "Manipulator Load Forces for a Robotic Firefighter," NPS MSME Thesis, Mar. 1986.

5. Petroka, R. P., "Computer Simulation and Experimental Validation of a Dynamic Model (Equivalent Rigid Link System) on a Single-Link Flexible Manipulator," NPS MSME Thesis, June 1986.

6. Burrill, L. D., "A Feasibility Investigation for Optimal Robotic Control," NPS MSME Thesis, Sept. 1986.

7. Mohammed, K., "Non-Singular Modelling of Rigid Manipulators," NPS MSME Thesis, Dec. 1986.

8. Harris, J. P., "Investigation and Development of a Micro-computer Based Robotic Controller," NPS MSME Thesis, June 1987.

D. Theses in Progress

1. Sanders, D., "Optimal Control as an Autonomous Vehicle Path Planner," NPS MSME Thesis, Dec. 1987 (expected).

2. Fancher, C., "Microcomputer Based Optimal Control for a Low Performance Manipulator," NPS MSME Thesis, Dec. 1987 (expected).

3. Altinok, S., "Non-Singular Simulation of Rigid Manipulator Motions," NPS MSME Thesis, Dec. 1987 (expected).

Section III

Investigation and Development of a

Micro-Computer Based Robotic Controller

TABLE OF CONTENTS

TABLE OF VARIABLES

A,B	--	Linear plant model matrices
c	--	θ - flowrate conversion coefficient
d_1,d_2	--	Manipulator link length to center of gravity
g	--	Gravity constant
h	--	Discrete time step
J_1,J_2	--	Manipulator link inertias
J,J_1,J_2	--	Merit function
k	--	Valve constant
K	--	Control gain matrix
l_1,l_2	--	Manipulator link lengths
m_1,m_2	--	Manipulator link masses
M_s	--	Return spring moment
P_r	--	Return pressure
P_s	--	Supply pressure
P_1,P_2	--	Actuator cylinder pressures
P	--	Real symmetric matrix (Riccati matrix equation)
q	--	Fluid flowrate
Q	--	State weighting matrix
R	--	Input weighting matrix
T,T_1,T_2	--	Joint torques
u	--	Input matrix
U_1,U_2	--	System inputs
v,v_1,v_2	--	Servovalve input voltages
x	--	State matrix
β_1,β_2	--	Joint friction coefficients
ϕ	--	Discrete plant matrix
Γ,Γ_0,Γ_1	--	Discrete plant matrices
λ	--	Scalar factor
Ω	--	Servovalve electrical resistance
Θ,Θ_1,Θ_2	--	Joint positions
$\dot{\Theta},\dot{\Theta}_1,\dot{\Theta}_2$	--	Joint velocities
τ	--	Time delay

situations. Deep submergence undersea exploration vehicles, unexploded munitions disposal units and carrier flight deck firefighting have stood out as examples of jobs that could be taken over by robots with the goal of reducing the risk to human life [Refs. 1,2,3]. In the area of shipboard fires, it was realized that a motorized firefighting unit cannot replace a complete firefighting team, but a quick reaction vehicle could provide intial fire suppression and quite possibly keep the fire from spreading out of control [Ref. 1]. Additionally, the vehicle could be sent into areas where the fear of either ammunition or fuel explosion would prohibit a firefighting team from entering.

The design and operation of a control system for such a robotic device is one area that has recently come under renewed scrutiny [Ref. 2]. The majority of all robots available today use a somewhat large and immobile computer as the master "brain". These large computers are needed to handle voluminous calculations that are demanded by the complex control algorithms for multiple robot manipulator links. In light of their sheer size however, these systems are a poor choice for mobile operations. A more suitable choice is a micro-computer based controller. Due primarily to increases in speed and computational power, "personal computers" (PC's) and the micro-processors that drive them, have been thrust into the limelight as the bridge to the self-contained robot operations.

The first goal of controller development is the selection of the algorithm that will provide adequate system performance. Because cost is a major factor in most operations, an ideally suited controller should minimize the power required to conduct an operation while balancing   this   against   the

I. INTRODUCTION

Robotics, only recently considered science fiction, has now become a permanent part of technology. Although the term "robot" is often misinterpreted, robotic type devices can now be found in all aspects of society, from personal toys, to an integral part of many major manufacturing industries. For the purpose of this paper, a robot is defined as a self contained electro-mechanical system consisting of: a digital controller, a power source, and a manipulator arm.

The advantages of using machines to replace man have long been appreciated. In industry, economics has driven the incorporation of this new technology to accomodate and sometimes replace older methods. The resulting automation has markedly boosted output while decreasing the per unit manpower costs. This has in turn caused an overall increase in production efficiency making many items more affordable to the consumer. Another advantage of automation has been the attainment of more consistent results. Painted items thus become more uniform, machined items become more exact, and production quality becomes more standard from item to item. All of these facts not withstanding, however, the most important reason for the use of mechanical equipment is to lessen the endangerment to man while operating in hazardous environments. The more autonomous the robotic devices, the more removed and hence safer the person controlling the mechanism.

Recently, the U.S. Navy has developed an interest in the use of robots with an aim toward replacing humans in potentially life threatening

positional error generated by the control system. To accomplish this, a modern controller should be investigated for implementation. Such modern controllers are capable of coordinating multiple joint inputs to control the complicated manipulator output configuration. The proof of these controllers lies in their ability to control a real piece of hardware.

This thesis describes the implementation of a modern controller on the Naval Postgraduate School manipulator control test bed. The test bed consists of: a NEPTUNE multiple rigid link robot system (Fig. 1), an IBM PC-AT micro-computer, and two Atchley jet pipe electro-hydraulic servovalves. The NEPTUNE system was modified so that it could be run as originally purchased (solenoid operation), or through a PC based servo controller in order to demonstrate the comparative performance associated with each type of controller.
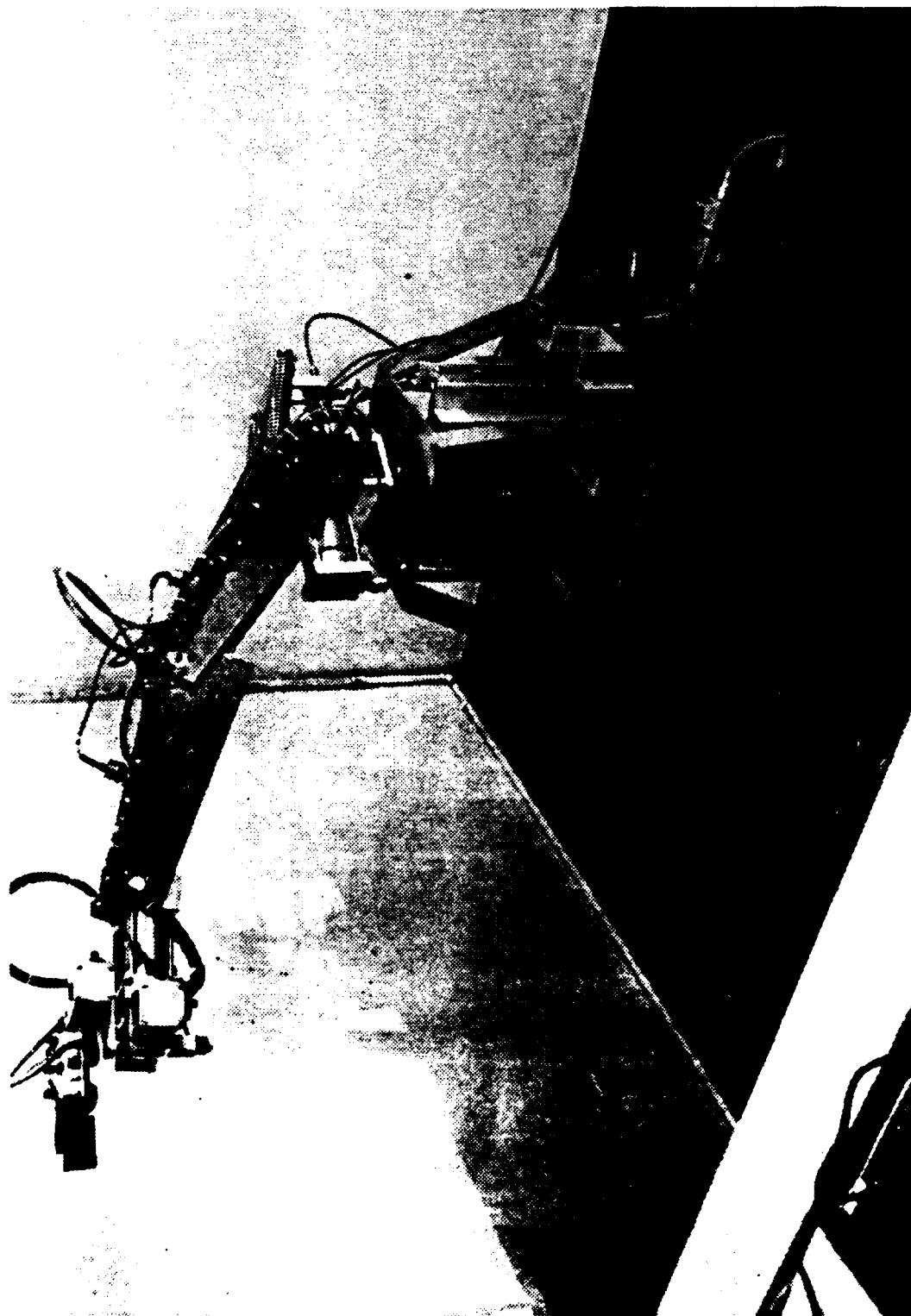
Figure 1
NEPTUNE Manipulator

19

II. BACKGROUND/PROBLEM DESCRIPTION

The primary goal of this work was to initiate an NPS test bed system for Navy development of robotic controllers. The fact that operational robots will be needed to operate in a hostile environment suggests that water based actuators be used as the prime motive force. The NEPTUNE robot arm and control system fit this requirement and were previously selected [Ref. 4]as the system nucleus. Lewis [Ref.4] described the operation of the basic computer/solenoid controlled assembly which was modified in the present investigation.

In the original NEPTUNE actuation scheme, a pseudo-proportional control was obtained through the use of several fluid restrictors (Fig. 2). By
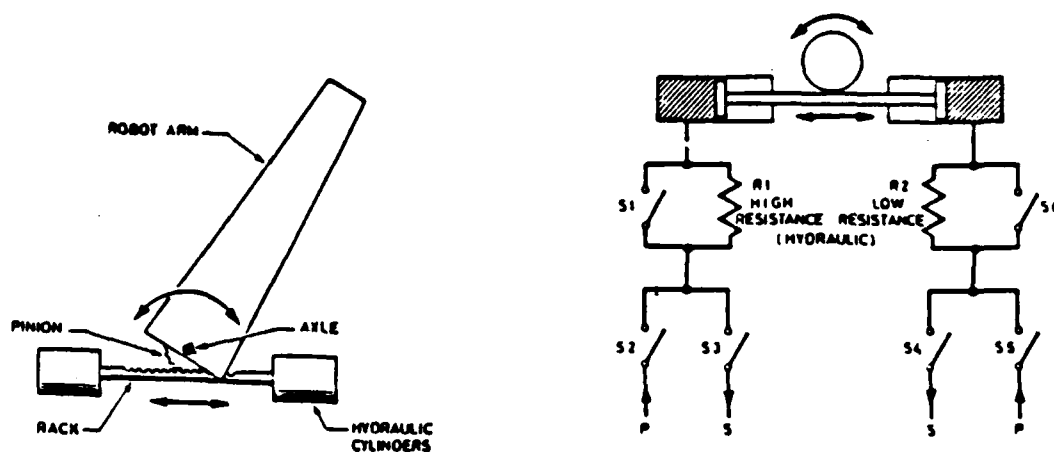
Figure 2

Solenoid hydraulic system

ganging more than one of these restrictors together on a joint, the motion and flow rate history as seen in Figure 3 was acheived. However, in order to investigate advanced servo controls, an infinitely variable flow rate is required as in Figure 4. In order to modify the NEPTUNE to accept a servo
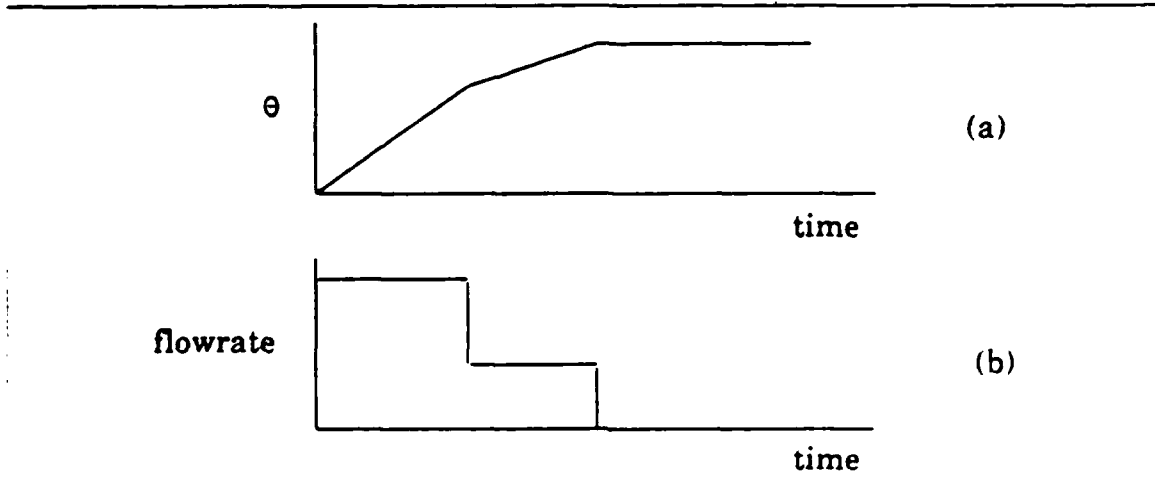
Figure 3
Solenoid operation. (a) motion. (b) flowrate history.
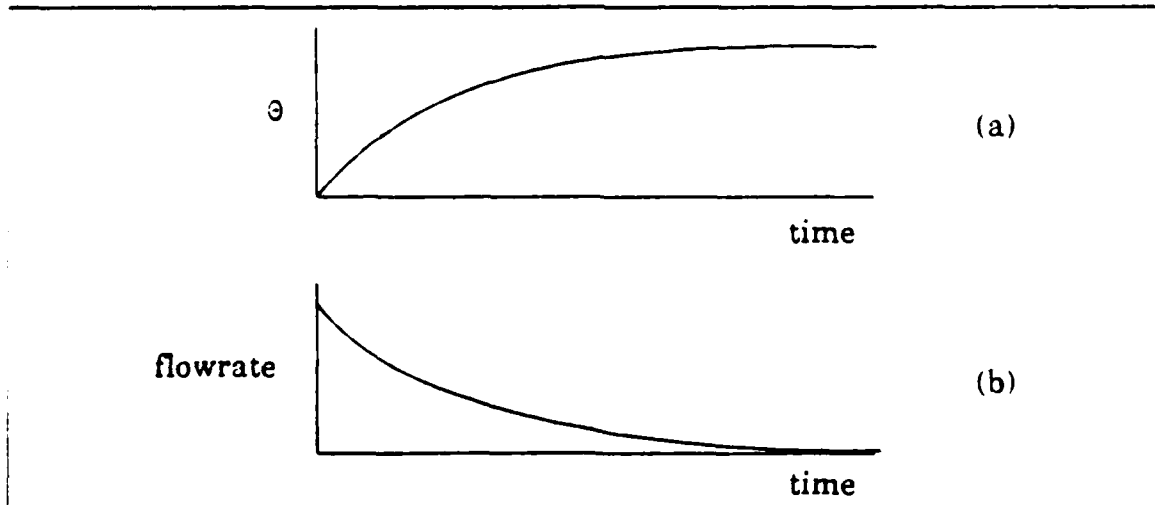
Figure 4
Servo valve operation. (a) motion. (b) flowrate history

control signal, Burrill [Ref. 5] conducted a feasibility study to determine the plant requirements and select the best suited servo valve. "Off the shelf" valves were desired to both minimize the initial procurement costs, and also to standardize the system components with those generally available to industry. The Atchley model 218 jet pipe servo valve was selected, and two valves were placed in service. Because only two dimensional control was to be demonstrated, axes 1 and 2 were chosen (Fig. 5).
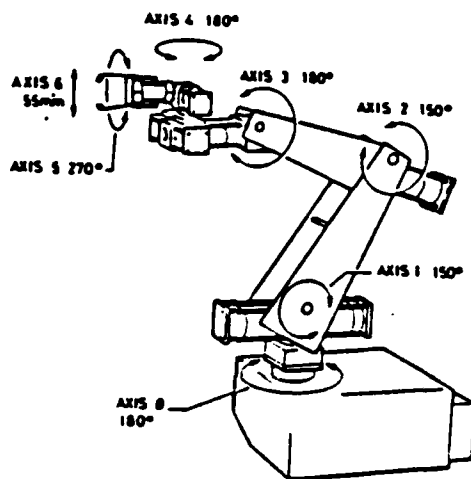

Figure 5
NEPTUNE axes of rotation

An initial hardware modification was required to improve hydraulic system operation. To provide a reservoir of fluid energy, the NEPTUNE hydraulic power pack comes with a 42 cubic inch air bladder accumulator. In order to reduce entrained air in the water-based operating fluid, an air bladder in the accumulator is filled to approximately 55 psi, or one half of system operating pressure. The fluid pump then fills the accumulator and

shuts off at 110 psi. As fluid is drawn down in an arm move, an unloading valve monitors the pressure and automatically turns the pump on at approximately 100 psi. With two joints being operated simultaneously, pump pressure waves can be observed in the actuator cylinder data. This effect was difficult to predict and evaluate.

To alleviate this problem, joints one and two cylinder dimensional measurements were taken, and the maximum amount of fluid needed to move both actuators was calculated. It was determined that approximately 36 cubic inches of fluid was needed to move both actuators the length of their travel. A 580 cubic inch accumulator was fitted such that less than 10 percent of the total volume would be used on any arbitrary move. The resulting cylinder pressure data was much more well behaved.

At this point some clarifications should be made as to the distinction between the plant and controller as described by this research. Figure 6 shows the general multi-port layout with the term system defined as the combination of the computer, both servovalves, and their associated links. The term plant refers to the arm and servovalve combination. Although not a radical departure from conventional thinking, the inclusion of the servovalve in the plant block instead of the controller block could be considered unusual. There were two reasons for taking this approach. First, the plant is normally considered as that part of the system that is, for one reason or another, already selected, unchangeable and must be controlled. Secondly, as will be discussed later, the dynamic characteristics of the links when combined with the hydraulic characteristics of the valves allows a simple yet effective modeling
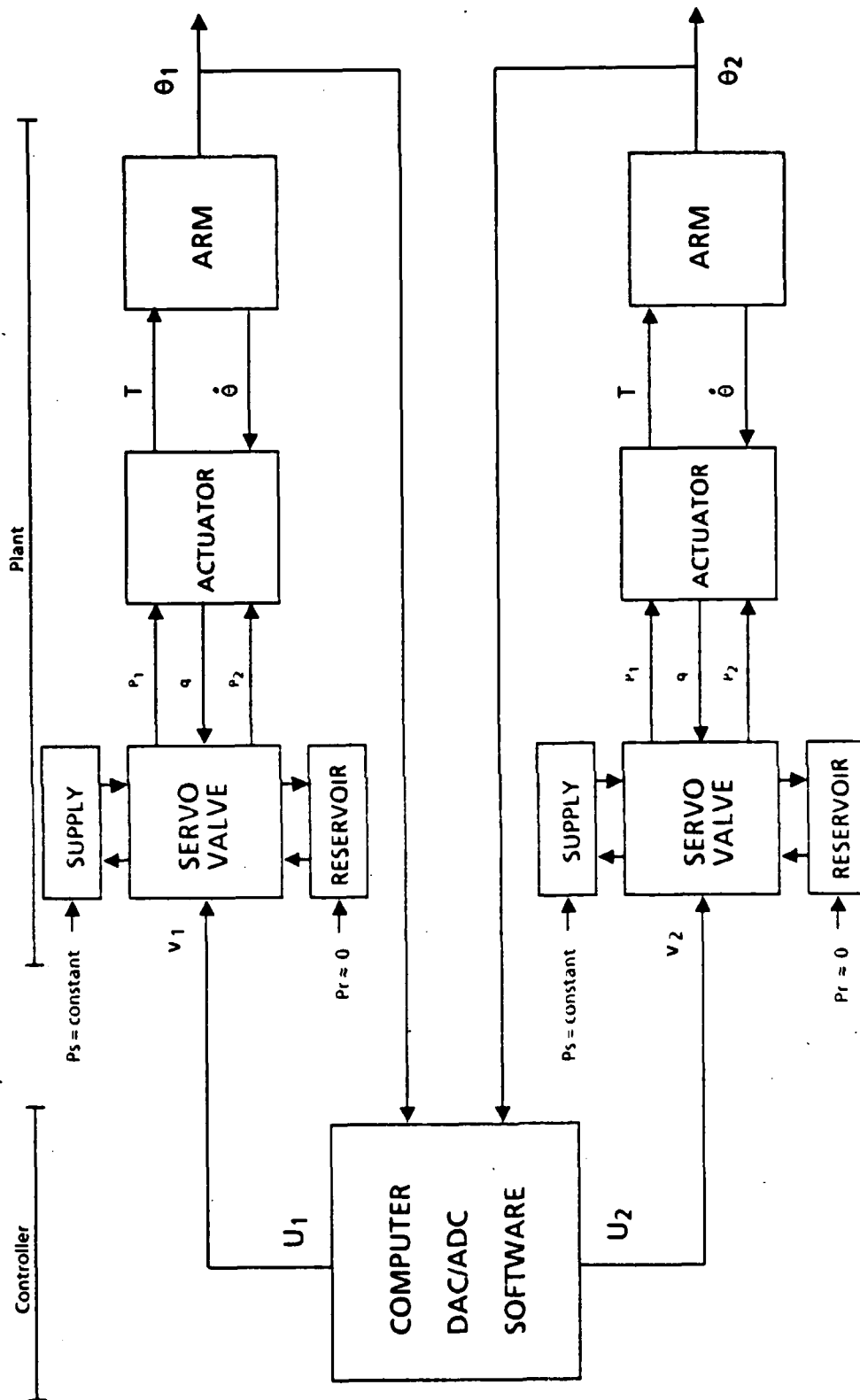
Figure 6
Multi-Port Block Diagram

24

of the plant. Because the speed and computational efficiency of the IBM PC AT are significantly less than that of a larger mainframe computer, any simplification of the model may allow for a shorter controller sample rate.The controller is defined as the combination the sensor acquisition/conversion elements, the IBM PC AT computer, and the control program. With the exception of Digital-to-Analog Converters (DAC), Analog-to-Digital Converters (ADC), and the computer itself, all control and regulation is software based. The DAC and ADC are contained on two expansion port boards internal to the AT. Computer interfacing was done with the system known as LABPAC, which has 6 12 bit DAC's and 16 12 bit ADC's. With 12 bits of data availabe for conversion, the maximum available resolution is .024 %. In addition to the converters, LABPAC has an onboard clock timer for sample rate regulation. Once setup, LABPAC automatically does both data acquisition and control at set intervals.

The system model is based on the Multiple Input Multiple Output (MIMO) elements of: the computer controller, servovalves, hydraulic actuators, and the arm itself. To create motion in the system, a voltage potential (v) is applied to the servovalve electrical input, which in turn sets up a current flow through the valve actuating coil. This causes an opening of the valve orifice. The actuating voltage in combination with the actuator feedback of fluid flowrate (q) produces the valve pressure outputs P_1 and P_2. In turn P_1 and P_2 are used as inputs to the actuator along with the arm velocity (Θ) in order to generate the torque (T) which creates motion in the arm.

In order to validate the robot test bed system for future operation, an optimal state space controller (LQR) was developed and implemented. As discussed by Ogata [Ref. 6] and Owens [Ref. 7], optimal control theory requires that a merit function J be selected. J can be considered the performance index that is to be minimized. To meet with established conventions, the merit function usually uses the two quadratic forms that follow.

$$J_1 = \int_0^\infty (\mathbf{x}^T \mathbf{Q} \mathbf{x}) \, dt \qquad (Eqn.\ 1)$$

$$J_2 = \int_0^\infty (\mathbf{u}^T \mathbf{R} \mathbf{u}) \, dt \qquad (Eqn.\ 2)$$

The matrices x and u are the state space matrices that correspond to state error and system-inputs respectively. Q is a weighting matrix that determines the relative importance of each term in the state matrix. R is determined by the system performance factor to be minimized, and cost weighting given each input. J can take the form of the arithmetic combination of Equations 1 and 2 in the form :

$$J = J_1 + J_2 \qquad (Eqn.\ 3)$$

$$J = \int_0^\infty \{\lambda (\mathbf{x}^T \mathbf{Q} \mathbf{x}) + (\mathbf{u}^T \mathbf{R} \mathbf{u})\} \, dt \qquad (Eqn.\ 4)$$

This is helpful because for most real life systems the minimization of the state error alone must be tempered by at least two considerations. First, all operations "cost" something whether it is energy, time, or some other quantity. Secondly, since this form of optimal control produces the feedback law:

$$u = -\mathbf{K}\mathbf{x} \qquad\qquad (Eqn.\,5)$$

a large state error will consequently produce a correspondingly large correcting input. Too large a feedback, however, can saturate most real systems thereby giving them a high degree of non-linearly.

To narrow the scope of the problem and provide a realistic goal, the performance indices chosen were related to state error versus the square of the hydraulic power used by the system. For the purpose of this discussion, the definition of hydraulic power will be that used by Merritt [Ref. 8] where:

$$Power = P_s\, q \qquad\qquad (Eqn.\,6)$$

$$P_s = P_{supply} = constant$$

Initial dynamic modeling of the two link arm mechanism was done in global vice local coordinate systems. This decision was made in anticipation of future problems with solving for joint accelerations using the Newton-Euler forward dynamic equations. If local coordinates are used in conjunction with the Denavit-Hartenburg [Ref. 9] convention, the potential exists for a singular solution when two adjoining links are colinear with the relative angle being either 0 or 180. degrees It was realized that the joint solutions in local coordinate systems are more computationally efficient; However, the singularity condition described above precludes general implementation of a model reference position control algorithm that does not have error handling procedures.

Subsequent modeling of the NEPTUNE system revealed that a much less complex plant model was needed to satisfactorily describe the motion. This realization, when coupled with the fact that all sensors and actuators functioned in local coordinates, allowed final implementation of the controller in joint relative coordinates.

There have been numerous research efforts aimed at various types of micro-computer robotic control [Refs. 10-14]. Optimal path control is dealt with by Snyder [Ref. 15]. The closest research done in the area of optimizing power appears in Reference 16, where performance indices similar to the one mentioned above are used, with the focus on weighted near minimum time-fuel control.

III. ANALYTICAL SYSTEM CHARACTERIZATION

A. RIGID TWO LINK SYSTEM MODEL

The Newton-Euler formulation for the robot arm was used in developing the classical dynamic model. Previous work by Lewis [Ref. 4] on the NEPTUNE arm showed that with the original solenoid valves installed, reduced dynamic Equations 7 and 8 could be used (all angles are relative).

$$T_1 = \beta_1 \dot{\Theta}_2 + D g \sin(\Theta_2 - \Theta_1) + G g \sin(\Theta_1) - M_s \qquad (Eqn. 7)$$

$$T_2 = \beta_2 \dot{\Theta}_2 + D g \sin(\Theta_2 - \Theta_1) \qquad (Eqn. 8)$$

$$D = m_2 d_2 + m_3 (l_2 + d_3)$$

$$G = l_1 (m_2 + m_3) + m_1 d_1$$

$$M_s = \text{return spring moment}$$

Because the modified arm system contained two servo valves of a higher performance and flow rate, the full Newton-Euler two degree of freedom equations of motion were used [Ref. 17]. The global formulation is shown in Figure 7.

The torque required for each joint was solved for as follows:

$$T_1 = (J_1 + m_1 d_2^2 + m_2 l_1^2)\ddot{\Theta}_1 + m_2 l_1 d_2 \cos(\Theta_1 - \Theta_2)\ddot{\Theta}_2$$
$$+ m_2 l_1 d_2 \sin(\Theta_1 - \Theta_2)\dot{\Theta}_2^2 + (m_2 g l_1 + m_1 g d_1)\cos\Theta_1 + T_2 \qquad (Eqn. 13)$$

29

$$T_2 = (J_2 + m_2 d_2^2)\ddot{\Theta}_2 + m_2 l_1 d_2 \cos(\Theta_2 - \Theta_1)\ddot{\Theta}_1$$

$$+ m_2 l_1 d_2 \sin(\Theta_2 - \Theta_1)\dot{\Theta}_1^2 + m_2 g d_2 \cos\Theta_2 \qquad (Eqn.\ 14)$$
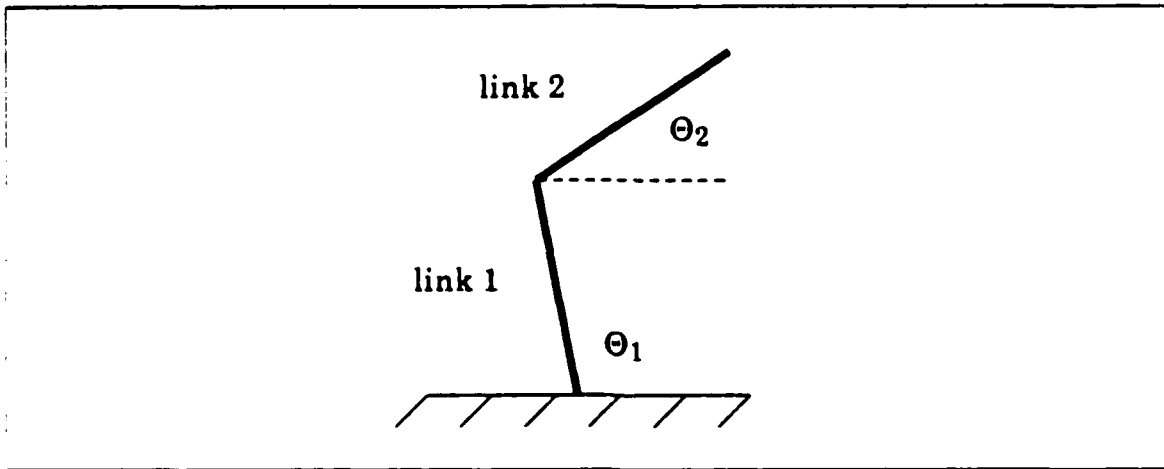

Figure 7
NEPTUNE geometry

B. SERVOVALVE MODEL

The servo valve was modeled using the classical equation for flowrate:

$$q = k\, i\, \sqrt{P_s - P_1} \qquad (Eqn.\ 15)$$

$$i = \frac{v}{\Omega}$$

Since all inputs to the actuating coil were DC, the valve impedance was modeled as a simple coil resistance (Ω). This allowed a direct conversion from the model, in current (i) to actuating voltage (v) (Eqn. 16). With the servo valve installed in the system, the flowrate relationships in Figure 8 could be used determine either the flow or pressure drops at any point in the system, if other values are known.

$$q = k v \sqrt{P_s - P_1} \qquad (Eqn. 16)$$
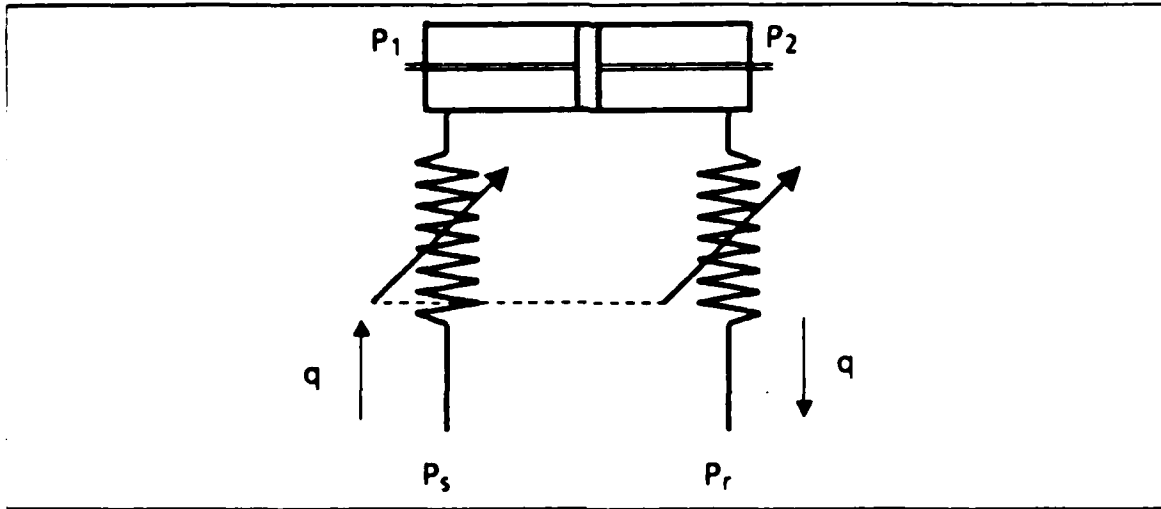
Figure 8
Pressure/Flow Schematic

If the valve is assumed to be symmetrical (both ports and spool areas are identical), then the valve constant k will be the same for both supply and return. Once k is determined experimentally , Equation 16 can be rearranged as follows :

$$P_1 = P_s \left(\frac{q}{k v} \right)^2 \qquad (Eqn. 17)$$

Refering to Figure 8 and Figure 2, it can be shown that $\dot{\Theta}$ and the flowrate q are linearly related by:

$$q = c \dot{\Theta} \qquad (Eqn. 18)$$

$$c = .1131 \; \frac{in^3}{deg} \qquad (Eqn. 19)$$

because of the combination piston, and rack and pinion gear assembly. With P_s = constant, Equation 17 can be further reduced to:

$$P_1 = P_s \left(\frac{\dot{\Theta}}{c k v} \right)^2 \qquad (Eqn. 20)$$

or

$$P_1 = fcn(v, \dot{\Theta}) \qquad (Eqn. 21)$$

C. VALVE TESTING

Pressure/flowrate tests were conducted on both servovalves in order to determine the valve constant k (Table I). As can clearly be seen, although k did follow a trend for each run, k was generally not a constant-either between the ports of the same valve, or with different input voltages. One explanation for this is that the normal operating pressure range for this valve is between 200-3000 psi. The pump and accumulator currently operate at between 100-110 psi. It is possible that the present configuration of the system forces the valve to operate in a non-linear region below the minimum design point. This notion is bolstered by the fact that although the rated maximum input voltage is 8.0 VDC, the observed saturation point is approximately 1.0 VDC for joint 1, and 0.6 VDC for joint 2. At inputs greater than these no corresponding increase in flowrate occurs.

Pressure plots of the driving cylinder (P_1), and the opposing cylinder (P_2) showed expected trends for a 0 to 90 degree move of link 2 (Fig. 9). For link 1, P_1 and P_2 remain at equal pressures until Θ_1 became greater than 35 degrees (Fig. 10). This is believed to be caused by the driving force on link 1 of the return springs. Once Θ_1 exceeds 35 degrees, the force added by the springs

32

TABLE I

VALVE CONSTANT CALCULATION RESULTS

|	Input current (mA)	Flow rate (in./s)	delta Ps (psi)	delta Pr (psi)	Ks	Kr
Joint 1	2.5	1.43	65.9	64.7	70.4	70.4
Run 1		1.15	54.0	74.1	62.4	53.3
		.855	42.0	87.6	52.8	36.5
Joint 1	5.0	1.86	67.4	65.0	45.3	46.1
Run 2		1.47	56.7	75.4	39.0	33.9
		1.07	43.6	90.3	32.4	22.5
Joint 2	1.25	0.410	40.7	101.3	51.4	32.6
Run 1		0.446	47.4	98.2	51.8	36.0
		0.541	61.0	92.7	55.4	45.0
Joint 2	3.75	0.95	36.0	96.3	42.2	25.8
Run 2		1.12	40.8	90.1	46.8	31.5
		1.36	49.5	82.5	51.6	39.9
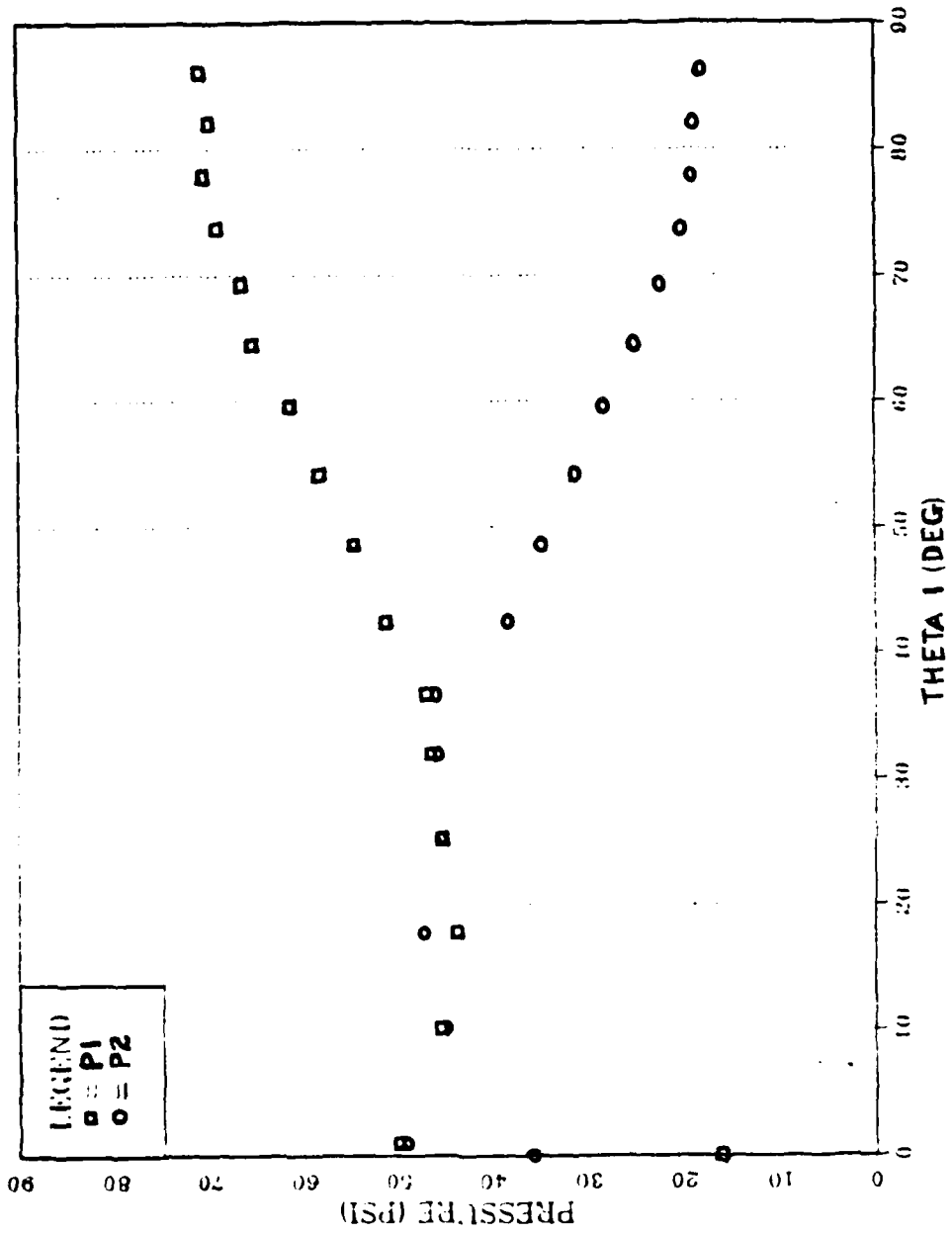
Figure 9
Joint 1 Pressure Plot
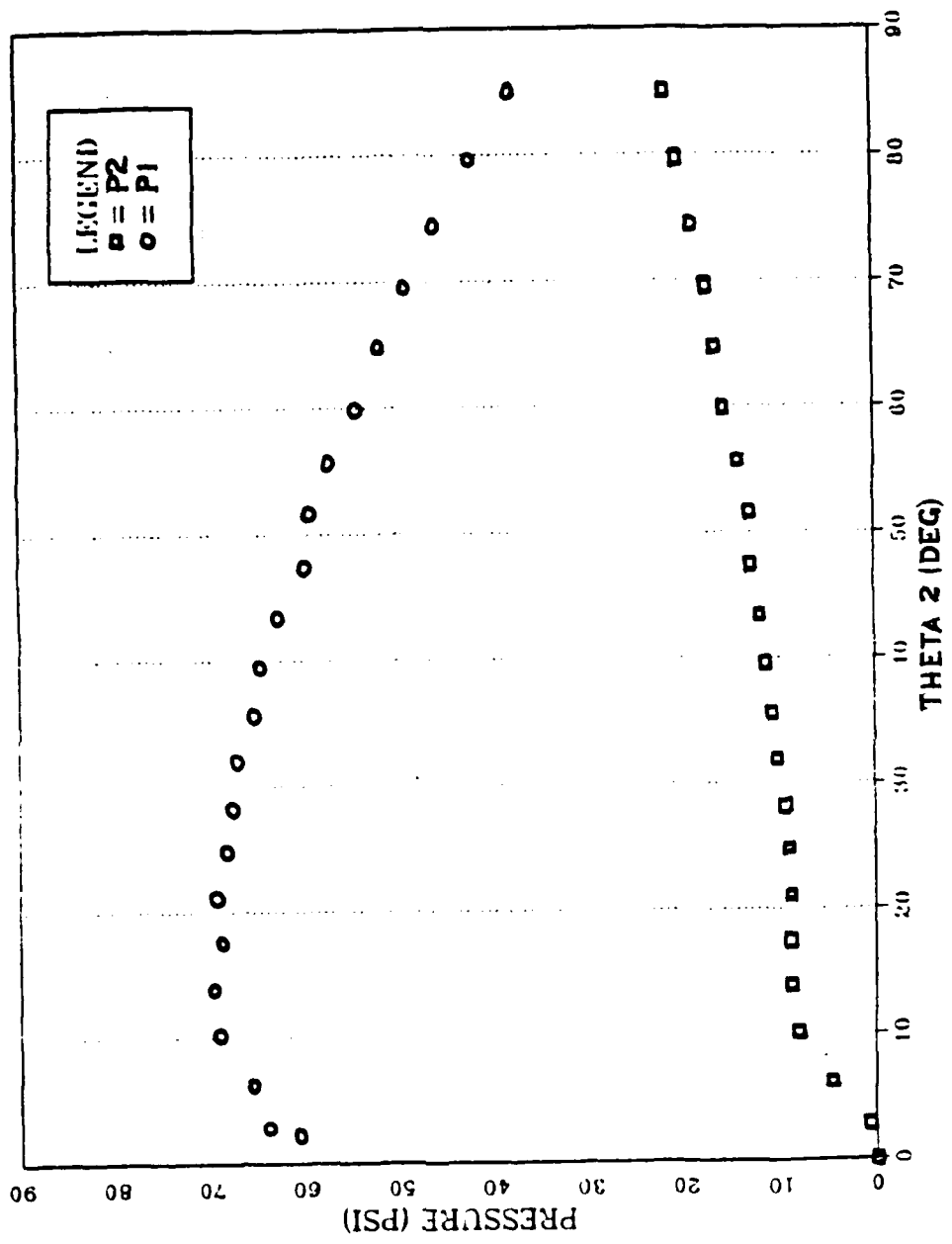
Figure 10
Joint 2 PressurePlot

35

decreased significantly, and the pressure plots follow the anticipated pattern. The maximum change in either P_1 or P_2, for either link was determined to be 25 psi. When incorporated into the valve model (Eqn. 15), the change in the flowrate or joint velocity is relatively small, even with a large angular. change. These observations tend to confirm Lewis' hypothesis that the NEPTUNE is a low performance robot arm, and as such, most of the system dynamics may be discounted.

Because classical valve operation and arm dynamics were unable to be validated by actual component performance, it was decided that an analytical model of the system would provide poor results. As an alternative, an equivalent linearization technique utilizing frequency response was selected. The system was modeled empirically using magnitude and phase plot.

IV. EMPIRICAL SYSTEM CHARACTERIZATION

A. EXPERIMENTAL SETUP

A Hewlett-Packard 3562A Dynamic Signal Analyzer was used to produce the Bode plots for plant modeling and analysis. This signal analyzer is capable of scanning a desired frequency range with a sinusoidal output, while simultaneously measuring and plotting transfer function magnitude and phase data. The signal analyzer output was hooked directly to the servovalve electrical inputs. The input to the signal analyzer was taken from the existing position feedback potentiometers on the manipulator arm. A small amplitude voltage was used to excite the servovalves. In this way an equivalent linearization of the arm was measured.

Based on the most likely operating regions of the arm, three linearization configurations were selected. For link 1, a mid-range point of 45 degrees was chosen. It was believed this position best accounted for actuator dynamics, link motion, and the nonlinearity created by the two return springs on link 1. Three linearization points were chosen for link 2. They were -45, 0, and +45 degrees (Fig. 11). These positions provided the best coverage for link 2 motion. Table II lists all data acquisition runs and initial conditions. Figure 12 displays the anticipated MIMO plant model to include cross coupled dynamics between the joints. It was anticipated that each linearization point would require a different set of transfer functions.

Although the effects of servovalve fluid leakage between the spool and housing were initially deemed negligible compared to the flow through the valve, the experiments showed that drift in the position of the link became

37

TABLE II

EQUIVALENT LINEARIZATION DATA RUNS

Run No.	U_1 (VDC/DC offset)	U_2 (VDC/DC offset)	Θ_1 (deg)	Θ_2 (deg)	Function Sampled
1	.3/.1	fixed	+45	-45	Θ_1/U_1
2	.3/.1	fixed	+45	0	Θ_1/U_1
3	.3/.1	fixed	+45	+45	Θ_1/U_1
4	fixed	.15/.1	+45	-45	Θ_2/U_2
5	fixed	.4/.15	+45	0	Θ_2/U_2
6	fixed	.2/.1	+45	+45	Θ_2/U_2
7	fixed	.15/.1	+45	-45	Θ_1/U_2
8	fixed	.4/.15	+45	0	Θ_1/U_2
9	fixed	.2/.1	+45	+45	Θ_1/U_2
10	.3/.1	fixed	+45	-45	Θ_2/U_1
11	.3/.1	fixed	+45	0	Θ_2/U_1
12	.3/.1	fixed	+45	+45	Θ_2/U_1
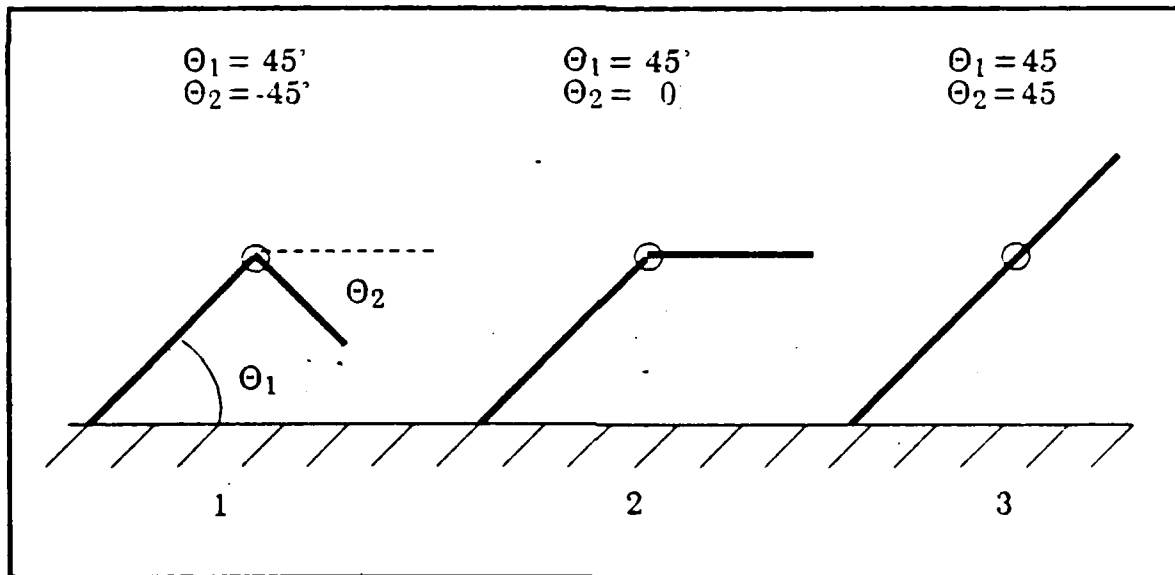
Figure 11
Linearization configurations
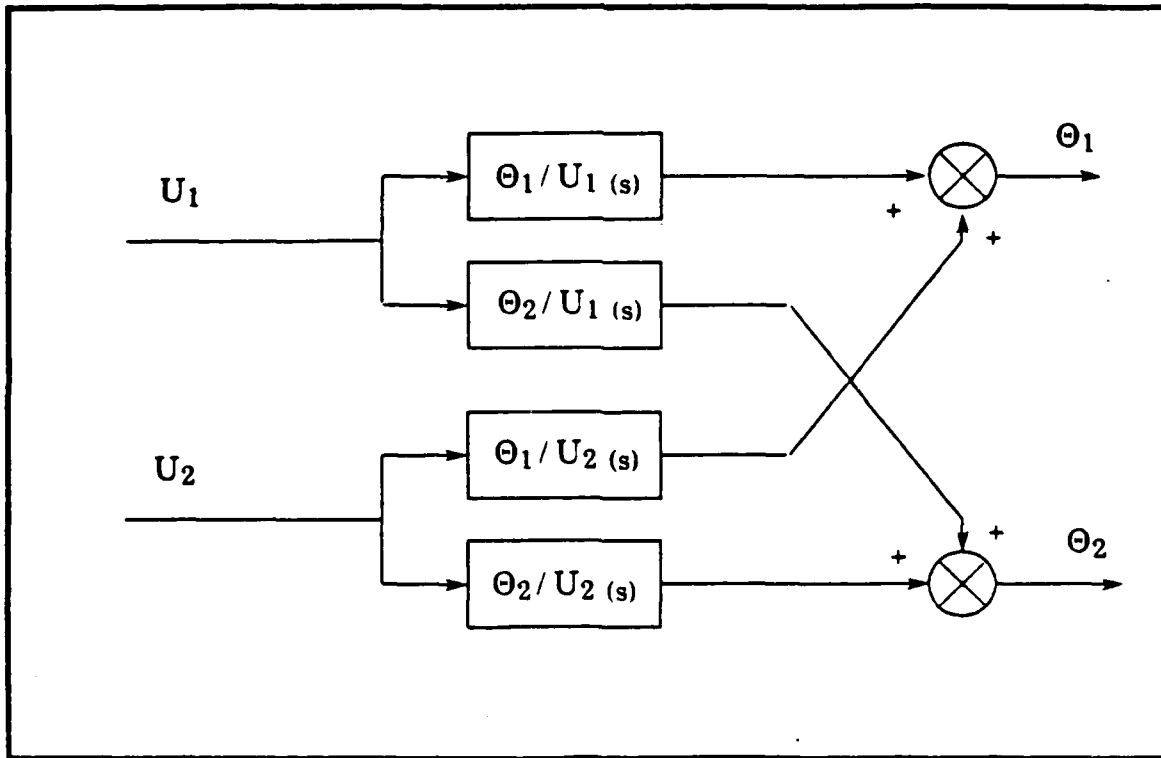
Figure 12
Plant Block Diagram

noticeable when the valve was hydraulically charged, but electrically inactive. To negate this effect, the unactivated link fluid supply hoses were disconnected and plugged at the valve end. The result of this was that the hydraulic characteristics (bulk modulus of elasticity, fluid properties, pressure wave reverberations, etc.) of the actuating cylinders and supply hoses on the unactivated link was included in the equivalent linearization, with the servovalve assumed to have no leakage.

39

B. RESULTS

1. Link 1

Figure 13 shows the results of the frequency response plots at $\Theta_1 =$ +45 degrees, $\Theta_2 =$ -45 degrees. In this run, Θ_2 was held constant and the sinusoid signal was input to servovalve 1. The output from the joint 1 feedback potentiometer was compared to the valve input signal in order to obtain the Bode plots. The frequency range of measured output was from .1-10 Hz. Curve approximations to data (dashed line) showed the best fit in both magnitude and phase plots was a two pole system. One pole was located at 0 Hz and the second pole was rooted at 3.6 Hz. The gain K_p was 1.1. The system displayed an apparent transportation lag of 0.04 seconds. This feature was anticipated since all real systems, particularly mechanical ones, have some finite time delay between signal input and noticeable output. The transportation lag was constant for all data runs of both valves, mainly because both valve and cylinder assemblies are essentially identical with the supply hoses of about the same length. A trial first order curve fit of the same data with a single pole located at 0 Hz corresponding to a transfer function of (K s) was also tried. Although the approximation was relatively good at lower frequencies, higher frequencies showed poor correlation in both magnitude and phase. Adjustments for transportation lag provided no significant improvement and the overall result was considered unacceptable. After careful analysis, the following transfer function was determined to most closely model link 1:

$$\frac{\Theta_1}{U_1} = \frac{1.1\,e^{-0.04\,s}}{s(s + 3.6)} \qquad (Eqn\ 22)$$

40
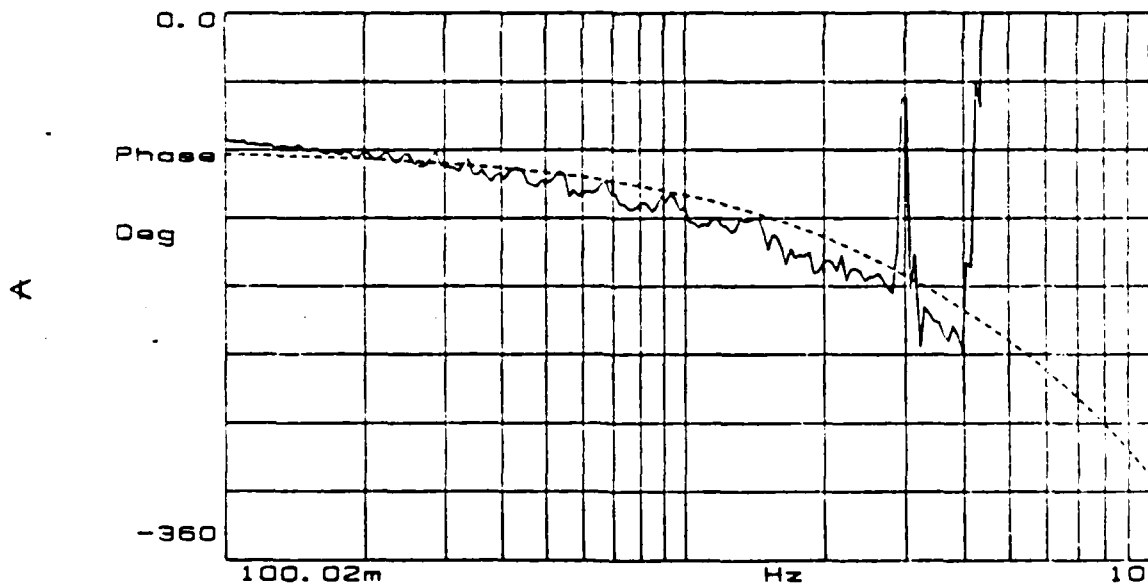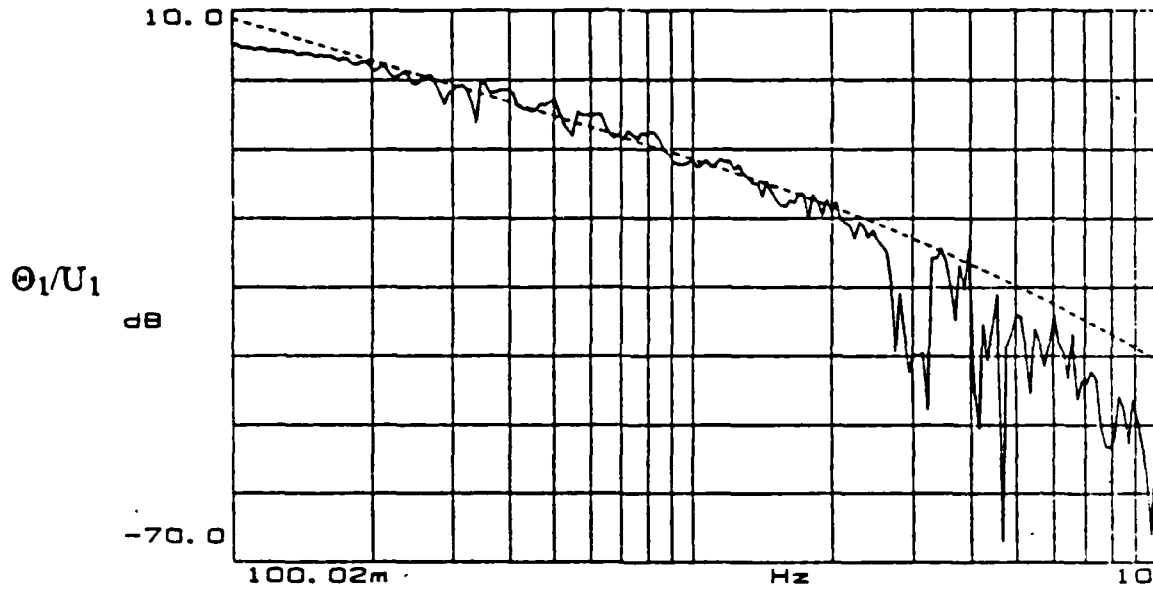
Figure 13
Configuration 1 Linearization - Θ_1/U_1 data

Linearization of link 1 at $\Theta_2 = 0$ degrees (Fig. 14), and +45 degrees (Fig. 15) produced similar results as described above with the transfer functions being :

$$\frac{\Theta_1}{U_1} = \frac{1.1\, e^{-0.04\, s}}{s(s + 3.6)} \qquad (Eqn.\ 23)$$

$$\frac{\Theta_1}{U_1} = \frac{1.0\, e^{-0.04\, s}}{s(s + 3.6)} \qquad (Eqn.\ 24)$$

respectively. Since all three transfer functions were within an experimental errror factor of 10%, it was decided that one common linearization point would suffice (Eqn. 22). Converting Θ_1 from volts/sec to degrees/sec gave the final form that would be implemented for the link 1 transfer function.

$$\frac{\Theta_1}{U_1} = \frac{100.16\, e^{-0.04\, s}}{s(s + 327.7)} \qquad (Eqn.\ 25)$$

2.   Link 2

Figure 16 shows data acquired from link 2 with Θ_1 fixed at +45 degrees, and Θ_2 linearized around -45 degrees. Analysis of the plots revealed a pole at 0 Hz, similar to link 1 results. However, no signs of any higher frequency poles were evident. A good curve fit to data was accomplished with a transfer function of the form (K/s). Once again a transportation lag of 0.04 seconds was evident in the phase plot, and the gain K_p was determined to be 0.21 :
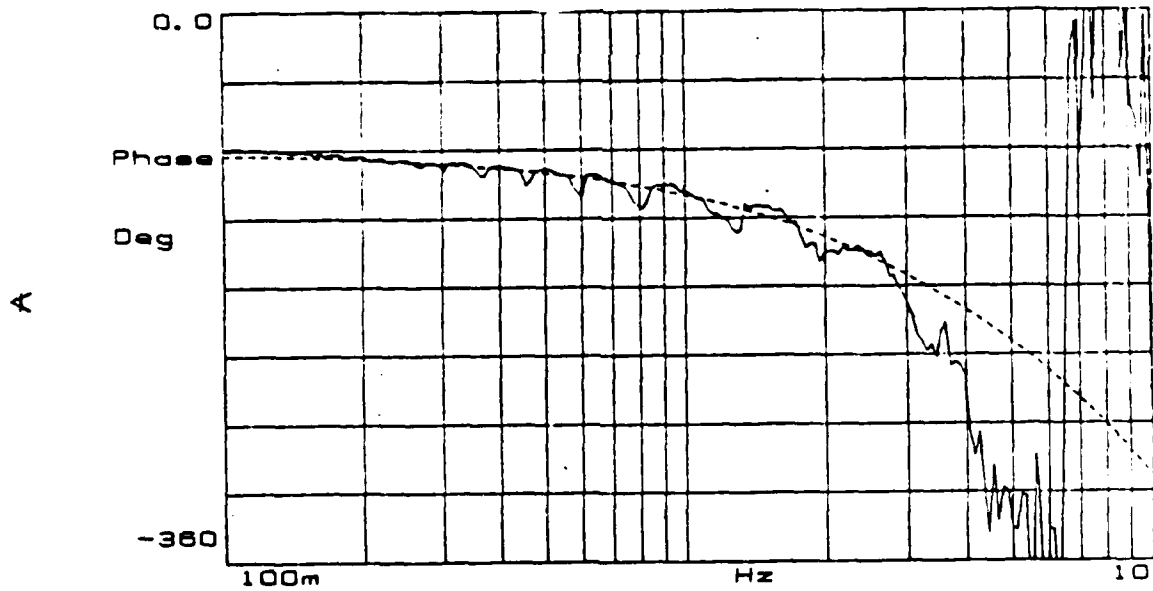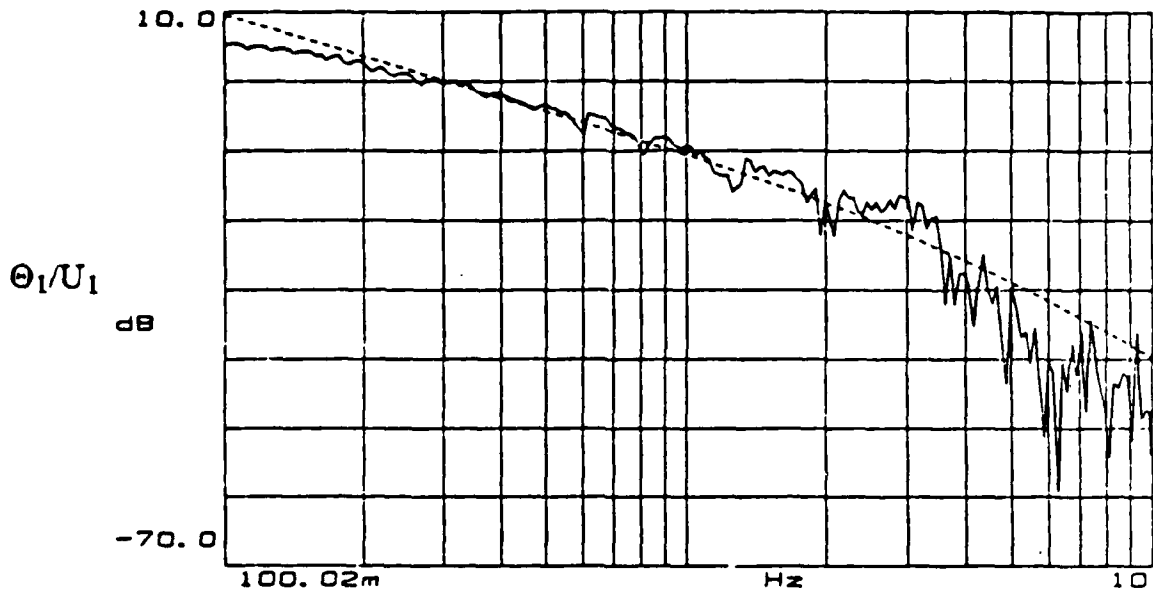
Figure 14
Configuration 2 Linearization - Θ_1/U_1 data
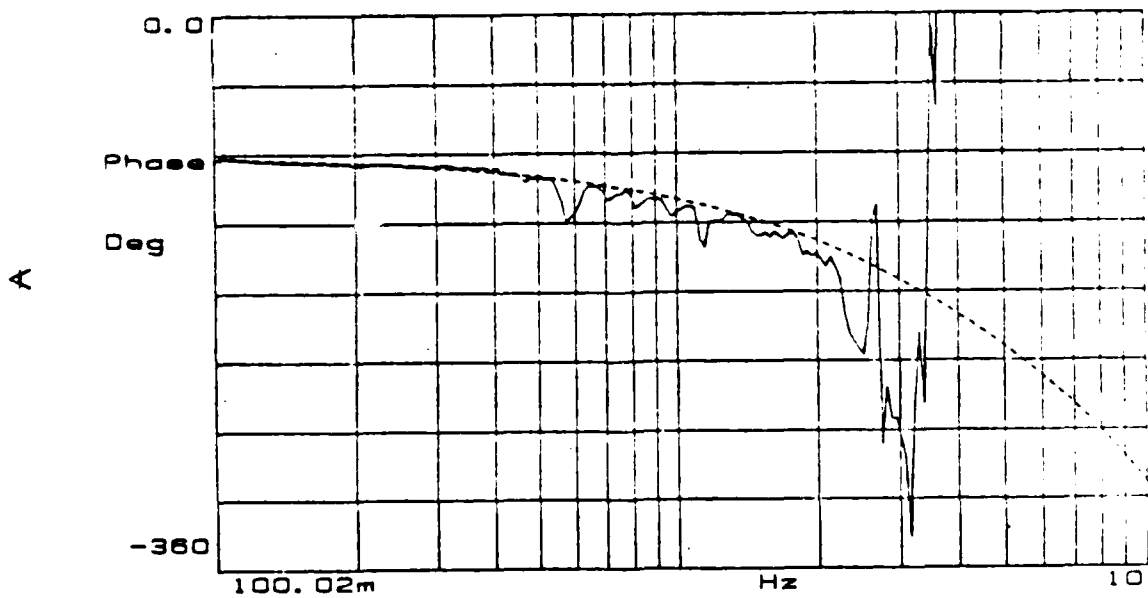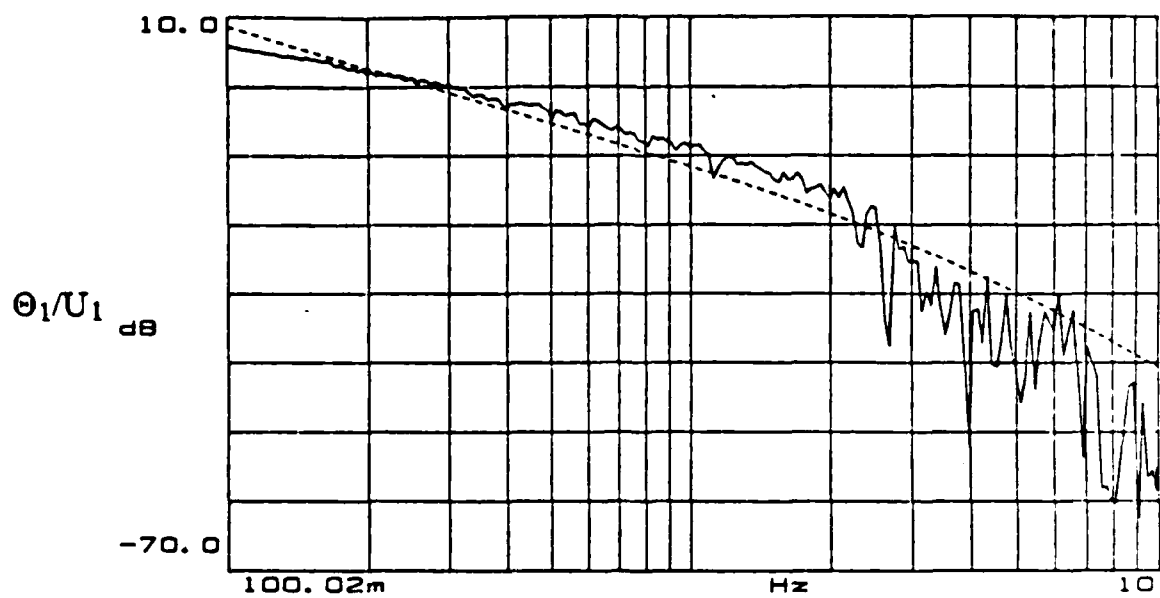
Figure 15
Configuration 3 Linearization - Θ_1/U_1 data

44
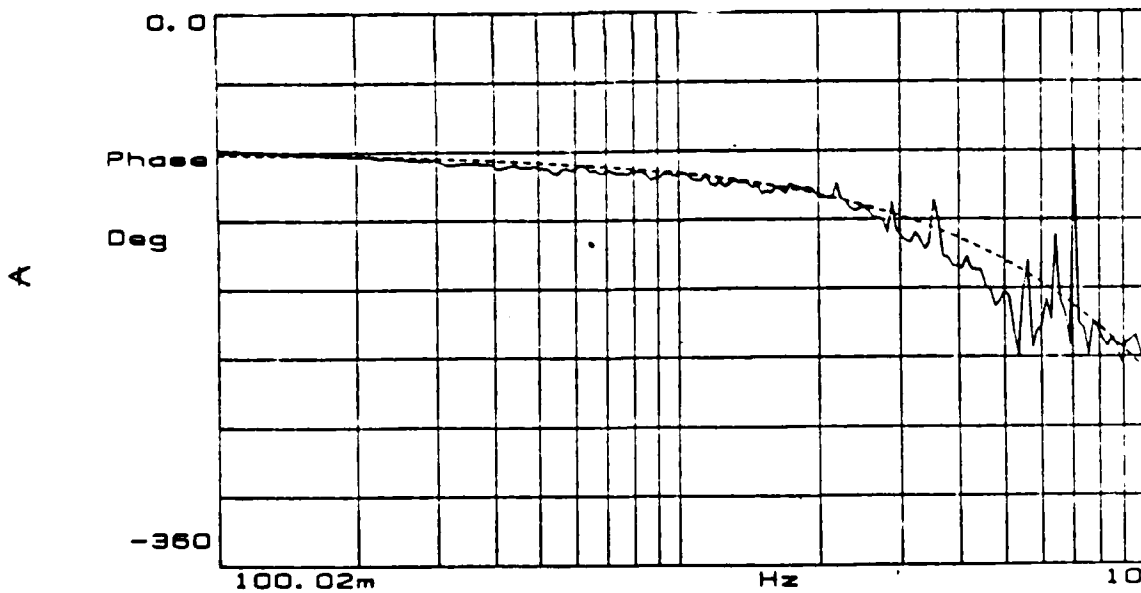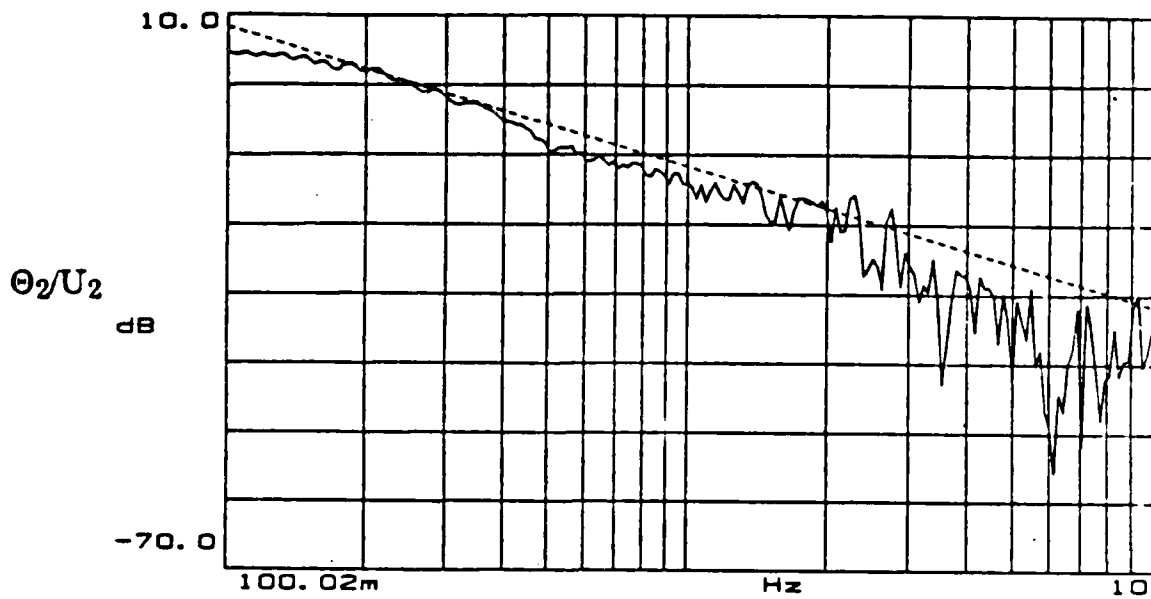
Figure 16
Configuration 1 Linearization - Θ_2/U_2 data

45

$$\frac{\Theta_2}{U_2} = \frac{.21\,e^{-0.04\,s}}{s} \qquad (Eqn.\ 26)$$

Figure 17 shows the results of linearization around $\Theta_2 = 0$ degrees. Comparable results were obtained from this data run, with the transfer function determined to be :

$$\frac{\Theta_2}{U_2} = \frac{.26\,e^{-0.04\,s}}{s} \qquad (Eqn.\ 27)$$

Linearization at $\Theta_2 = +45$ degrees could not be accomplished using the signal analyzer because of the low DC signal offset required to keep the link in gravitational equilibrium. Limited data points were taken manually with Fig. 18 showing an approximate curve fit. Although this data was unusable in providing an accurate model, it does show correlation to the data of the previous two linearization points. The approximate transfer function for link 2 was:

$$\frac{\Theta_2}{U_2} = \frac{.23\,e^{-0.04\,s}}{s} \qquad (Eqn.\ 28)$$

As in the case of link 1, since the results were so closely grouped, it was felt that only one linearization equation would be needed to adequately model the range of the three original set points. Conversion from volts/sec to degree/sec produced the final form for the link 2 transfer function (Eqn. 29).
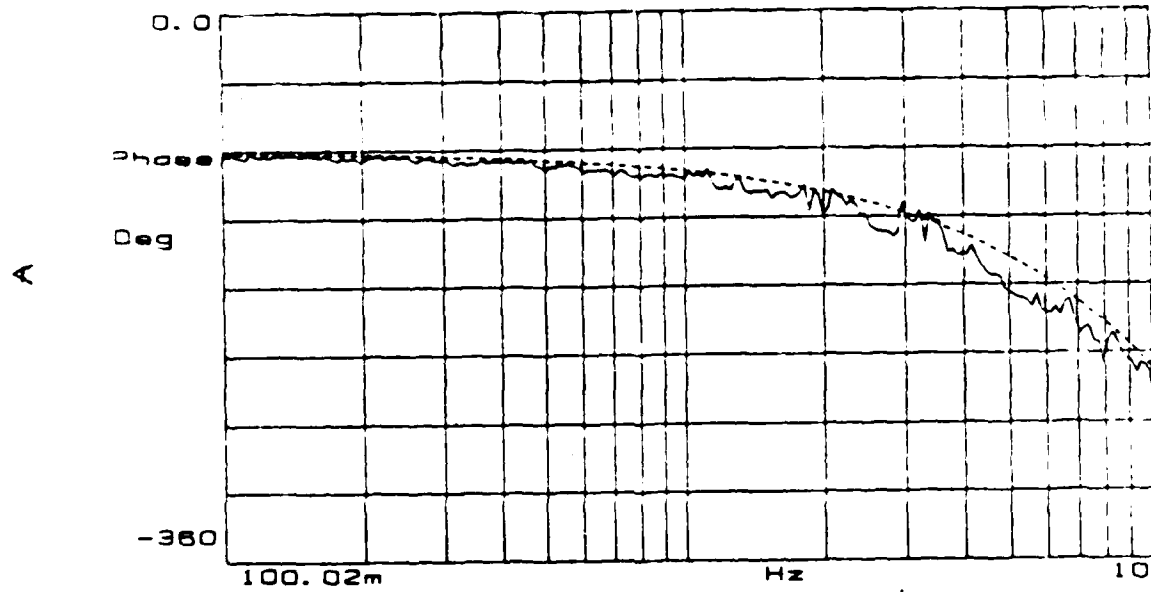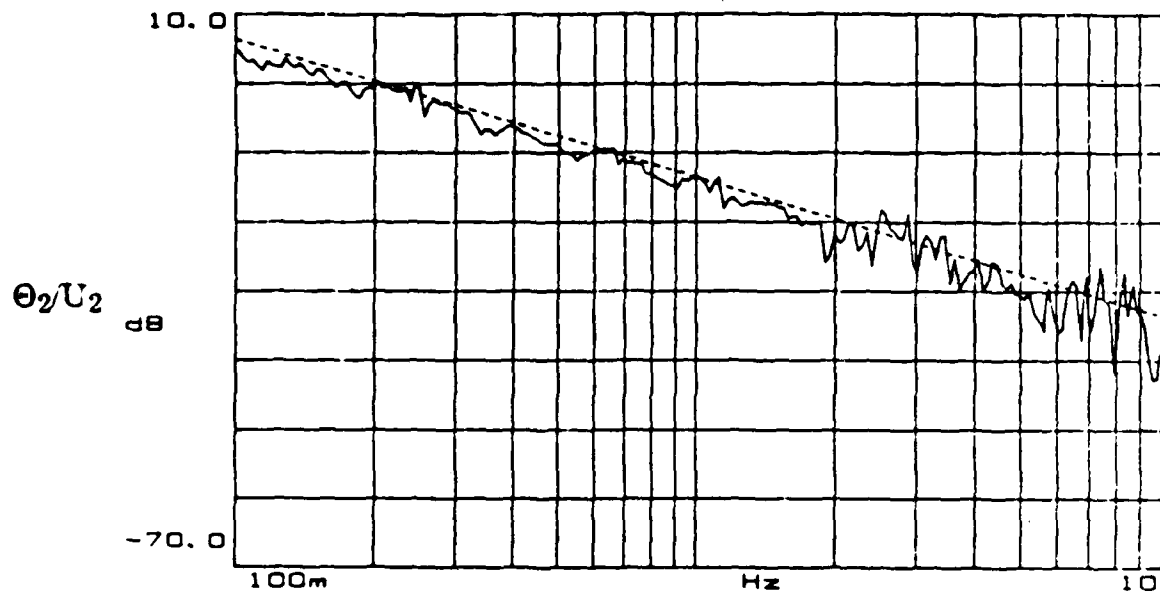
Figure 17
Configuration 2 Linearization - Θ_2/U_2 data

47

$$\frac{\Theta_2}{U_2} = \frac{\{22.5\,e^{-0.04\,s}\}}{s} \qquad (Eqn.\ 29)$$

3. Cross Joint Coupling

In most complex mechanisms, dynamic cross coupling between links is a very real factor that will inevitably increase the system complexity. In an effort to account for this the plant model presented in Figure 12 contains two additional transfer functions, Θ_1/U_2 and Θ_2/U_1. These transfer functions contain the cross-coupling terms that generate an output motion in link 2 when joint 1 is actuated, and vice versa. Data taken in runs 7 through 12 were used to determine the cross-coupled effects. In all runs, random data scatter occured between -35 and -70 dB with no correlation or consistency. The conclusion is that the low velocities and accelerations generated by this arm are not enough to produce any significant cross-coupling motion. In effect each individual link can be considered independent. This result is specific to the NEPTUNE arm performance and may not be the case for higher performance systems. Therefore, care must be taken to test for the existence of dynamic cross-coupling before attempting similar simplification.

4. Revised Plant Model

With the elimination of cross-coupling and the decrease in the number of linearization points, a revised plant model is shown in Figure 19. The conversion of these transfer functions from the Laplace domain to the time domain yielded :

$$\ddot{\Theta}_1 = -327.7\,\dot{\Theta}_1 + 100.2\,U_1\,(t - 0.04) \qquad (Eqn.\ 30)$$

$$\dot{\Theta}_2 = 22.5\,U_2\,(t - 0.04) \qquad (Eqn.\ 31)$$

48

The acceleration term in Equation 30 strongly suggests that although the U_2 input has no cross-coupling effect to Θ_1, the inertia generated by the mass translation of link 2 is still important to the motion of link 1. The impact of Equation 31 is that the velocity of link 2 is directly controllable by the input voltage U_2, to the servovalve.

$$U_1 \xrightarrow{\hspace{2cm}} \boxed{\frac{100.2}{s\,(s+327.7)}\; e^{-0.04\,s}} \xrightarrow{\hspace{2cm}} \Theta_1$$

$$U_2 \xrightarrow{\hspace{2cm}} \boxed{\frac{22.5}{s}\; e^{-0.04\,s}} \xrightarrow{\hspace{2cm}} \Theta_2$$
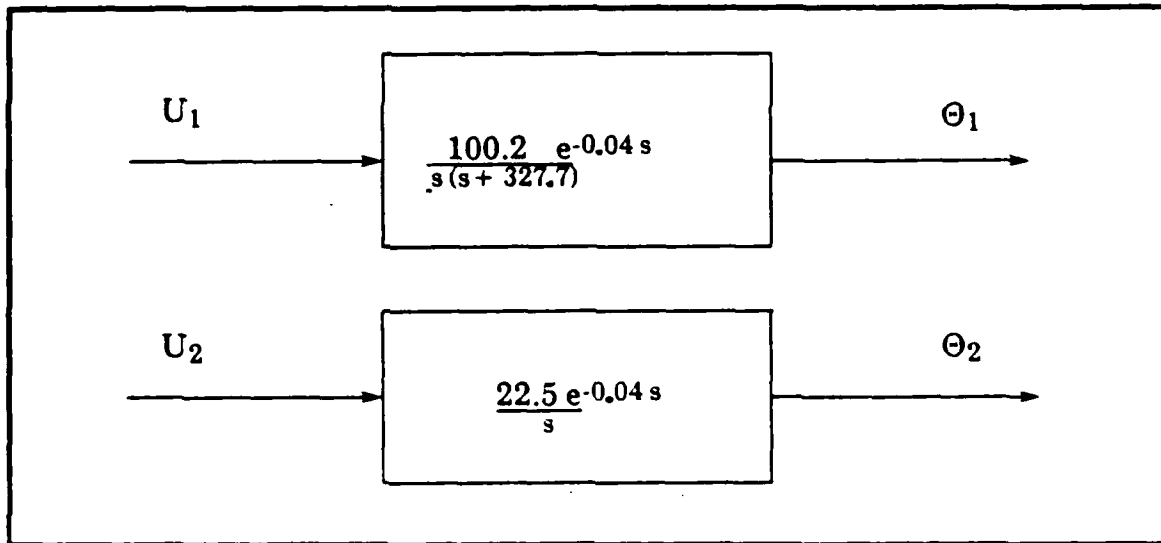
Figure 19
Revised Plant Model

V. OPTIMAL CONTROL THEORY

A. CONTINUOUS TIME LINEAR QUADRATIC REGULATOR

The **Linear Quadratic Regulator** (LQR) is considered one of the most important and most used optimal controllers. The reason for this is based on the fact that although the derivation of the control law is a laborious and painstaking procedure, the implementation is an extremely simple and straightforward method to achieve multiple coordinated inputs. LQR control assumes that the plant can be modeled linearly in state space with:

$$\dot{\mathbf{x}} = \mathbf{A}\mathbf{x} + \mathbf{B}\mathbf{u} \qquad (Eqn. 32)$$

Additionally, the performance index J must be of the quadratic form:

$$J = \int_0^{\infty} \{\lambda (\mathbf{x}^T \mathbf{Q}\mathbf{x}) + (\mathbf{u}^T \mathbf{R}\mathbf{u})\} dt \qquad (Eqn. 4)$$

As discussed earlier, the weighting matrices **Q** and **R** have special definitions with respect to state error and control cost. Further restrictions apply to each weighting matrix : **Q** must be either a positive semi-definite or positive definite, real symmetric matrix; **R** on the other hand is required to be a positive definite, real symmetric matrix. Once **Q** and **R** are reduced to the proper form, a gain matrix **K** can be found in a two step procedure. The first step necessiates the solving of the reduced matrix Riccati equation for the unique positive definite, real symmetric matrix **P**.

$$\mathbf{A}^T \mathbf{P} + \mathbf{P}\mathbf{A} - \mathbf{P}\mathbf{B}\mathbf{R}^{-1}\mathbf{B}^T\mathbf{P} + \mathbf{Q} = 0 \qquad (Eqn. 33)$$

The matrix **K** will then follow directly as:

$$K = R^{-1}B^T P \qquad (Eqn. 34)$$

With **K** determined, the governing control law is given as

$$u = -Kx \qquad \cdot \qquad (Eqn. 5)$$

Figure 20 shows the corresponding system block diagram.
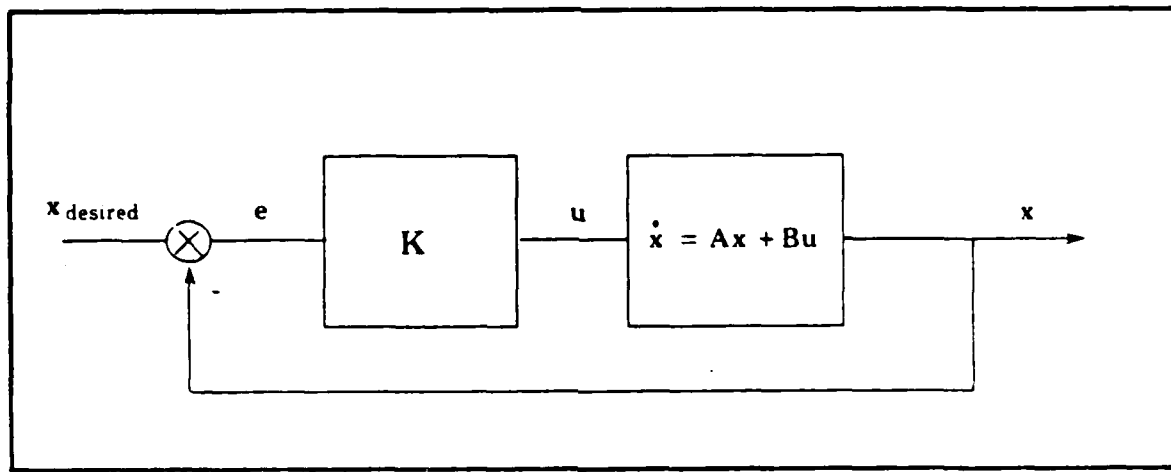
Figure 20
Optimal Feedback Control Block Diagram

In this work the state selections were: $x_1 = \Theta_1$, $x_2 = \dot{\Theta}_1$, $x_3 = \Theta_2$. Since NEPTUNE has only position feedback potentiometers, joint 1 velocities ($\dot{\Theta}_1$) were calculated using a backward difference method.

B. DISCRETE TIME LINEAR QUADRATIC REGULATOR

Because the system controller was to be implemented in software using a computer, the continuous time LQR had to be converted to a discrete time format. This required discretizing the plant model, the performance index,

51

and the matrix Riccati equation. This work has been done previously [Refs. 4,15,16] and the results are presented in Equations 35 (plant), 38 (performance index), and 39 (gain matrix) for comparison to the continuous time LQR controller equations.

$$x(n+1) = \Phi\, x(n) + \Gamma\, u(n) \qquad\qquad (Eqn.\ 35)$$

$$\Phi = e^{Ah} \qquad\qquad (Eqn.\ 36)$$

$$\Gamma = \{\textstyle\int_0^h e^{At}\, dt\, \}\, B \qquad\qquad (Eqn.\ 37)$$

$$J = \sum_{n=0}^{\infty} \{\lambda\, (x^T(n)\, Qx(n)) + (u^T(n)\, Ru)(n)\}\, dt \qquad (Eqn.\ 38)$$

$$K = (R + \Gamma^T P\Gamma)^{-1}\, \Gamma^T P\, \Phi \qquad\qquad (Eqn.\ 39)$$

C. EFFECTS OF TRANSPORTATION LAG

Transportation lag in the discrete time system is an important factor from the viewpoint of sample rate and system stability. If the sample period (h) is significantly shorter than the time delay (τ), several control periods may go by before there is a corresponding change in the output. One method to rectify this problem is provided for in Reference 18; It requires the addition of an extra state for each overlapped sample period. With τ less than the sample period, Equations 40,41,42,43 detail the procedure and contents of the modified Φ and Γ matricies. Actual determination of the sample period that was used will be discussed in a later section.

$$\Phi = e^{A h} \qquad (Eqn. 40)$$

$$\Gamma_1 = e^{A(h-\tau)} \left\{ \int_0^\tau e^{At} \, dt \right\} B \qquad (Eqn. 41)$$

$$\Gamma_0 = \left\{ \int_0^{(h-\tau)} e^{At} \, dt \right\} B \qquad (Eqn. 42)$$

$$\begin{bmatrix} x(n+1) \\ u(n) \end{bmatrix} = \begin{bmatrix} \Phi & \Gamma_1 \\ 0 & 0 \end{bmatrix} \begin{bmatrix} x(n) \\ u(n-1) \end{bmatrix} + \begin{bmatrix} \Gamma_0 \\ I \end{bmatrix} u(n) \qquad (Eqn. 43)$$

D. DISCRETE PLANT DETERMINATION

From Equations 30,31 the continuous time linear plant model was determined to be:

$$x = \begin{bmatrix} 1 & 0 & 0 \\ 0 & -327.7 & 0 \\ 0 & 0 & 0 \end{bmatrix} x + \begin{bmatrix} 0 & 0 \\ 100.2 & 0 \\ 0 & 22.5 \end{bmatrix} u \qquad (Eqn. 44)$$

Discretization of this for a sample period of 0.05 seconds leads to:

$$x(n+1) = \begin{bmatrix} 1 & 3.05(10^{-3}) & 0 \\ 0 & 7.66(10^{-8}) & 0 \\ 0 & 0 & 1 \end{bmatrix} x(n) + \begin{bmatrix} 1.44(10^{-2}) & 0 \\ 3.03(10^{-1}) & 0 \\ 0 & 1.125 \end{bmatrix} u(n) \qquad (Eqn. 45)$$

Inclusion of the transportation delay produced the following Φ and Γ matrices:

$$\Phi = \begin{bmatrix} 1 & 3.05(10^{-3}) & 0 & 2.03(10^{-2}) & 0 \\ 0 & 7.66(10^{-8}) & 0 & 1.15(10^{-2}) & 0 \\ 0 & 0 & 1 & 0 & 0.9 \\ 0 & 0 & 0 & 0 & 0 \\ 0 & 0 & 0 & 0 & 0 \end{bmatrix} \qquad (Eqn. 46)$$

$$\Gamma = \begin{bmatrix} 2.16(10^{-3}) & 0 \\ 2.94(10^{-1}) & 0 \\ 0 & 2.25(10^{-1}) \\ 1 & 0 \\ 0 & 1 \end{bmatrix} \qquad (Eqn.\ 47)$$

E. DETERMINATION OF THE WEIGHTING MATRICES

The selection of the **R** matrix was driven by the goal to minimize hydraulic power. To fit the form of the quadratic performance index and also to force **R** to be positive definite it was decided to minimize Power ^{2}.

$$Power_i^2 = (P_s q_i)^2 \qquad (Eqn.\ 48)$$

$$= P_s^2 q_i^2$$

$$= P_s^2 c^2 \dot{\Theta}_i^2$$

$$= R u_i^2$$

Joint 2 fit the form exactly with $\dot{\Theta}_2 = 22.5\ U_2$. Because of the second order term in the linearized equation for joint 1, however, a similar form did not exist for $\dot{\Theta}_1$ and U_1. To alleviate this, a reversion back to the first order approximation of joint 1 motion was required <u>for the purpose of merit function evaluation only</u>. As discussed earlier, a satisfactory fit at lower frequencies was found for the (K s) joint 1 model, but increasing deviation at higher frequencies was observed. Actual observation of the link in operation indicated that the higher frequency dynamics occured mainly in the transition from static equilibrium to sustained motion, and vice versa. For the majority of the operating region much lower velocities were encountered.

Based on this it was felt that, although the approximation was not accurate over the entire operating spectrum, reasonable results could be obtained for power comparisons with the (K/s) model for link 1. This led to the following R matrix based on first order models for both joints:

$$R = \begin{bmatrix} 80473 & 0 \\ 0 & 78400 \end{bmatrix}$$ (Eqn. 49)

The Q state weighting matrix took the form of a reduced identity matrix I. The states that were considered important were Θ_1, $\dot{\Theta}_1$, and Θ_2. Minimizing the feedback states of past inputs, or $u_i(n-1)$, was felt to have no real utility

$$Q = \begin{bmatrix} 1 & 0 & 0 & 0 & 0 \\ 0 & 1 & 0 & 0 & 0 \\ 0 & 0 & 1 & 0 & 0 \\ 0 & 0 & 0 & 0 & 0 \\ 0 & 0 & 0 & 0 & 0 \end{bmatrix}$$ (Eqn. 50)

and hence was ignored. Although discussed only briefly in most control texts, the proper selection of Q is the major factor in determining which states the controller will emphasize in optimizing plant performance.

In order to ascertain the affect that various magnitudes of λ (Eqn. 38) have on power minimization, three trial values were chosen. The first value of 30, was picked specifically to show a situation where both valve 1 and 2 intial voltages were in the saturated region. The second value of 15 placed the intial voltages at the saturation boundary. The final value of 1 produced valve inputs that remained in the acceptable performance range throughout the move.

55

F.   CALCULATION OF THE GAIN MATRIX K

With Φ, Γ, R, and Q determined, the Riccati equation was solved for K. The following values were obtained.

$$K_{\lambda=1} = \begin{bmatrix} 3.52(10^{-3}) & 1.08(10^{-5}) & 0 & 7.17(10^{-5}) & 0 \\ 0 & 0 & 3.56(10^{-3}) & 0 & 3.2(10^{-3}) \end{bmatrix} \quad (Eqn.\ 51)$$

$$K_{\lambda=15} = \begin{bmatrix} 1.37(10^{-2}) & 4.17(10^{-5}) & 0 & 2.78(10^{-4}) & 0 \\ 0 & 0 & 1.37(10^{-2}) & 0 & 1.24(10^{-2}) \end{bmatrix} \quad (Eqn.\ 52)$$

$$K_{\lambda=30} = \begin{bmatrix} 1.93(10^{-2}) & 5.89(10^{-5}) & 0 & 3.94(10^{-4}) & 0 \\ 0 & 0 & 1.93(10^{-2}) & 0 & 1.74(10^{-2}) \end{bmatrix} \quad (Eqn.\ 53)$$

VI. MICRO-COMPUTER IMPLEMENTATION

A. CONTROLLER SAMPLE RATE

Determination of the correct controller sample rate for the IBM PC AT in conjunction with the NEPTUNE arm was a two part process. First, an offline software test was conducted to determine the time required for the execution of the complete control algorithm. After this was accomplished, an examination of the arm model was performed to predict the minimum sample rate that was needed perform the ADC, control, and DAC while still maintaining system stability.

The offline software test consisted of coding the entire control loop in Fortran, and compiling. This test code was then iterated 5000 times, and the elapsed time was recorded. The results of this test produced an average computer control cycle period of 2.57 milli-seconds. As a general rule of thumb, it was decided that the control computation time should not exceed 60% of the computer control sample period. The reasoning behind this was that system overhead time would be required for sensor acquisition, conversion, and computer "housekeeping" chores. For LABPAC this overhead time is approximately 0.8 milli-seconds, making the minimum computer sample period 3.37 milli-seconds.

Shannon sampling criteria was used to determine the minimum sample frequency required to enable reconstruction of the sampled motion [Ref. 1]. Since the highest frequency pole was associated with joint 1 at 3.6 Hz, the lowest acceptable sample frequency for the system was set at 7.2 Hz, with a recommended sample frequency of 36 Hz. This equated to a sample period for

system stability of between .028 (recommended) and .139 (required) seconds. Use of the recommended sample rate, however, meant that the transportation lag of 0.04 seconds would extend over two sample periods. A compromise .05 second (50 msec) sample period (20 Hz) was implemented, thus making the duty cycle (3.37 msec) less than 10% of the sample rate.

B. POWER DATA COMPARISONS

A total of four comparison runs were performed with the arm. The first three runs used the gain matricies that corresponded to the three previously discussed values of λ. The last run utilized the solenoid control as originally configured on the NEPTUNE to provide a baseline for comparison. The start point for each run was $\Theta_1 = 20$ degrees, $\Theta_2 = -60$ degrees; with the end point being $\Theta_1 = 70$ degrees, $\Theta_2 = 30$ degrees. Figures 21,22 show time-motion plots of joints 1 and 2. Each link shows expected results, with the optimal control runs approaching their desired set points assymtotically. It should be noted here that in the case of $\lambda = 1$, the target position was never actually reached. Θ_2 finally ended 3 degrees short of the desired position, because valve input - Kx was in the deadband voltage for that small error condition . In comparison, the solenoid runs approached the target positions with constant velocity, and motion was slowed by use of the fluid restrictors. When the link was within the error deadband, motion was stopped by shutting the solenoid valve.

Figures 23,24,25 compare total hydraulic power consumption for the arm ($\Sigma(P_{1_i}-P_{2_i})q_i$) with solenoid power consuption, for the specified λ's. The negative power values that appear for the solenoid and $\lambda = 1$ move, are attributable to the fact that the joint 1 return springs were providing all forces
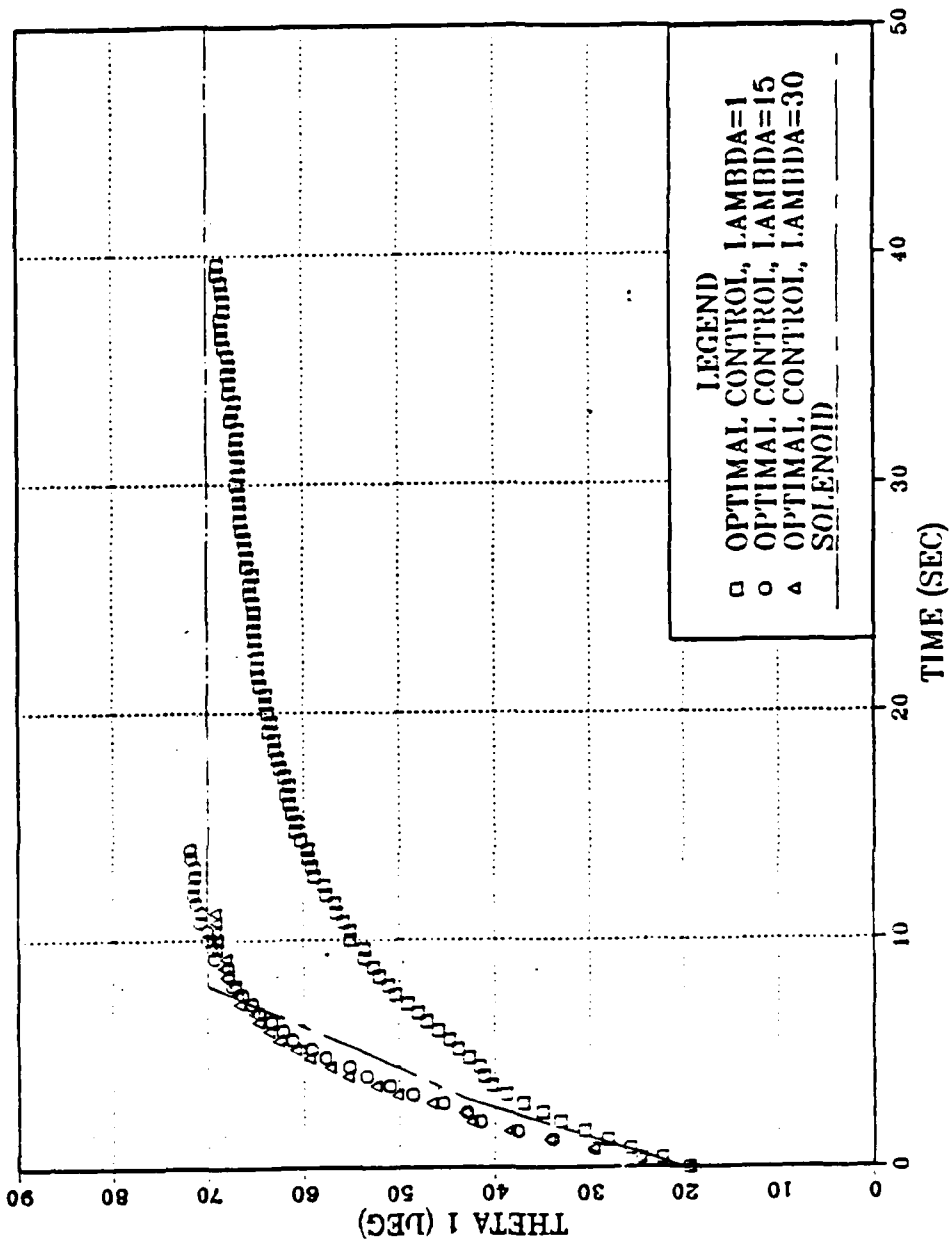
Figure 21
Joint 1 position plot

59
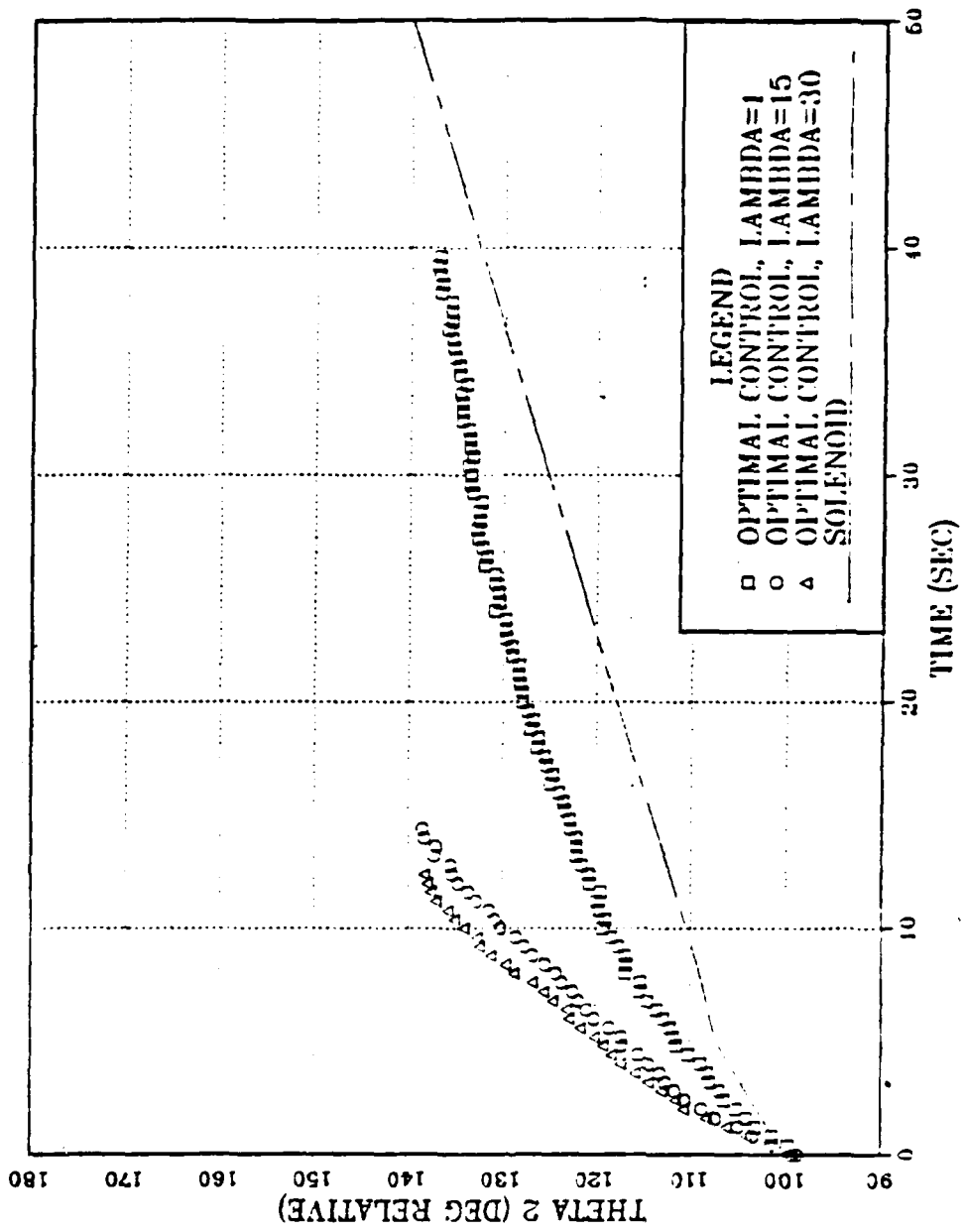
Figure 22
Joint 2 position plot

60
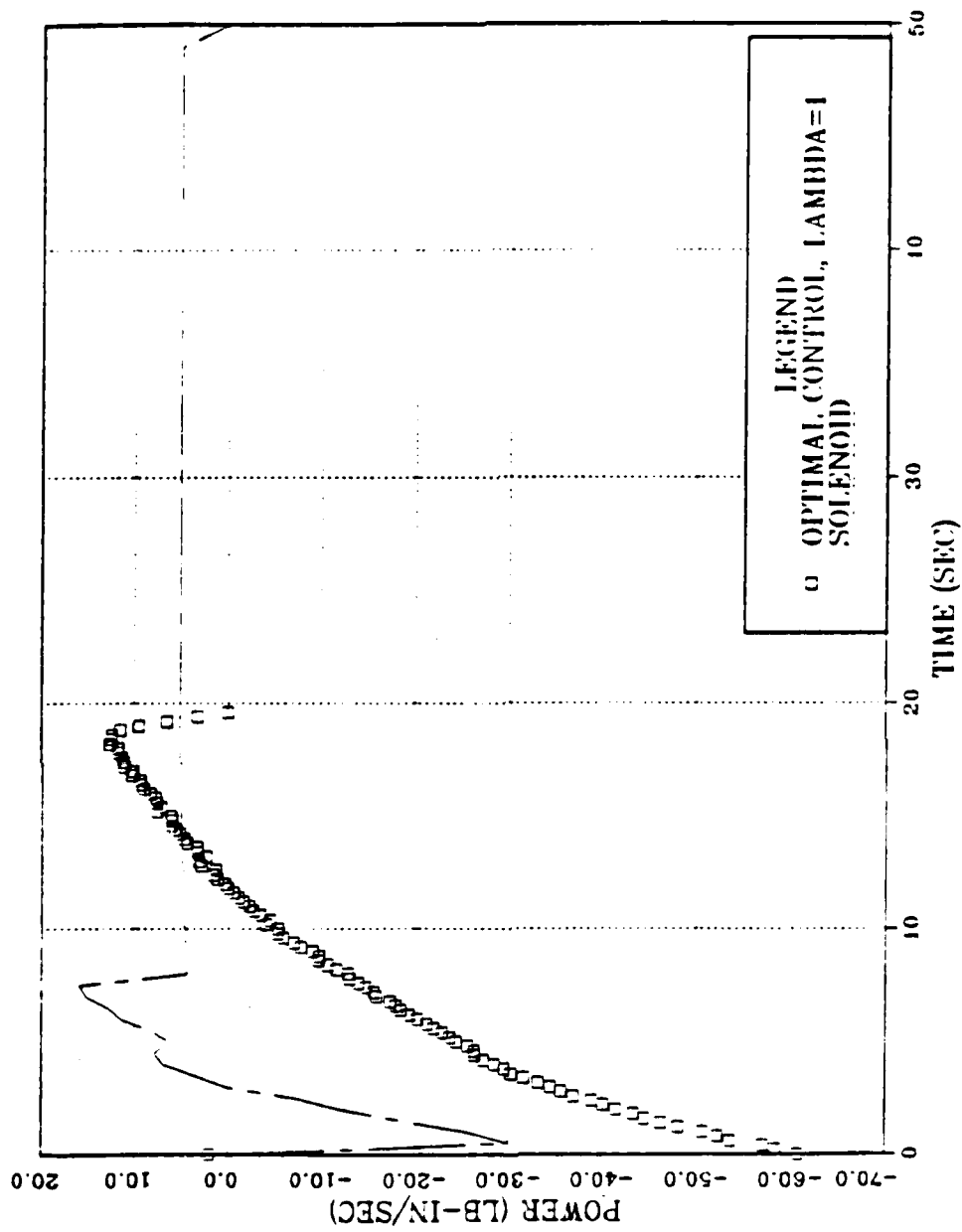
Figure 23
Total arm power - $\lambda = 1$

61
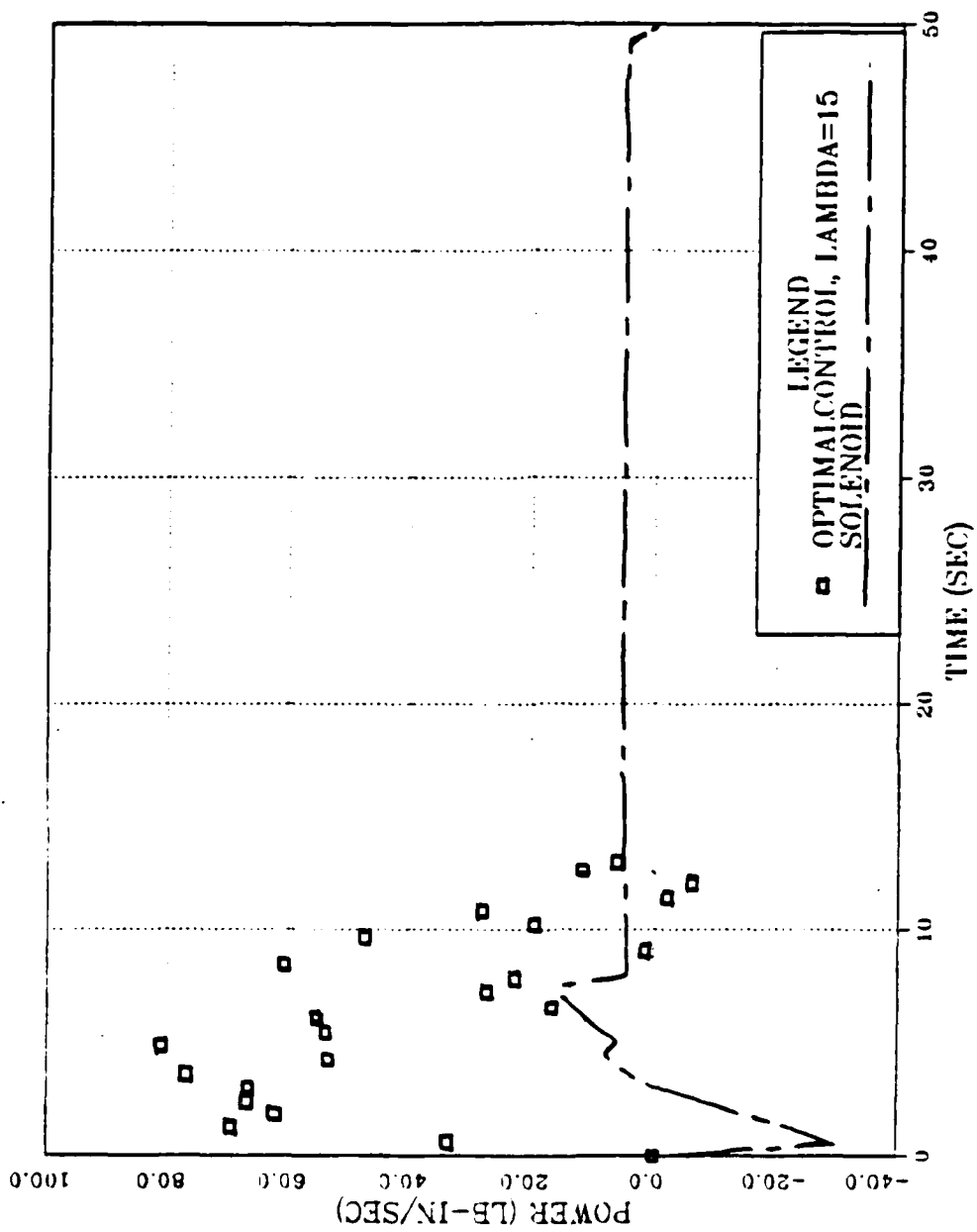
Figure 24
Total arm power - $\lambda = 15$
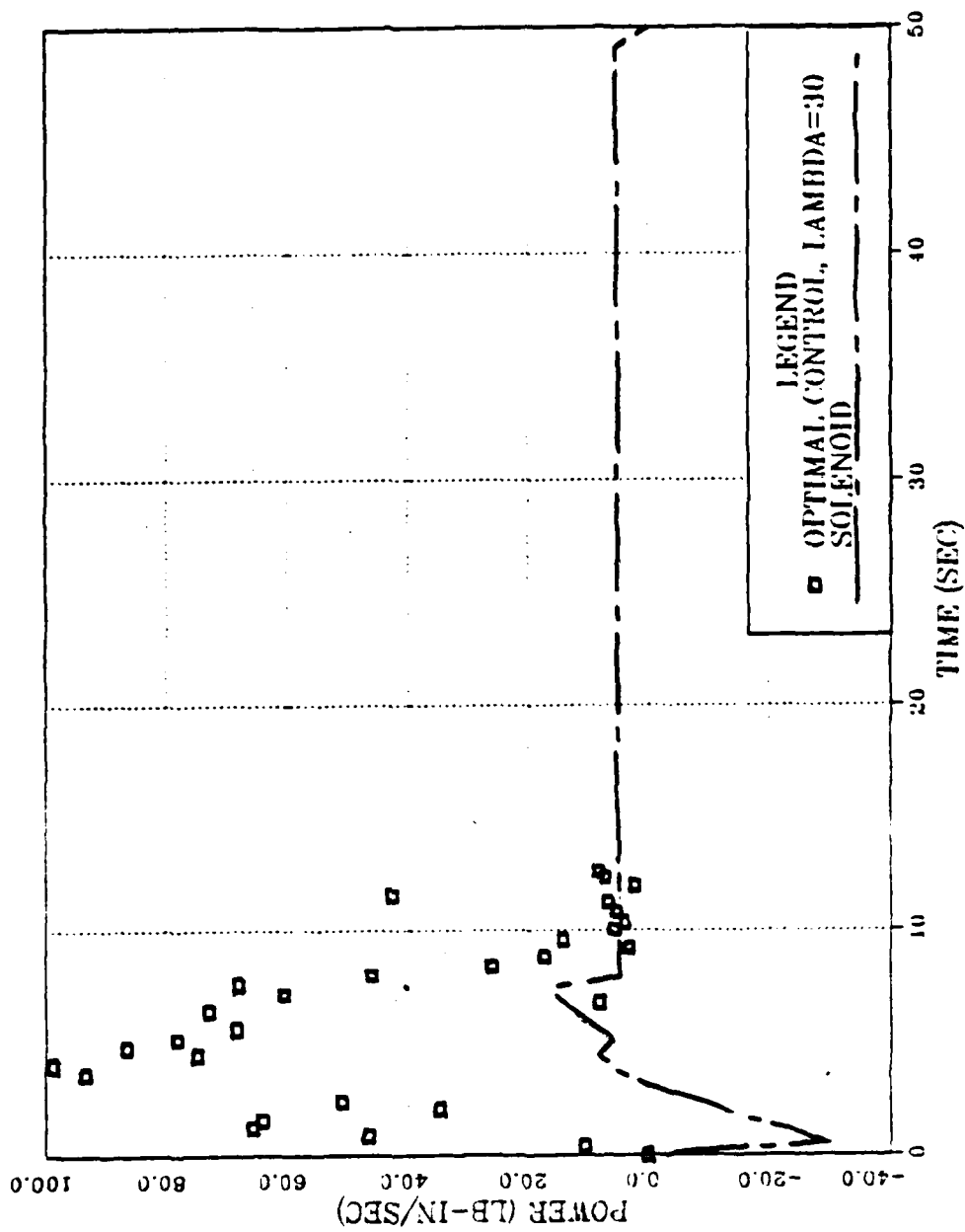
Figure 25
Total arm power - $\lambda = 30$

necessary for motion of link 1 until Θ_1 exceeded 35 degrees. This phenomenon was not evident for $\lambda = 15$, or $\lambda = 30$. As λ increased from 1 to 30, the maximum instantaneous power used by the arm was correspondingly higher reflecting increased weight on error. Accurate values for the actual power used by the arm were difficult to determine, largely because of the noise from the position feedback potentiometers, and random errors in ADC. However, a general trend can be discerned that shows $\lambda = 1$ had a lower maximum power requirement than did the solenoid. The sawtooth like curve of the solenoid operation correlates with fluid restrictor closing. The power requirements for all optimal control moves appear to transition smoother, from high to low values. This can be advantageous, especially in hydraulic systems, where sudden shocks are not desired.

Total system power plots (power taken from accumulator with Ps assumed constant) show results consistent with arm power results. $\lambda = 30$ and 15 plots (Fig. 26,27) show that the power used by the system always exceeds solenoid power requirements. In contrast, the power requirements for $\lambda = 1$ somewhat closely matches that of the solenoid (Fig. 28). The major deviation is the initial power surge for the servovalve operation. Once again, transitions in power levels were smoother in optimal control than solenoid control.
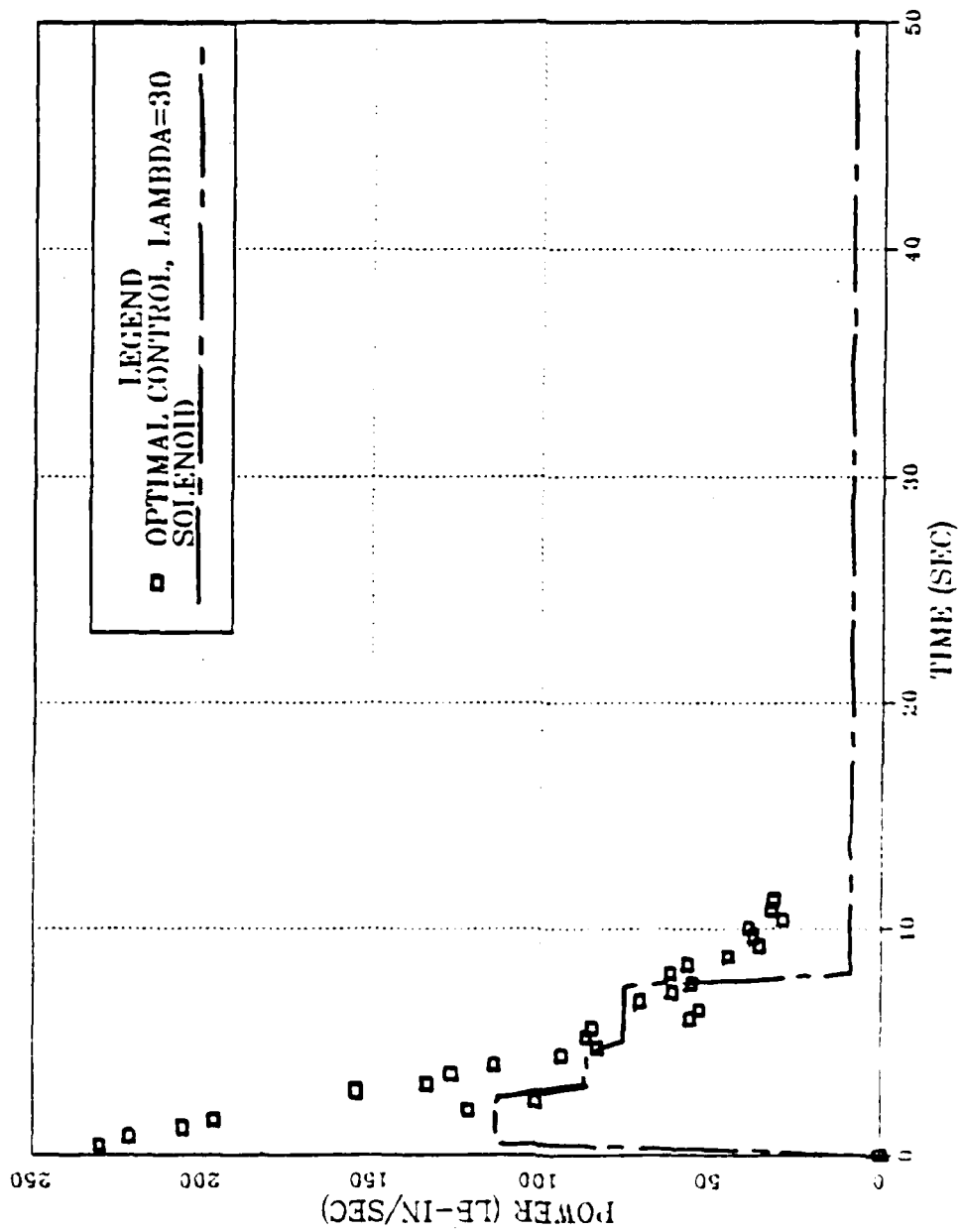
Figure 26
Total system power - $\lambda = 30$

65
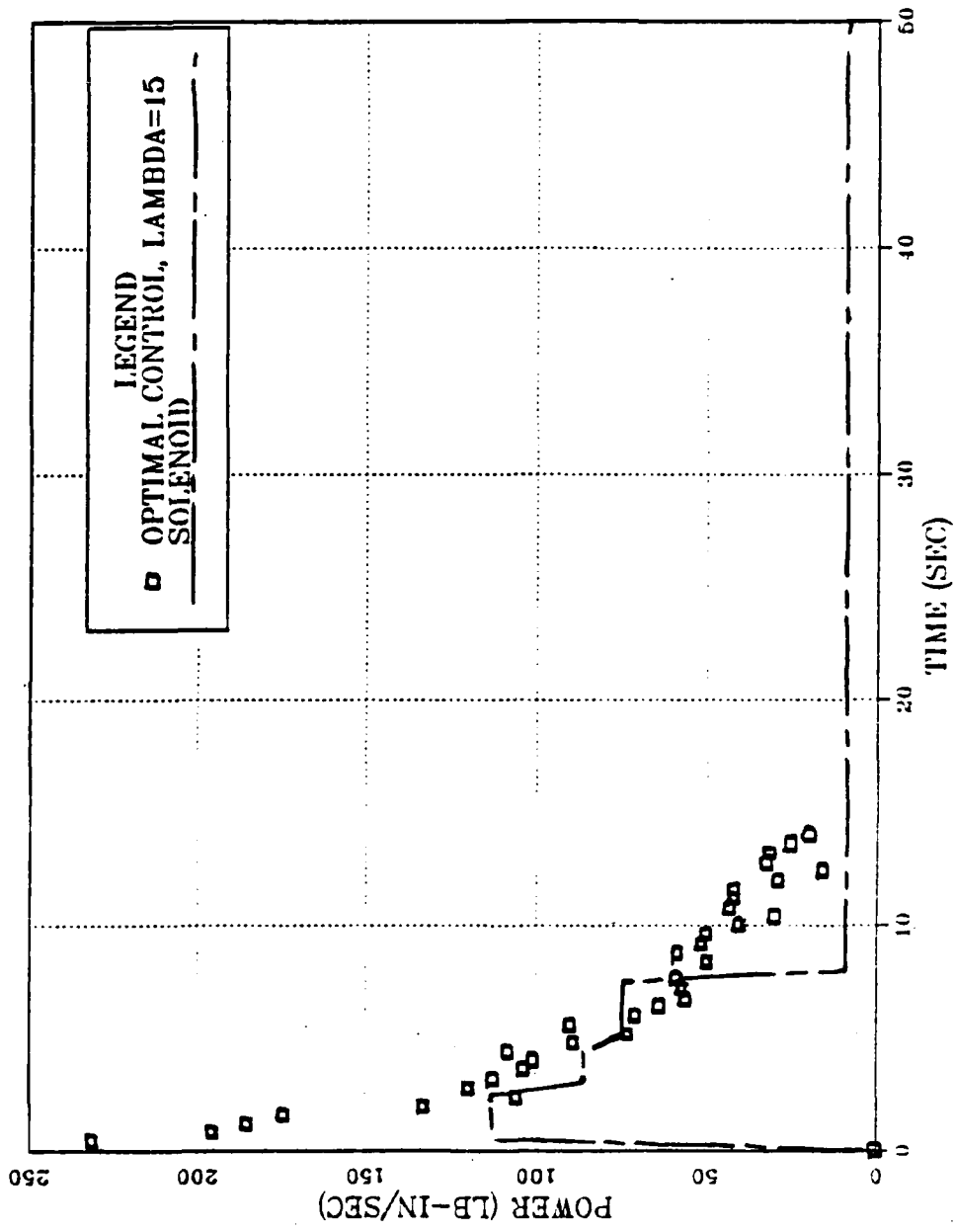
Figure 27
Total system power - $\lambda = 15$

66
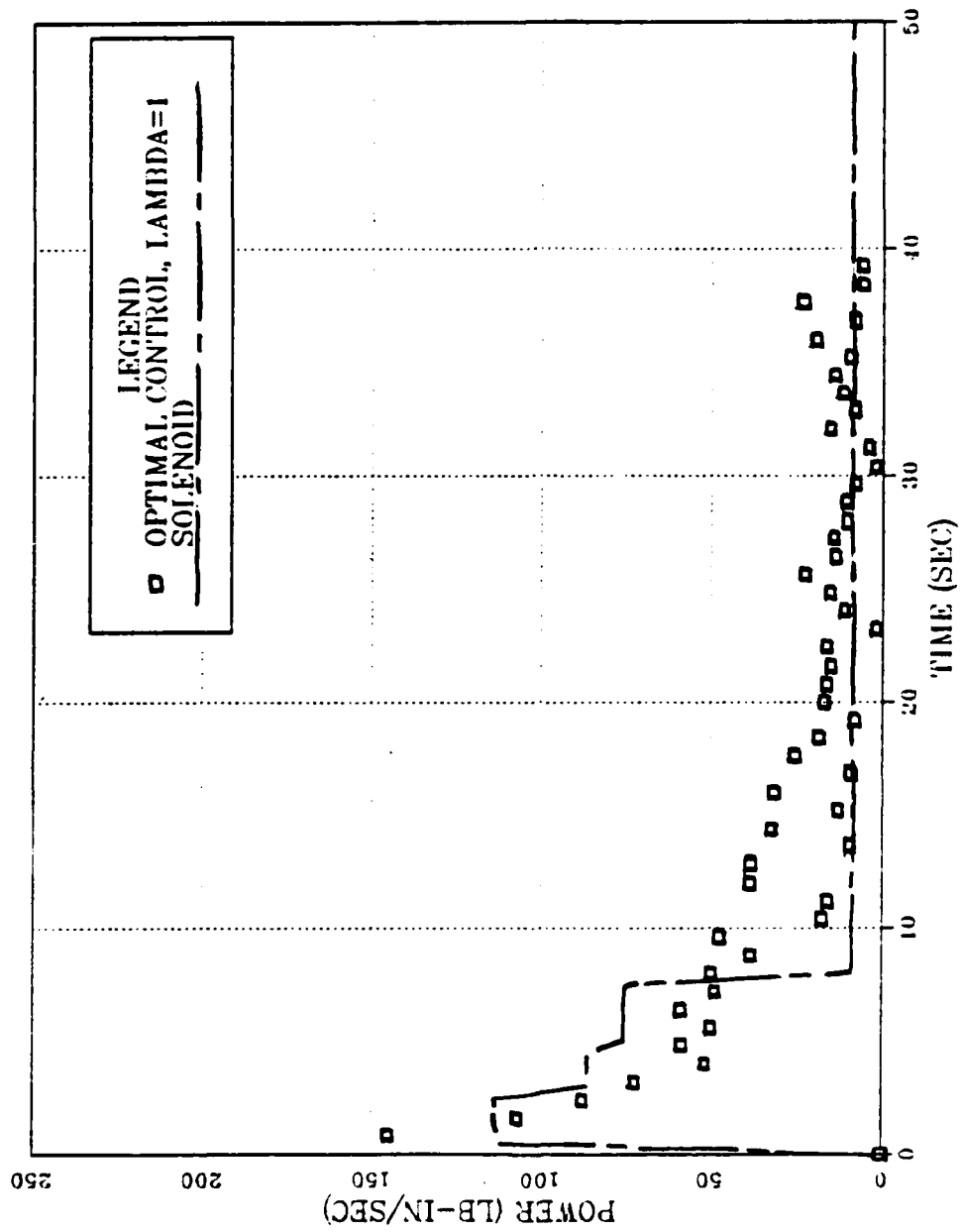
Figure 28
Total system power - $\lambda = 1$

67

VII. CONCLUSIONS

A. SYSTEM LINEARITY

The intial evaluation of the equations of motion for the NEPTUNE system were based on the assumption that the rotational inertia of the arm structure was dominant. This in fact was not the case with the NEPTUNE. With the servovalves installed, the dominant mechanism for determining motion, was the combination servovalve and actuator assembly. Even at relatively low pressures, the NEPTUNE behaves linearly. In essence, the hydraulic system has enough power to override much of the low performance dynamics that might have been expected.

B. SERVOVALVE PERFORMANCE

The data that was obtained for the servovalve did not reflect the anticipated classical valve model. The reason for this is believed to be the relatively low system pressure and the distance between the servovalves and pressure sensors. It was felt that by correcting these factors, better correlation may be obtained. Nevertheless, equivalent linearization techniques were used to adequately model both the valve and arm performance as configured in the present study.

C. MICRO-COMPUTER OPTIMAL CONTROL

Micro-computer optimal control is a simple to implement, feasible control scheme. The control system can be "tuned" to the desired performance level by the proper choice of weighting matrices Q and R. Additionally, a smooth transition in motion and hydraulic power requirements can be expected.

D. SAMPLE RATE

Since the NEPTUNE was of such low performance, the maximum sample rate available with the IBM PC-AT was adequate. The driving concern in sample rate determination was the proper handling of the transportation delay. Finally, although the selected sample rate was less than a recommended five times the Shannon sampling criteria, system stability was not affected.

VIII. RECOMMENDATIONS

Continue the use of NEPTUNE plus IBM PC-AT as a test bed for controller development. Three future projects are recommended as follow on work. First, a three dimensional optimal controller should be implemented in order to utilize the full range of motion on the NEPTUNE arm. Second, comparison studies of optimal versus Proportional-Integral-Derivative (PID) control should be conducted, to provide a better baseline evaluation against a common type of controller found in industry. Finally, the NEPTUNE and IBM PC-AT should be configured to perform more intelligent types of control such as: adaptive, obstacle avoidance, etc.

Additionally, the following hardware improvements should be made to the system. First, it is recommended that the system pressure be increased to that specified by the valve manufacturer, and the system should be remodeled. It is also recommended that the rack and pinion joint transmission gears be redesigned to remove or minimize backlash. Lastly, digital shaft encoders should be installed to increase the accuracy of joint position feedback.

APPENDIX
OPTIMAL CONTROL PROGRAM

```
$include:'labhead.for'
$include:'master.for'
$include:'dadio.for'
        dimension  chan(6),databuf(6,2500)
        real*4 volt,runt,term1,term2,svlt1r,svlt2r,kopt(2,5),deltj1,deltj2
        real*4 stpt1,stpt2,endpt1,endpt2,lambda,thdot1
        logical flag1,flag2

c constants
        th1zero = 41
        th2zero = 1300
        th1nint = 2620
        th2nint = 3835
        th1rng = th1nint-th1zero
        th2rng = th2nint-th2zero
        count = 1
        runt = 40
        nsweep = runt*20
        dither = 10

c set channel numbers to be scanned

        chan(1) = 1
        chan(2) = 2
        chan(3) = 6
        chan(4) = 7
        chan(5) = 8
        chan(6) = 9


c  reset and initialize labpac


        result = labpac(RESET)
        result = labpac(ATOD,12,AIINIT)

c initialize dadio board for digital to analog output

        result = labpac(DA,4,AOINIT)
        result = labpac(7,125,TIMER,SWINIT)
        result = labpac(0,0,AORAW)
        result = labpac(1,0,AORAW)


c read in the starting and ending joint positions
```

71

```fortran
400     write (*,*) 'ENTER JOINT 1 STARTING POSITION (DEGREES) :'
        read (*,*) stpt1
        write (*,*) 'ENTER JOINT 1 ENDING POSITION (DEGREES) :'
        read (*,*) endpt1
        write (*,*) 'ENTER JOINT 2 STARTING POSITION (DEGREES) :'
        read (*,*) stpt2
        write (*,*) 'ENTER JOINT 2 ENDING POSITION (DEGREES) :'
        read (*,*) endpt2
        write (*,*)
        write (*,*)

c read in the array of control feedback constants

        write(*,*) 'ENTER THE FILE NAME THAT CONTAINS THE K
     +  MATRIX'
        write (*,*)
        open (12, file='',status='old')
        read(12,*) lambda
        do 50 i=1,2
50      read (12,*) kopt(i,1),kopt(i,2),kopt(i,3),kopt(i,4),kopt(i,5)


c move joint 1 and 2 to starting position

        pause 'TURN ON MASTER SERVO POWER SWITCHES'
        flag1 = .false.
        flag2 = .false.
        term2 = stpt1/90.*th1rng
        iterm2 = ifix(term2)
100     th1 = labpac(1,AIRAW)
        delth1 = th1-iterm2
        svlt1r = -(delth1*2047.)/th1rng
        svolt1 = ifix(svlt1r) + dither
        if (svolt1 .lt. -2047) then
         svolt1 = -2047
        endif
        if (svolt1 .gt. 2047) then
         svolt1 = 2047
        endif
        if (abs(delth1) .le. 15) then
         result = labpac(0,0,AORAW)
         flag1 = .true.
        else
         result = labpac(0,svolt1,AORAW)
         flag1 = .false.
        endif
        th2 = labpac(2,AIRAW)
        term1 = stpt2*(th2rng/90.)
        iterm1 = ifix(term1)
        delth2 = th2-th2nint-iterm1 + th1
        svlt2r = -(delth2*2047.)/th2rng
```

72

```fortran
        svolt2 = ifix(svlt2r) + dither
        if (svolt2 .lt. -2047) then
         svolt2 = -2047
        endif
        if (svolt2 .gt. 2047) then
         svolt2 = 2047
        endif
        if (abs(delth2) .le. 15) then
         result = labpac(1,0,AORAW)
         flag2 = .true.
        else
         result = labpac(1,svolt2,AORAW)
         flag2 = .false.
        endif
        if (flag1 .and. flag2) then
         goto 200
        endif
        dither = -dither
        goto 100


c  commence optimal control and data acquisition run

200     write(*,*)
        pause 'READY TO COMMENCE OPTIMAL CONTROL MOVE'

c convert theta 2 from global to relative
        endpt2 = 180.-endpt1 + endpt2

        swleft = nsweep-1
        lstout1 = 0.
        lstout2 = 0.
        result = labpac(1,NSWEEP,6,CHAN,DATABUF,AISWST)


c optimal control algorithm with 20th of a second time delay
c between control sweeps

300     result = labpac(SWLEFT,AISTAT)
        deltj1 = float(databuf(1,count)-th1zero)*90./float(th1rng)-endpt1
        deltj2 = float(databuf(2,count)-th2zero)*90./float(th2rng) + 90.
    +-endpt2
        if(((abs(deltj1).le. 1.) .and. (abs(deltj2).le. 1.)) .or. (swleft
    +.eq. 0)) then
         result = labpac(0,0,AORAW)
         result = labpac(1,0,AORAW)
         result = labpac(AISWAB)
         stop
        endif
        thdot1 = float(databuf(1,count-1)-databuf(1,count))*1800./float
    +(th1rng)
```

73

```
      svlt1r = -kopt(1,1)*deltj1-kopt(1,2)*thdot1-kopt(1,3)*deltj2-
     +kopt(1,4)*lstout1-kopt(1,5)*lstout2
      svolt1 = ifix(svlt1r*2047/10. + dither)
      svlt2r = -kopt(2,1)*deltj1-kopt(2,2)*thdot1-kopt(2,3)*deltj2-
     +kopt(2,4)*lstout1-kopt(2,5)*lstout2
      svolt2 = ifix(svlt2r*2047/10. + dither)
      result = labpac(0,svolt1,AORAW)
      result = labpac(1,svolt2,AORAW)
      lstout1 = svlt1r
      lstout2 = svlt2r
      count = count + 1
      swleft = swleft-1
      dither = -dither
      go to 300
      end
```

LIST OF REFERENCES

1. Naval Surface Weapons Center Report MP84-478,
    Applications of Robotics and Artificial IntelligenceFor Ship Operations
    and Mission Activities-An OverviewVolume 1, by S. Hogge, 1 May 1985.

2. NAVSEA Office of Robotics and Autonomous Systems SEA-90G,
    Robotics Development inSupportof Naval Operations,
    by Science Applications International Corporation, 29 August 1985.

3. Office of Robotics and Autonomous Systems SEA-90G
    Report 450-90G-TR-0003, Naval Sea Systems Command Integrated
    Robotic Program Annual Report, FiscalYear 1985, by LCDR H. R.
    Everett, December 1985.

4. Lewis, D. R., Modeling of a Low Performance Rigid Revolute Robot Arm,
    M.S. Thesis, Naval Postgraduate School, Monterey, California,
    December 1985.

5. Burrill, L. D., A Feasibility Investigation for Optimal Control,
    M.S. Thesis, Naval Postgraduate School,
    Monterey, California, September 1986.

6. Ogata, K., Modern Control Engineering, Prentice-Hall Inc.,
    New Jersey, 1970.

7. Owens, D. H., Multivariable and Optimal Systems, Academic Press Inc.,
    New York, 1981.

8. Merritt, H. E., Hydraulic Control Systems, John Wiley& Sons Inc.,
    New York, 1967.

9. Denavit, J. and Hartenberg, R. S., A Kinematic Notation For Lower-Pair
    Mechanisms Based on Matrices, Journal of Applied Mechanics, V. 22,
    No. 2, 215-21, June 1955.

10. Guo, T.H. and Koivo, A.J., "Microprocessors Implementation
    of an Adaptive Controller for Robotic Manipulators", pp.641-6 in: IEEE
    Computer Society Conference on Pattern Recognition and Image
    Processing, 1982. Proceedings of PRIP 82.

11. Gobburu, V. T. and Doty, K. L., "A Novel Design Principle
    For Microprocessor Based 6-DOF Manual Controllers", pp.178-83 in:
    IEEE Southeastcon 1981 Conference Proceedings.

12. Rafauli, R., Sinha, N., and Tlusty, J., "A Microprocessor Control System
    For An Industrial Report",International Electrical Electronics
    Conference and Exposition, 1981.

13. Bertino, M., Furxhi, M. G., and Gola, M., "Microcomputer Control for a 5 Axis Manipulator With Cartesian PathControl", pp. 1078-84 in: <u>International Conference on Cybernetics and Society</u>, 1980. Proceedings.

14. Klein, C. A. and Briggs, R. L., "Minicomputer and Microcomputer Control of Mechanical Linkage Systems", <u>National Electronics Conference</u>, pp. 186-90 in: 32nd, 1978.Proceedings.

15. Snyder, W. E. and Gruver, W. A., "Microprocessor Implementation of Optimal Control For a Robotic Manipulator System", Part II, pp. 839-41 in: <u>IEEE Conference</u>, 18th, 1979. Proceedings.

16. Kim, Byung Kook and Shin, Kang G., <u>Suboptimal Control of Industrial Manipulators With a Weighted Minimum Time-Fuel Criterion</u>, IEEE Transactions on Automatic Control, V. AC-30, No. 1, January 1985.

17. Koozekanani, S. H., and others, <u>On the Role of Dynamic Models in Quantitative Posturography</u>, IEEE Transactions on Biomedical Engineering, V. BME-27, No. 10, 605-9, October 1980.

18. Astrom, K. J. and Wittenmark, B., <u>Computer Controlled Systems Theory and Design</u>, Prentice-Hall Inc., New Jersey, 1984.

Section IV

Robot Firefighter Drilling Loads

TABLE OF CONTENTS

LIST OF VARIABLES

A   The cross-sectional area (in^2)

c   The distance from the neutral axis to the most extreme fiber (in)

$\bar{d}$ Support tube mean diameter (0.9 in)

E   Young's Modulus of Elasticity (29,000,000 lbs/in^2)

F_{r_x}, F_{r_y}, F_{r_z} Resultant forces for an arbitrary point on the support tube cylinder (lbs)

F_1, F_2, F_3 Load forces at the penetrator tip (lbs)

G   Shear Modulus of Elasticity (lbs/in)

I   The moment of inertia of the cross-section with respect to the neutral axis (in^4)

J   The polar moment of inertia of the cross-section relative to its centroid (in^4)

L_{21}, L_{22} The distance from the centerline of the drill to the critical points on the support cylinder surface ($L_{21} = 2.75$ in and $L_{22} = 6.75$ in)

M   Bending moment (in-lbs)

M_{r_x}, M_{r_y}, M_{r_z} The resultant moments for an arbitrary point on the cylinder (in-lbs)

M_1, M_2, M_3 The load moments at the penetrator tip (in-lbs)

P   Transmitted force (lbs)

Q   The first moment of the area with respect to the neutral axis (in^3)

$\bar{r}$ Support tube mean radius (0.45 in)

r_i Inside radius of the support cylinder (0.4 in)

r_o Outside radius of the support cylinder (0.5 in)

t   Radial thickness of the support cylinder (0.1 in)

T	Torque (in-lbs)
V	Transverse shear force (lbs)
α	The angle between a force vector and the x axis (degrees)
β	The angle between a force vector and the y axis (degrees)
γ	Shear strain (in/in)
$\gamma_{xy}, \gamma_{yz}, \gamma_{zx}$	The shear strain where the first subscript denotes the plane face on which the strain acts and the second the direction on that face (in/in)
$\gamma_{yz_B}(L_{21})$	The shear strain at the point B a distance L_{21} from the centerline of the penetrator (in/in)
δ	The angle between a force vector and the Z axis (degrees)
ε	Normal strain (in/in)
$\varepsilon_x, \varepsilon_y, \varepsilon_z$	The normal strain where the subscript denotes the plane face on which the strain acts (in/in)
ε_{yz}	A strain measured by a rosette gage element in the Y-Z plane (in/in)
$\varepsilon_{y_A}(L_{21})$	The normal strain at a point A on the cylinder a distance L_{21} from the centerline of the penetrator (in/in)
$\varepsilon_{y_A}(L_{22})$	The normal strain at a point A on the cylinder a distance L_{22} from the centerline of the penetrator (in/in)
$\varepsilon_{y_A}(L_{21})$	The normal strain at a point B on the cylinder a distance L_{21} from the centerline of the penetrator (in/in)
$\varepsilon_{y_A}(L_{22})$	The normal strain at a point B on the cylinder a distance L_{22} from the centerline of the penetrator (in/in)
$\varepsilon_{y_B}(L_{21})$	The normal strain at a point C on the cylinder a distance L_{21} from the centerline of the penetrator (in/in)

$\varepsilon_{yz_B}(L_{21})$ The Y-Z plane strain at a point B on the cylinder a distance L_{21} from the centerline of the penetrator (in/in)

$\varepsilon_{z_{B}(L_{21})}$ The normal strain at a point B on the cylinder a distance L_{21} from the centerline of the penetrator (in/in)

θ An angle in the X-Z plane measured from the X axis (degrees)

ν Poison's ratio (0.29)

σ Normal strain (lbs/in)

$\sigma_x, \sigma_y, \sigma_z$ The normal stress where the subscript denotes the plane face on which the strain acts (lbs/in)

$\sigma_{y_A}, \sigma_{y_B}, \sigma_{y_C}$ The normal stress acting on the Y plane face at the points A, B, and C

$\sigma_y(r, \theta)$ The normal stress acting on the Y plane face as a function of the variables r and θ (in/in)

τ Shear stress (lbs/in)

$\tau_{yx_A}, \tau_{yz_B}, \tau_{yx_C}$ The shear stress at the points A, B, and C where the first subscript denotes the plane face on which the stress acts and the second the direction on that face (in/in)

81

I. INTRODUCTION

A. PROBLEM DESCRIPTION

An aircraft skin penetrator/applicator was developed by the USAF as a device for penetrating an aircraft fuselage and injecting Halon into the interior of the aircraft to extinguish fires [Ref. 1]. The guidelines for the present study and other related Naval Postgraduate School work were to investigate the requirements for a robot arm to manipulate such a tool. The purpose of this work was to identify the loads that the support structure would have to sustain during a drilling operation with the device. In general, the loads are functions of the material characteristics of the drilling surface and the drill parameters, i.e., type drill bit, length of the drill, feed rate, and angle of attack. For this investigation, the drill bit parameters were predetermined from previous work at the Naval Postgraduate School [Ref. 2]. Sheet aluminum was used to simulate the aircraft fuselage.

B. APPROACH

The approach was to experimentally determine the drill tip loads by selective support structure strain measurements. The analytical method used was to resolve the loads at the drill tip into six force and moment components about an orthonormal coordinate axes system (Figure 1). These
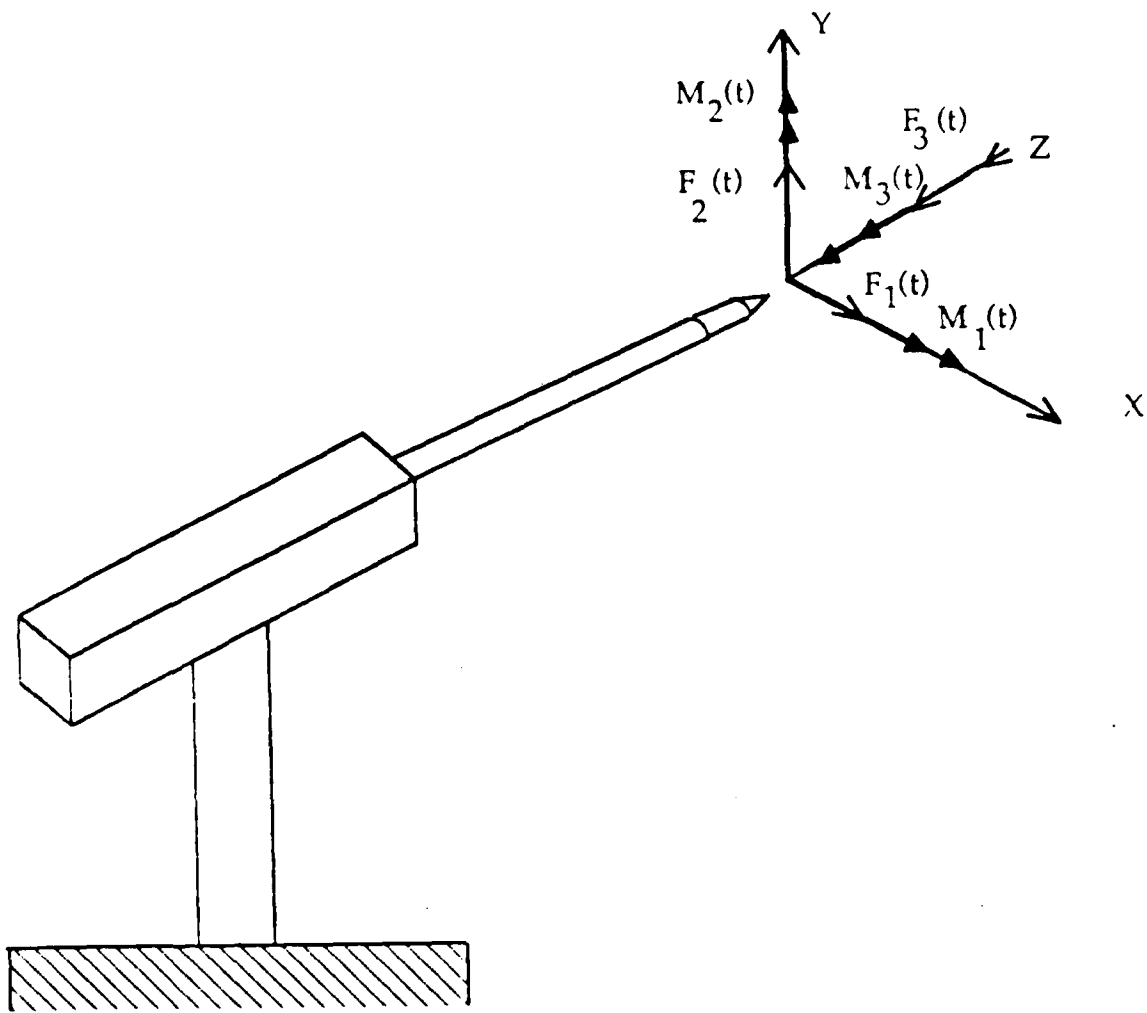
Figure 1.   Penetrator Forces and Moments

loads create a state of strain on the outer surface of the support structure which was analyzed by conducting a static force/moment equilibrium analysis and a solid mechanics analysis. The resulting strain equations were evaluated to determine a set of selective strain measurements which would facilitate segregation of the individual effects of each drill tip load. The analytical expressions for the strain at those locations were then used to find analytical expressions for the force/moment loads. In this way, the measured strains on the support structure were used to estimate the six forces and moments at the drill tip which are experienced during a drilling operation.

C. PREVIOUS WORK

Reference 2 is a previous study of the same problem with the assumption that the effects of certain forces and moments were negligible (Figure 2). Notice that only two forces (F_1 and F_3) and one moment (M_3) were previously assumed to be significant. The same methodology for determining analytical expressions for the force/moment components as functions of measured strain quantities was used in both studies, but the present study removes this restrictive assumption on the load magnitudes. The previous work also used an Operational Test and Evaluation drill to make measurements, while this investigation used a new drill supplied by the NSWC/White Oak laboratory.
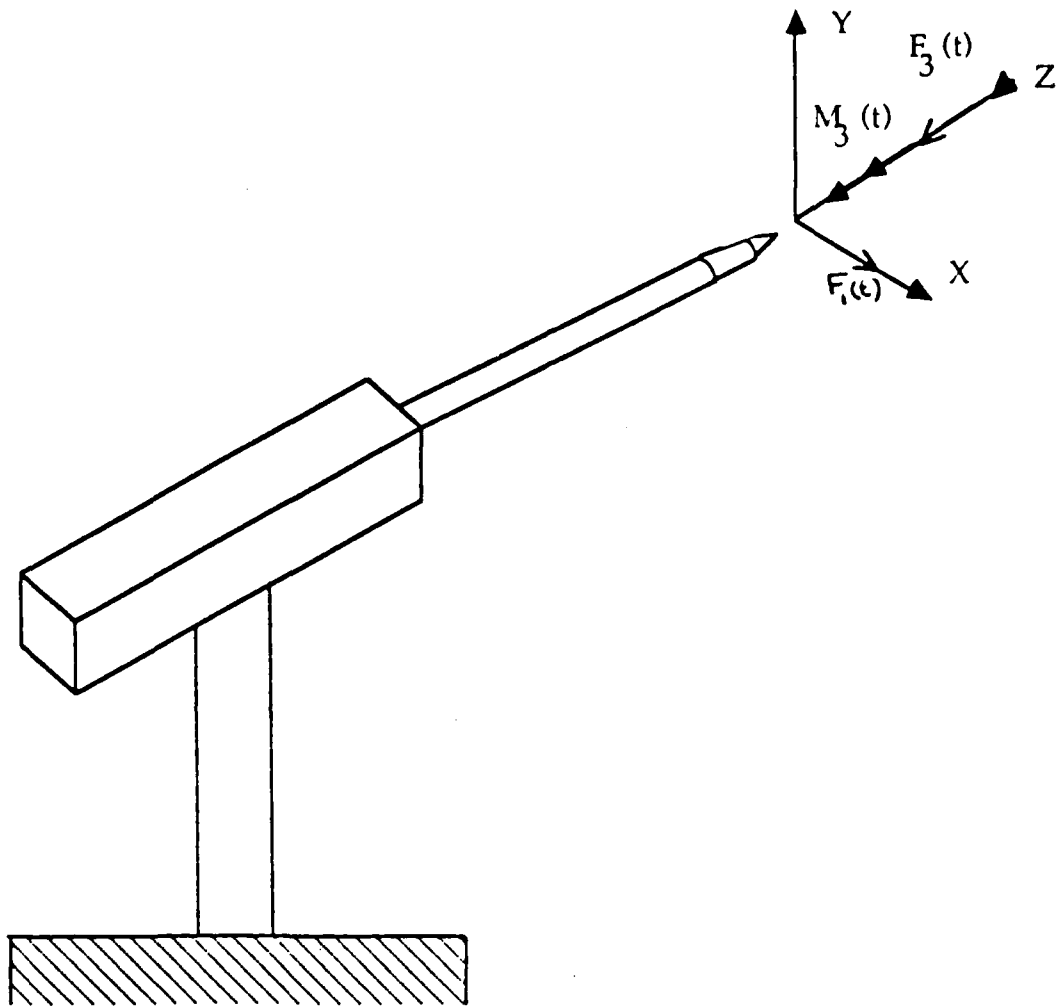
Figure 2. Penetrator Forces and Moments of Previous Work

85

II. EXPERIMENTAL EQUIPMENT

A. PENETRATOR ASSEMBLY AND FOUNDATION

1. Aircraft Skin Penetrator/Applicator

An AMETEK, Offshore Research and Engineering Division model ASP/AA-1 skin penetrator/applicator was utilized (Figure 3). For this work the carrier and bottle assemblies and the Halon ball valve were removed to facilitate installation on a milling machine bed. The drill was designed to be powered by compressed air carried by the operator. In the present work, a source of compressed shop air (165 psig) was used to power the drill.

2. Instrumented Support Fixture

A support fixture was manufactured from mild steel which consisted of a central cylinder with top and bottom support plates welded to its external radius. The penetrator was attached to the top plate with eight self-locking helicoil fasteners. The bottom plate was bolted to a milling machine bed. Five strain gages were mounted on the cylinder surface to facilitate the measurement of the cylinder deformation during a drilling operation.

3. Milling Machine

A Milwaukee model H milling machine, with mill removed, provided a movable foundation for the penetrator.

86
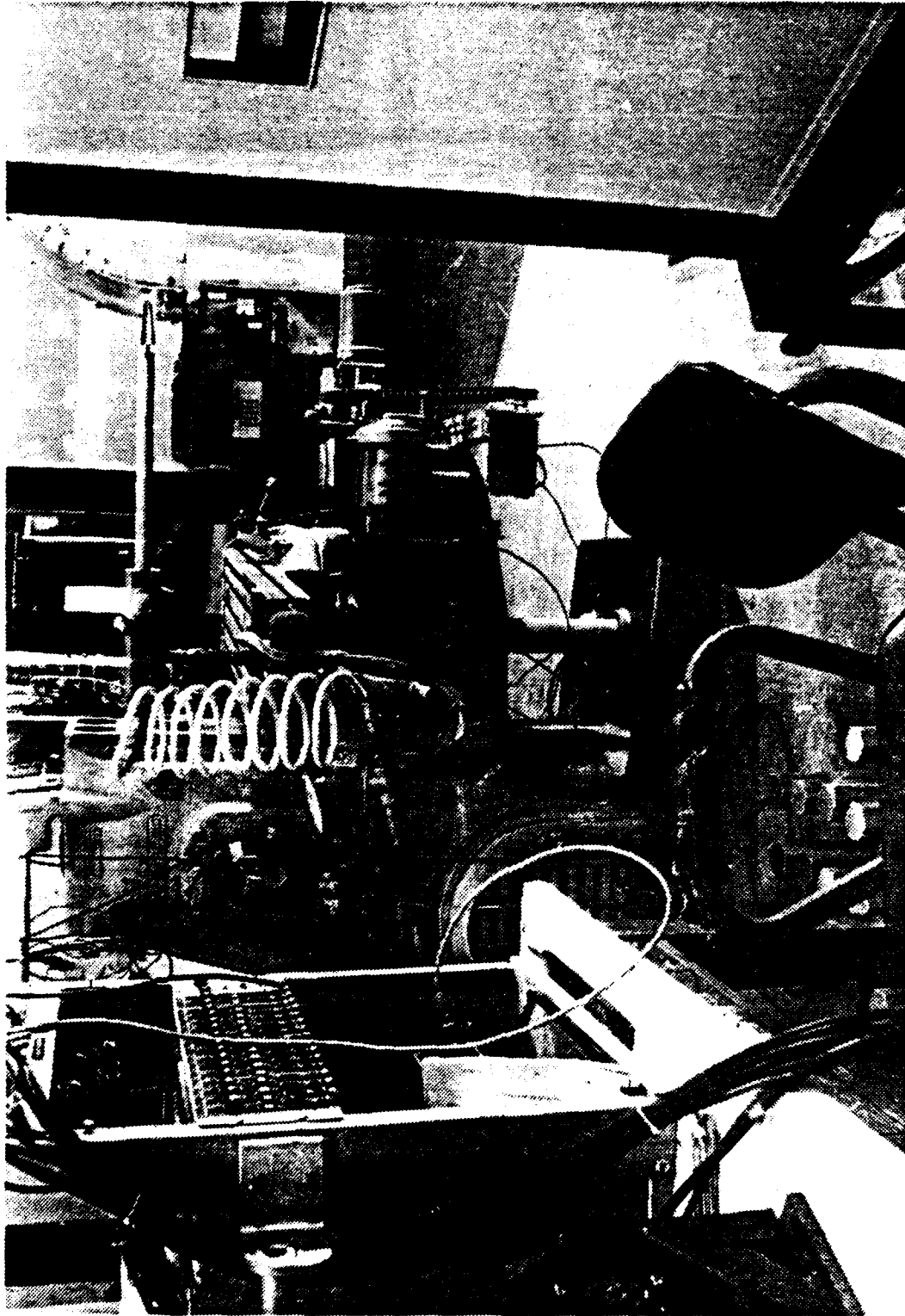
Figure 3. Experimental Equipment Left View

87

Two Superior Electronic synchronous/stepping motors, 72 RPM, 120 volts and 60 hertz, were installed on the milling machine's transversing gear assemblies and were controlled by 3-position switches. These motors provided for movement along the Y and Z directions at a constant speed of 14 inches/minute.

B. SIMULATED AIRCRAFT FUSELAGE

1. Test Panels

As in Reference 2, the aircraft fuselage was simulated by test panels constructed of 7075-T6 aluminum 0.050 inch sheets. The panels were rolled to the shape of the support frame.

2. Support Frame

The support frame with a test panel installed is shown in Figure 4. The frame was bolted to the floor and leveled. Due to the manner in which the support frame was constructed, the minimum angle of attack achievable, without penetrating the support frame, was 8.48 degrees between the drill axis and the sheet aluminum.

C. STRAIN MEASUREMENT/RECORDING EQUIPMENT

1. Strain Gages

Linear gages were installed at critical points on the support structure. These gages were Micro-Measurement Division series CEA-06-125UN-350 constantan strain gages with a gage factor of 2.065 +/- 0.5% , and a resistance of
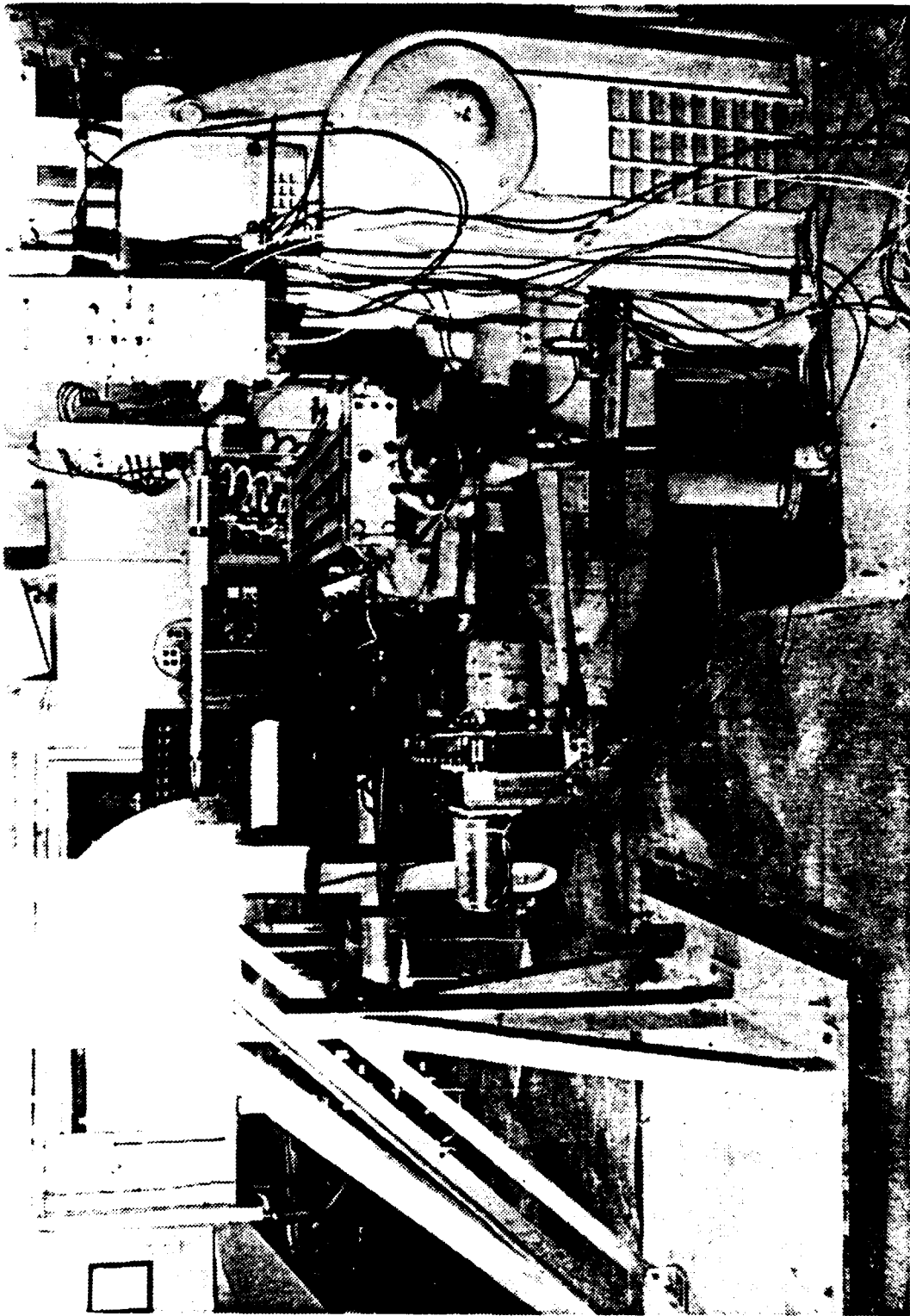
Figure 4. Experimental Equipment Right View

350 ohms +/- 0.3%. A rosettee strain gage was used to determine shear force; it was a Micro-Measurement Division 3 element 45 degree rectangular stacked rosette, series WK-06-120WR-350, superimposed K-alloy, strain gage with a gage factor of 2.065 and a resistance of 350.0 ohms +/- 0.4%.

2. Recording Equipment

Recording of the strain gage outputs was accomplished with an Astro-Med, Inc. 8 channel strip chart recorder via an Ectron amplifier assembly.

III. ANALYTICAL METHOD

A. BACKGROUND

1. System Model

The system model was a rigid body assembly which consisted of a pneumatic drill mounted on a rigid, movable support structure. The support structure was a thin-walled tube (diameter >> thickness) welded to support plates top and bottom and fixed to a rigid milling machine bed.

2. Theoretical Approach

The first step was to conduct a static analysis of the system to determine the force/moment resultants at any arbitrary point on the support tube as a function of the drill tip loading. Following this, a solid mechanic analysis was conducted to determine the particular effect of each force/moment component. Using the theory of superposition, the six effects were added to determine the net effect of the force/moment components. These were then converted to functions of drill tip loading by utilizing the equilibrium equations of the static analysis. The next step was to apply the fundamental triaxial stress-strain relationships. This provided analytical expressions for the strain at any arbitrary point on the tube as a function of the loads at the drill tip. The final step was to evaluate the reverse case; that is, to determine analytical

expressions of the force/moment loads of the drill tip as functions of the strains at an arbitrary point on the tube.

3. Theory of Superposition

The theory of superposition for linear systems states that the net stresses of a system loaded with a combination of forces and moments can be analyzed by determining the resulting stresses of each load and adding the like stress components. Therefore, an analysis of the normal strains and shear strains resulting from the reaction loads of Figure 1 at an arbitrary cut on the tube was analytically evaluated for each load and then combined to determine the net effect.

B. STATIC SOLID MECHANICS ANALYSIS

1. Static Analysis

A free body diagram of the system with static loading is presented in Figure 5. The static equations are:

$$\sum F_x = 0: \quad F_1 + F_{r_x} = 0 \;\rightarrow\; F_{r_x} = -F_1$$

$$\sum F_y = 0: \quad F_2 + F_{r_y} = 0 \;\rightarrow\; F_{r_y} = -F_2$$

$$\sum F_z = 0: \quad F_z + F_{r_y} = 0 \;\rightarrow\; F_{r_z} = -F_3$$

$$\sum \bar{M}_r = \bar{0}: \quad (L_2\hat{j} - L_1\hat{k}) \times (F_1\hat{i} + F_2\hat{j} + F_3\hat{k}) + (M_1 + M_{r_x})\hat{i}$$

$$+ (M_2 + M_{r_y})\hat{j} + (M_3 + M_{r_z})\hat{k} = 0$$

Equating the like components equal to zero yields:

92
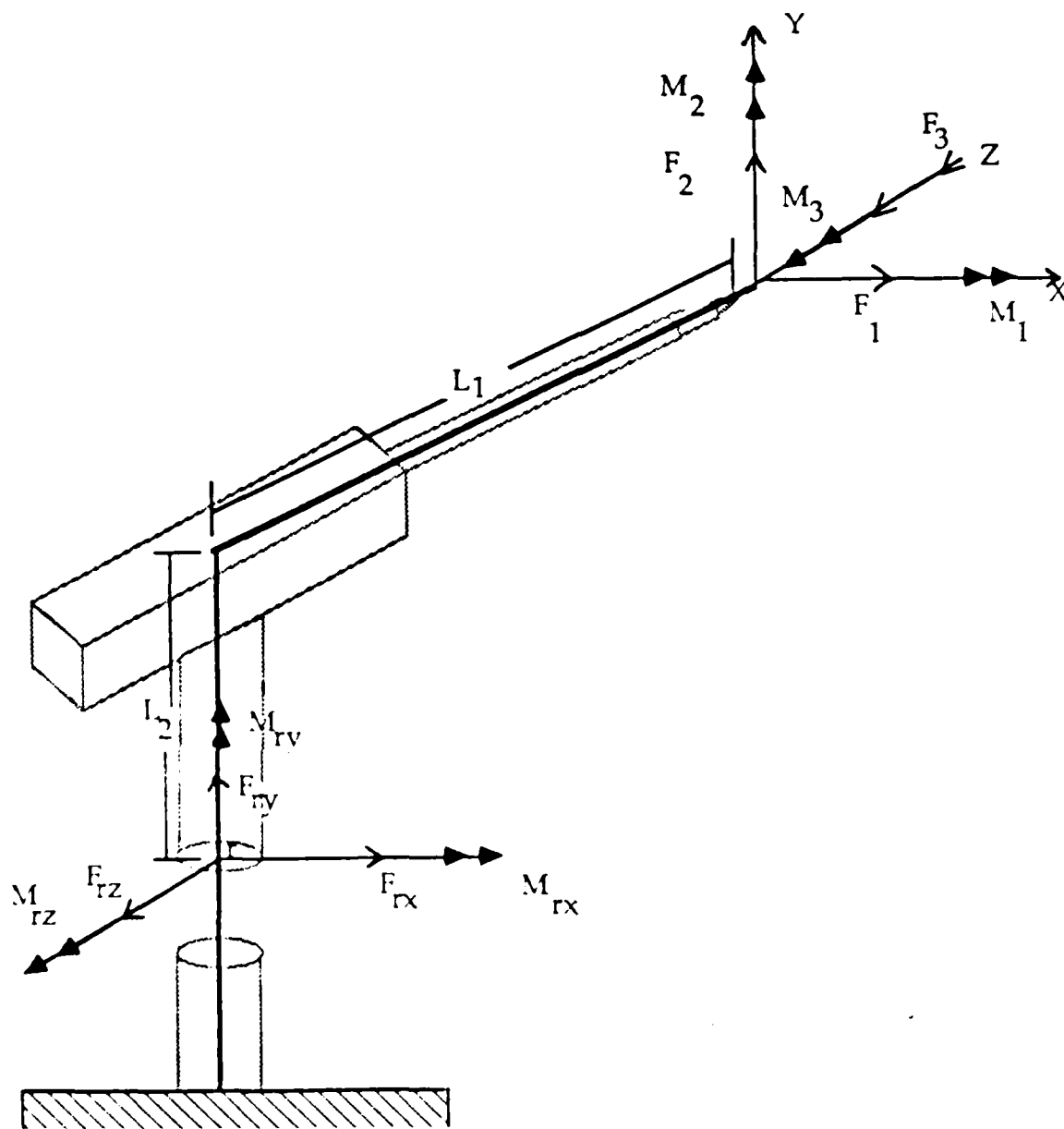
Figure 5.   Penetrator Free Body Diagram

93
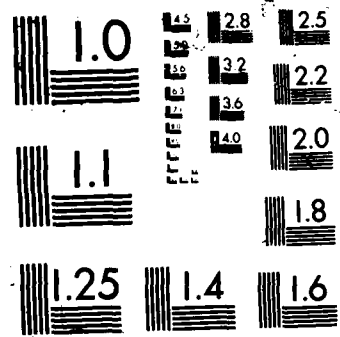
$\hat{i}$ components: $L_2F_3 + L_1F_2 + M_1 + M_{r_x} = 0$

$$\rightarrow M_{r_x} = -(L_2F_3+L_1F_2+M_1)$$

$\hat{j}$ components: $-L_1F_1 + M_2 + M_{r_y} = 0 \rightarrow M_{r_y} = L_1F_1 - M_2$

$\hat{k}$ components: $-L_2F_1 + M_3 + M_{r_z} = 0 \rightarrow M_{r_z} = L_2F_1 - M_3$

2.   <u>Load-Stress Fundamental Relationships [Ref. 3]</u>

For axial tension, the normal stress is given by:

$$\sigma = \frac{P}{A}$$

where:

P = the transmitted force

A = the cross-sectional area $(A = \pi t d)$

For axial bending, the normal stress is given by:

$$\sigma = \frac{Mc}{I}$$

where:

M = the bending moment

c = the distance from the neutral axis to the most extreme fiber $(c = r_o)$

I = the moment of inertia of the cross-section with respect to the neutral axis

$$[I = \frac{\pi}{4}(r_o^4 - r_i^4)]$$

For transverse loading, the shearing stress is given

by:

$$\tau = \frac{VQ}{Jt}$$

where:

        V = the transverse shear force

        Q = the first moment of the area of the semi-circular section with respect to the neutral axis

$$[Q = \frac{2}{3}(r_o{}^3 - r_i{}^3)]$$

        t = the radial thickness of the cross-section

        J = the polar moment of inertia of the cross-section relative to its centroid

$$(J = \frac{\pi}{4} t\bar{d}^3)$$

For torsion of thin-walled tubes, the shearing stress is given by:

$$\tau = \frac{T\bar{r}}{J}$$

where:

        T = the applied torque

        $\bar{r}$ = mean radius

        J = the polar moment of inertia of the cross-section relative to its centroid

$$(J = \frac{\pi}{4} t\bar{d}^3)$$

95

3. Stress Analysis

The state of stress at a point on the tube is described by nine values of stress. The following is an analysis of each reaction load to determine their contribution to these stress values.

For M_{r_z}, Figure 6 depicts the loading condition, with the resulting stress distribution. Notice that the stress at A and C is zero, and at B is maximum. These critical points will be important in all the stress and strain relationships which follow. The stress distribution is given by:

$$\sigma_y(r,\theta) = \frac{M_{r_z} \, r_o \, \cos \theta}{I}$$

For M_{r_x}, Figure 7 depicts the loading condition, with the resulting stress distribution. The stress distribution is given by:

$$\sigma_y(r,\theta) = \frac{M_{r_x} \, r_o \, \sin \theta}{I}$$

For M_{r_y}, Figure 8 depicts the loading condition, with the resulting stress distribution. The stress distribution is given by:

$$\tau = \frac{M_{r_y} \, \bar{r}}{J}$$

96
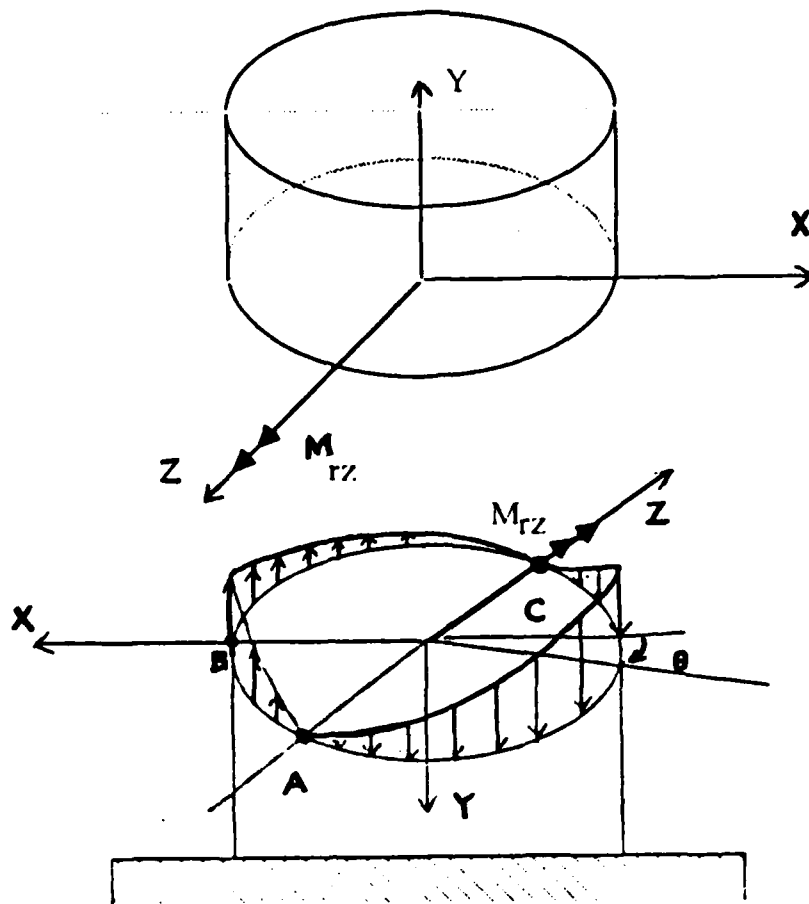
Figure 6. M_{r_z} Load and Stress Distribution

97
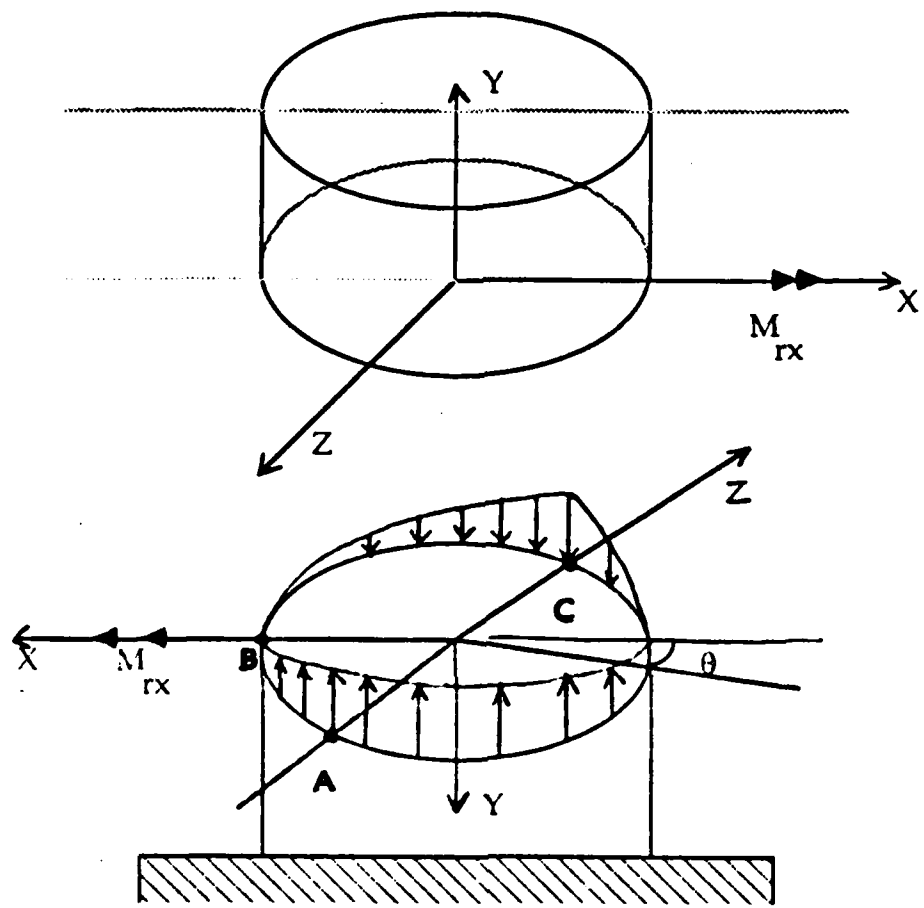
Figure 7. M_{r_x} Load and Stress Distribution
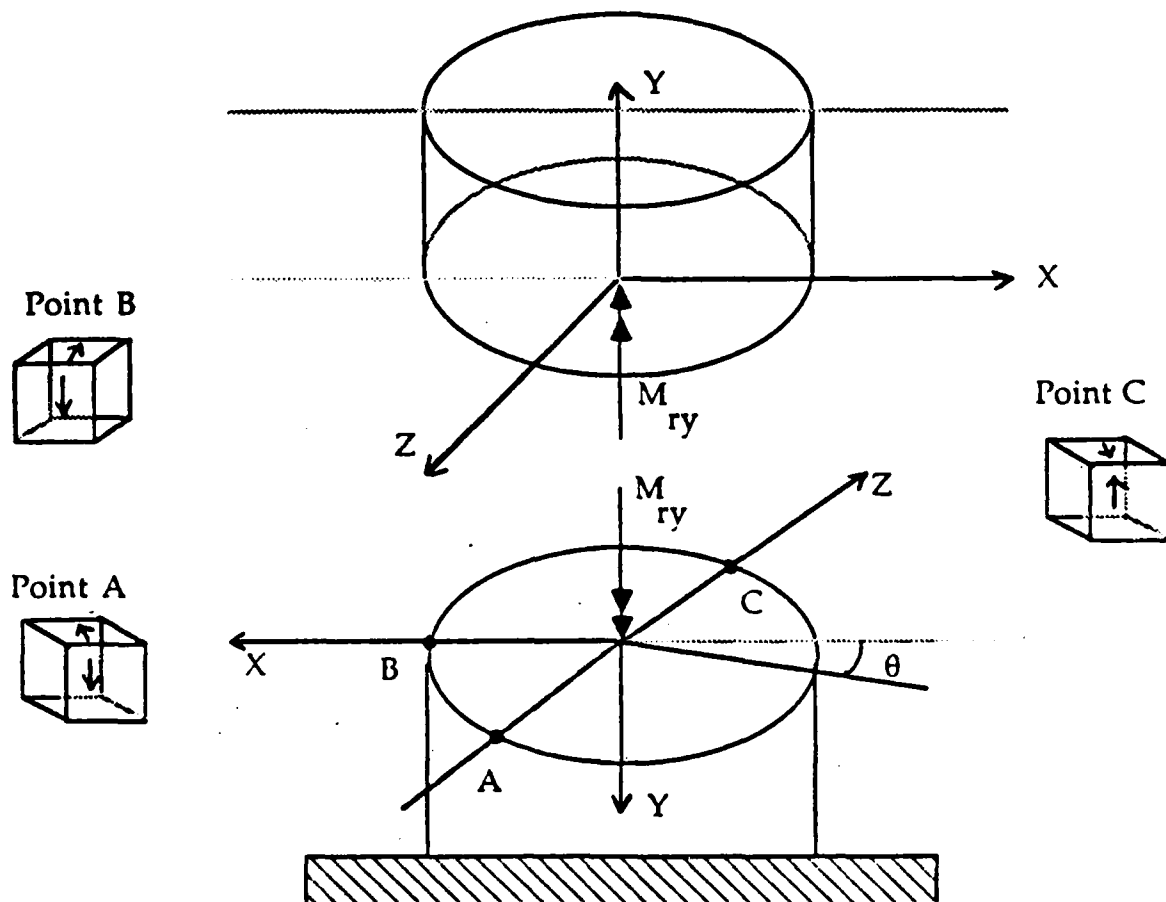
Figure 8. M_{r_y} Load and Stress Distribution

99

For F_{r_z}, Figure 9 depicts the loading condition, with the resulting stress distribution. The stress distribution is given by:

$$\tau = \frac{F_{r_z} Q}{Jt}$$

For F_{r_x}, Figure 10 depicts the loading condition, with the resulting stress distribution. The stress distribution is given by:

$$\tau = \frac{F_{r_x} Q}{Jt}$$

For F_{r_y}, Figure 11 depicts the loading condition, with the resulting stress distribution. The stress distribution is given by:

$$\sigma_y = \frac{F_{r_y}}{A}$$

Now, utilizing the theory of superposition the net stress at points A, B, and C can be determined. Additionally, utilizing the static equilibrium equations of Section II.B.1, the following six stress equations are produced:

Point A:
$$\sigma_{y_A} = \frac{M_{r_x} r_o}{I} - \frac{F_{r_y}}{A} = \frac{-(L_2 F_3 + L_1 F_2 + M_1)}{I} + \frac{F_2}{A}$$

$$\tau_{yx_A} = \frac{-M_{r_y} \overline{r}}{J} - \frac{F_{rx} Q}{Jt} = \frac{-(L_1 F_1 - M_2)\overline{r}}{J} + \frac{F_1 Q}{Jt}$$

100

Figure 9. F_{r_z} Load and Stress Distribution

101
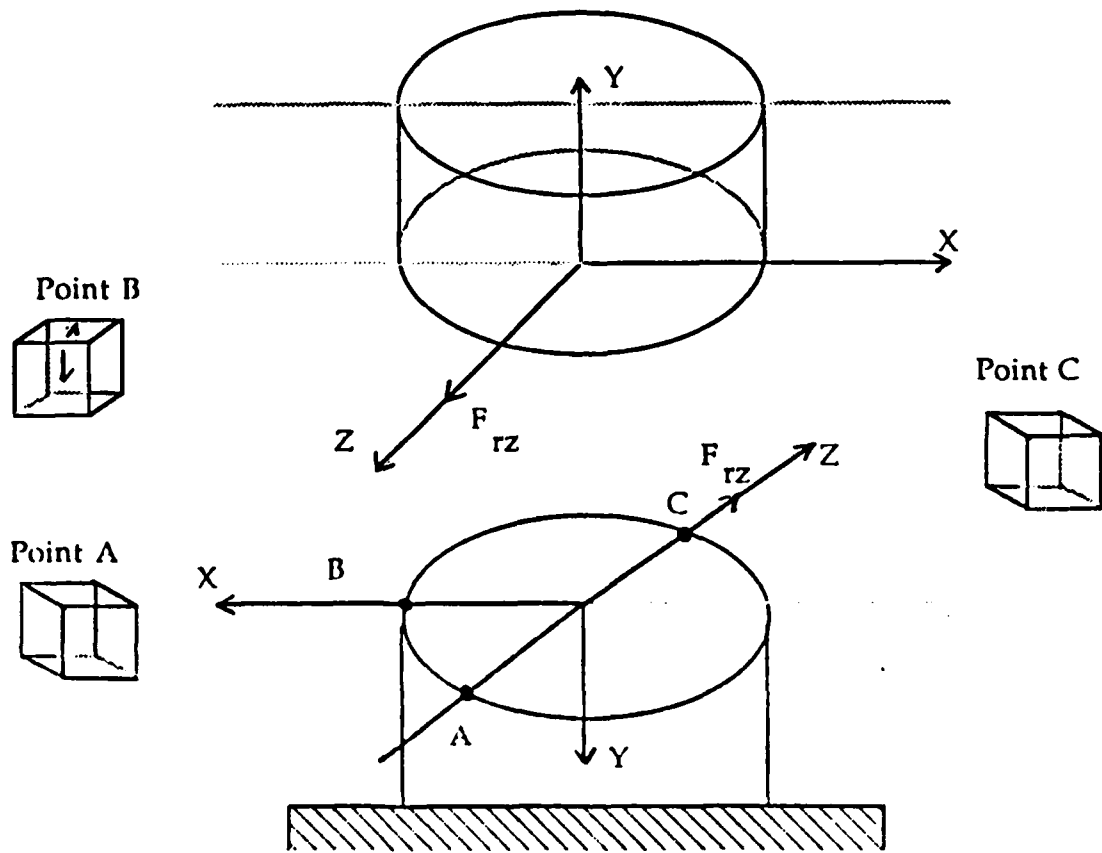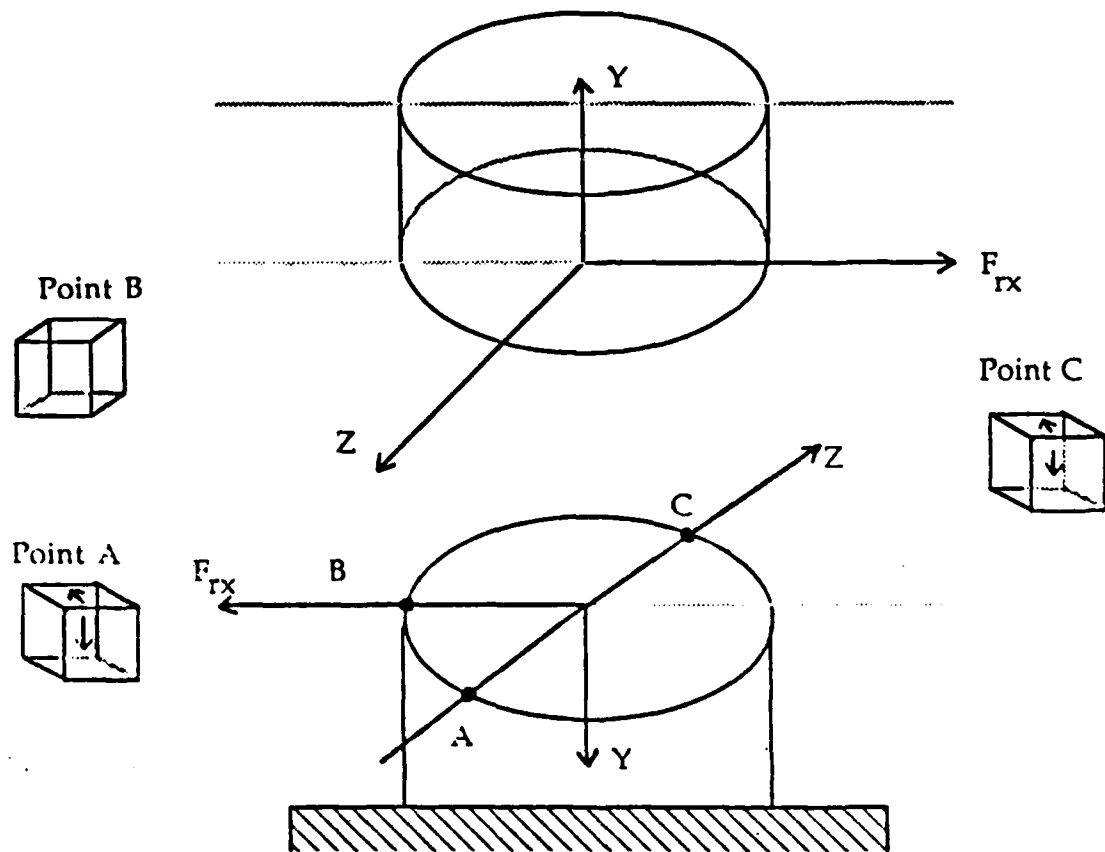
Figure 10. F_{r_x} Load and Stress Distribution
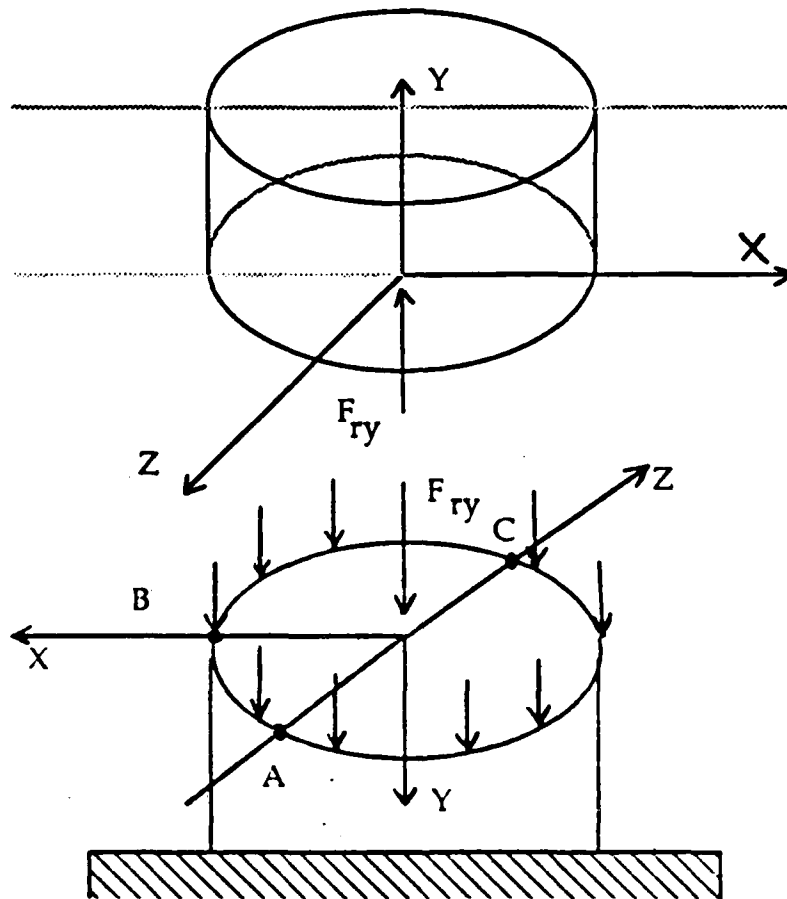
Figure 11. F_{r_y} Load and Stress Distribution

Point B:
$$\sigma_{y_B} = \frac{M_{r_z} r_o}{I} - \frac{F_{r_y}}{A} = \frac{(L_2 F_1 - M_3) r_o}{I} + \frac{F_2}{A}$$

$$\tau_{yz_B} = \frac{-M_{r_y} \bar{r}}{J} - \frac{F_{r_z} Q}{Jt} = \frac{-(L_1 F_1 - M_2)\bar{r}}{J} + \frac{F_3 Q}{Jt}$$

Point C:
$$\sigma_{y_C} = \frac{-M_{r_x} r_o}{I} - \frac{F_{r_y}}{A} = \frac{(L_2 F_3 + L_1 F_2 + M_1) r_o}{I} + \frac{F_2}{A}$$

$$\tau_{yx_C} = \frac{M_{r_y} \bar{r}}{J} - \frac{F_{r_x} Q}{Jt} = \frac{(L_1 F_1 - M_2)\bar{r}}{J} + \frac{F_1 Q}{Jt}$$

4. Stress-strain Fundamental Relationships

$$e_x = \frac{1}{E}[\sigma_x - \nu(\sigma_y + \sigma_z)]$$

$$e_y = \frac{1}{E}[\sigma_y - \nu(\sigma_x + \sigma_z)]$$

$$e_z = \frac{1}{E}[\sigma_z - \nu(\sigma_x + \sigma_y)]$$

$$\gamma_{xy} = \tau_{xy}/G$$

$$\gamma_{yz} = \tau_{yz}/G$$

$$\gamma_{zx} = \tau_{zx}/G$$

5. Determination of Strains

As stated in the theoretical approach, Section II.A.2, the next level of analysis was to determine analytical expressions for the strains at points A, B, and C as functions of the loads. This was accomplished by

104

substituting the expressions for stresses of Section II.B.3 into the fundamental triaxial stress-strain relationships of Section II.B.4. Table I summarizes the results. Appendix A contains the Fortran computer code for these equations.

6. Determination of the Drill Tip Loads

Figure 12 shows the locations of the strain sites of interest. Point A is a point on the outer surface of the tube in the Y-Z plane. L_{2i} is the distance from the centerline of the drill to any arbitrary Z-X plane cut of the tube (e.g., horizontal cut) through point A. The normal strain at point A is a function of L_{2i} only and is given by:

$$\varepsilon_{Y_A}(L_{2i}) = \frac{1}{E}[\frac{-(L_{2i}F_3 + L_1 F_2 + M_1)r_o}{I} + \frac{F_2}{A}]$$

Therefore, taking the difference of two normal strains whose Y coordinates are $L_{2i} = L_{22}$ and $L_{2i} = L_{21}$, such that $L_{22} > L_{21}$, yields

$$\varepsilon_{Y_A}(L_{22}) - \varepsilon_{Y_A}(L_{21}) = \frac{(-L_{22} + L_{21})r_o F_3}{EI}$$

Solving for F_3 yields

$$F_3 = \frac{[\varepsilon_{Y_A}(L_{22}) - \varepsilon_{Y_A}(L_{21})]EI}{(-L_{22} + L_{21})r_o} \tag{1}$$

105

TABLE I

STRAIN EQUATIONS

Point	ϵ_x	ϵ_y	ϵ_z	γ_{yx}	γ_{yz}	γ_{zx}
A	$-\frac{\nu}{E}\left[\frac{(L_2F_3+L_1F_2-M_1)r_o}{I}+\frac{F_2}{A}\right]$	$\frac{1}{E}\left[\frac{-(L_2F_3+L_1F_2+M_1)r_o}{I}+\frac{F_2}{A}\right]$	$-\frac{\nu}{E}\left[\frac{(L_2F_3+L_1F_2+M_1)r_o}{I}+\frac{F_2}{A}\right]$	$\frac{1}{G}\left[\frac{-(L_1F_1-M_2)\bar{r}}{J}-\frac{F_1Q}{JE}\right]$		
B	$-\frac{\nu}{E}\left[\frac{(L_1F_3-M_3)r_o}{I}+\frac{F_3}{A}\right]$	$\frac{1}{E}\left[\frac{(L_1F_3-M_1)r_o}{I}+\frac{F_3}{A}\right]$	$-\frac{\nu}{E}\left[\frac{(L_2F_3-M_1)r_o}{I}+\frac{F_3}{A}\right]$		$\frac{1}{G}\left[\frac{-(L_1F_1-M_2)\bar{r}}{J}+\frac{F_3Q}{JE}\right]$	
C	$-\frac{\nu}{E}\left[\frac{(L_2F_3+L_1F_2-M_1)r_o}{I}+\frac{F_2}{A}\right]$	$\frac{1}{E}\left[\frac{(L_2F_3+L_1F_2+M_1)r_o}{I}+\frac{F_2}{A}\right]$	$-\frac{\nu}{E}\left[\frac{(L_2F_3-L_1F_2+M_1)r_o}{I}+\frac{F_2}{A}\right]$	$\frac{1}{G}\left[\frac{-(L_1F_1-M_2)}{J}+\frac{F_1Q}{JE}\right]$		

a. Side View (Y-Z plane)

b. Front View (X-Y plane)

Figure 12.   Strain Measurement Locations

Alternatively, using the same rationale for point B and taking the difference of two normal strains with coordinates $Y = L_{22}$ and $Y = L_{21}$, yields

$$\varepsilon_{Y_B}(L_{22}) - \varepsilon_{Y_B}(L_{21}) = \frac{(L_{22}-L_{21})\, r_o\, F_1}{EI}$$

Solving for F_1 yields

$$F_1 = \frac{[\varepsilon_{Y_B}(L_{22}) - \varepsilon_{Y_B}(L_{21})]\,EI}{(L_{22}-L_{21})\, r_o} \qquad (2)$$

At points A and C, the M_r bending moment normal stress components are equal but in opposite directions. Therefore adding the normal strains at these points yields

$$\varepsilon_{Y_A}(L_{21}) + \varepsilon_{Y_C}(L_{22}) = \frac{2F_2}{EA}$$

Solving for F_2 yields

$$F_2 = \frac{[\varepsilon_{Y_A}(L_{21}) + \varepsilon_{Y_C}(L_{21})]\,EA}{2} \qquad (3)$$

With the three load forces known, the moment loads can be determined directly from the strain equations. Solving the normal strain at point A at L_{21} for M_1 yields

$$M_1 = \frac{I}{r_o}[-E\varepsilon_{Y_A}(L_{21}) + \frac{F_2}{A} - \frac{(L_{21}F_3 + L_1F_2)r_o}{I}] \qquad (4)$$

108

Solving the normal strain at point B at L_{21} for M_3 yields

$$M_3 = \frac{I}{r_o}[-E\varepsilon_{Y_B}(L_{21}) + \frac{F_2}{A} + \frac{L_{21}F_1 r_o}{I}]$$ (5)

Solving the shear stress at point B at L_{21} for M_2 yields

$$M_2 = \frac{J}{r}[G\gamma_{yz_B}(L_{21}) - \frac{F_3 Q}{Jt} + \frac{L_1 F_1 \bar{r}}{J}]$$ (6)

7. Previous Load Determinations

As stated earlier, the previous work assumed the principal loads were F_1, F_3, and M_3 and the other loads were negligible. The further assumption that F_1 did not contribute to the bending moment about the Z axis was also made. Thus the strain equations of Table I reduce to:

$$\varepsilon_{Y_A}(L_{21}) = \frac{-L_{21} F_3 r_o}{EI}$$

$$\varepsilon_{Y_B}(L_{21}) = \frac{-M_3 r_o}{EI}$$

$$\gamma_{Y_{Z_B}}(L_{21}) = \frac{1}{G}[\frac{-L_1 F_1 \bar{r}}{J} + \frac{F_3 Q}{Jt}]$$

Solving for the loads yields

$$F_3 = \frac{-EI}{L_{21}r_o}\varepsilon_{Y_A}(L_{21})$$ (7)

$$M_3 = \frac{-EJ}{r_o}\varepsilon_{Y_B}(L_{21})$$ (8)

109

$$L_1 F_1 = -\frac{J}{r}[G\gamma_{yz_B}(_{21}) - \frac{F_3 Q}{Jt}] \tag{9}$$

In a later part of this report, the results of equations (1), (5), (6) and equations (7), (8), (9) will be compared in order to evaluate their predictions.

C. STRAIN GAGE PLACEMENT

1. Strain Gage Type and Location

In order to solve equations (1), (2), and (3) the axial strain at five locations is required. Additionally, the shear strain is required at one location for equation (6). Table II summarizes the strain gage types and locations, and Figure 12 shows their locations.

2. Determination of the Shear Stress

Although the normal strains can be measured directly from the gages, additional computations are required to determine the shear stress.

Figure 13 depicts a 45 degree rectangular rosette strain gage. The applicable strain equation is [Ref. 3]:

$$\gamma_{yz} = 2\varepsilon_{yz} - \varepsilon_z - \varepsilon_y$$

Substituting this expression into the expression for M_2 yields

$$M_2 = \frac{J}{r}[G[2\varepsilon_{yz_B}(L_{21}) - \varepsilon_{z_B}(L_{21}) - \varepsilon_{y_B}(L_{21})] - \frac{F_3 Q}{Jt} + \frac{L_1 F_1 \bar{r}}{J}]$$

110

TABLE II

STRAIN GAGE TYPES AND LOCATIONS

Point	Moment Arm	Type	Quantity Measured
A1	L_{21}	Linear	ε_y
A2	L_{22}	Linear	ε_y
B1	L_{21}	45 degree rectangular rosette	$\varepsilon_z, \varepsilon_y, \varepsilon_{yz}$
B2	L_{22}	Linear	ε_y
C1	L_{21}	Linear	ε_y
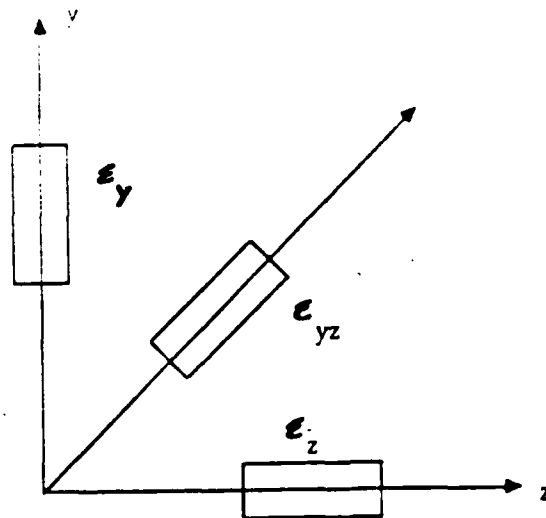
Figure 13. 45 Degree Rectangular Rosette

111

Table III summarizes the force/moments equations for this work and Table IV for the previous study. Appendix B contains the Fortran computer code for these equations.

D. CALIBRATION PROCEDURES

1. Approach

Static loads were applied to the support structure to evaluate whether the analytical expressions of Table I correctly predict the measured strains at locations A, B, and C. Figures 14, 15, 16, and 17 depict the methods by which the static loads were applied to the instrumented drill support structure. The static loads consisted of round stock cut into approximately ten pound segments. Each segment weight was measured using an Instron Corporation Material Testing System 100 pound test cell. For this test cell the accuracy of the measurement was +/- 1.0 % of the indicated load, or 0.02 % of the test cell capacity (100 lbs).

The weight holding apparatus depicted in the static loading figures was of sufficient strength to hold the required testing loads. However, due to misalignment in the support structure, the loads were not applied exactly along the desired coordinate directions associated with the

TABLE III

LOAD EQUATIONS

$$F_1 = \frac{[\epsilon_{y_B}(L_{22}) - \epsilon_{y_B}(L_{21})]EI}{(L_{22} - L_{21})r_o}$$

$$F_2 = \frac{[\epsilon_{y_A}(L_{21}) - \epsilon_{y_C}(L_{21})]EA}{2}$$

$$F_3 = \frac{[\epsilon_{y_A}(L_{22}) - \epsilon_{y_A}(L_{21})]EI}{(-L_{22} + L_{21})r_o}$$

$$M_1 = \frac{I}{r_o}[-E\epsilon_{y_A}(L_{21}) + \frac{F_2}{A} - \frac{(L_{21}F_3 + L_1F_2)r_o}{I}]$$

$$M_2 = \frac{J}{r}(G[2\epsilon_{yz_B}(L_{21}) - \epsilon_{z_B}(L_{21}) - \epsilon_{y_B}(L_{21})] - \frac{F_3Q}{Jt} + \frac{L_1F_1\bar{r}}{J})$$

$$M_3 = \frac{I}{r_o}[-E\epsilon_{y_B}(L_{21}) + \frac{F_2}{A} + \frac{L_{21}F_1r_o}{I}]$$

TABLE IV

LOAD EQUATIONS OF PREVIOUS WORK

$$F_3 = \frac{-EI}{r_o L_{21}}\epsilon_{y_{A_{21}}}$$

$$M_3 = -\frac{EI}{r_o}M_3$$

$$L_1F_1 = -\frac{\bar{r}}{J}(G[2\epsilon_{yz_B}(L_{21}) - \epsilon_{z_B}(L_{21}) - \epsilon_{y_B}(L_{21})] - \frac{F_3Q}{Jt})$$

113
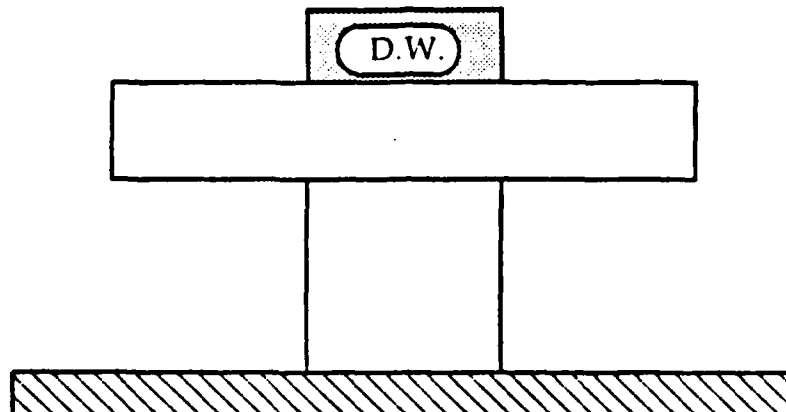
Figure 14. F_2 Static Loading
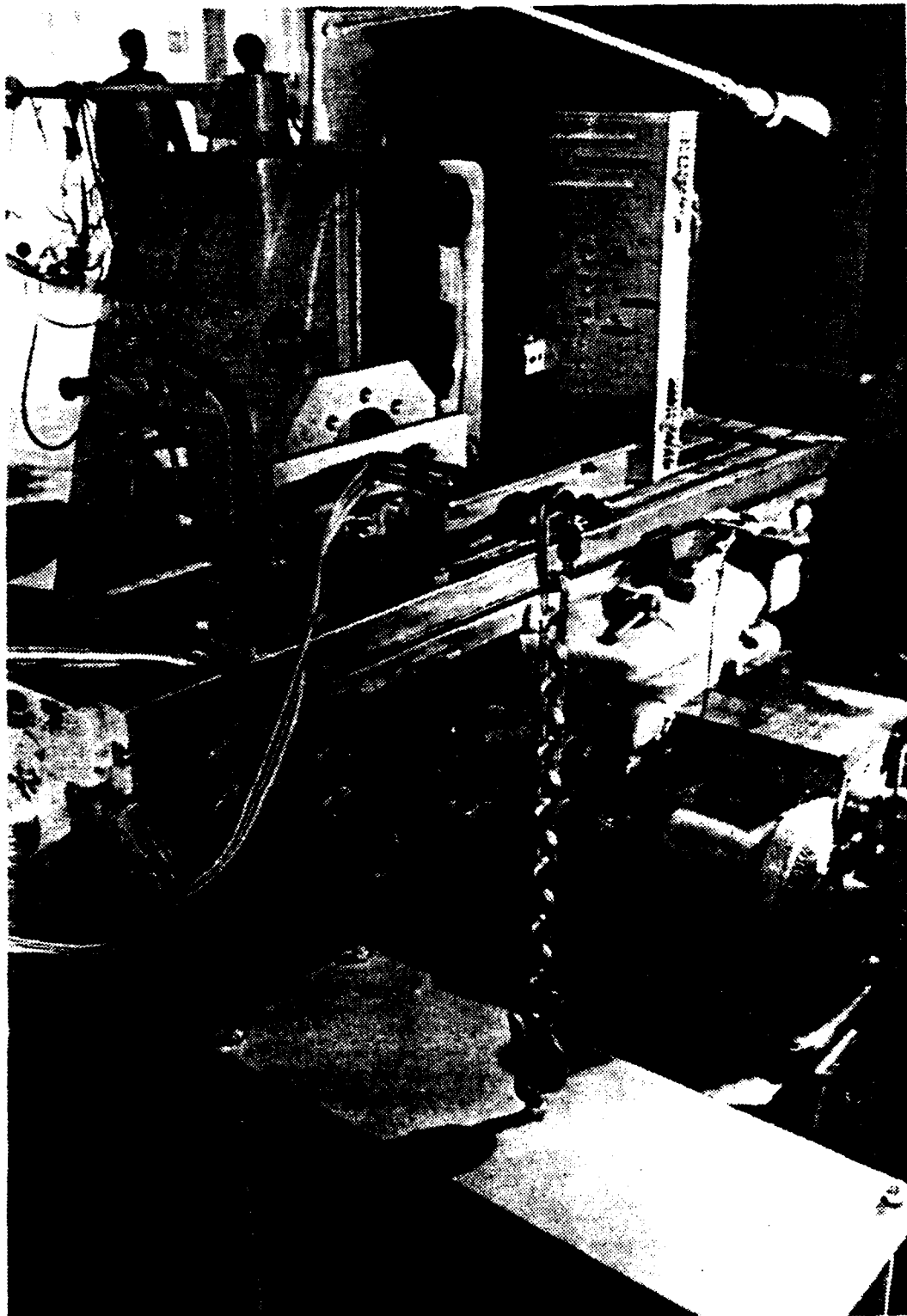
Figure 15. F_1 Static Loading

115

Figure 16. F_3 Static Loading

116
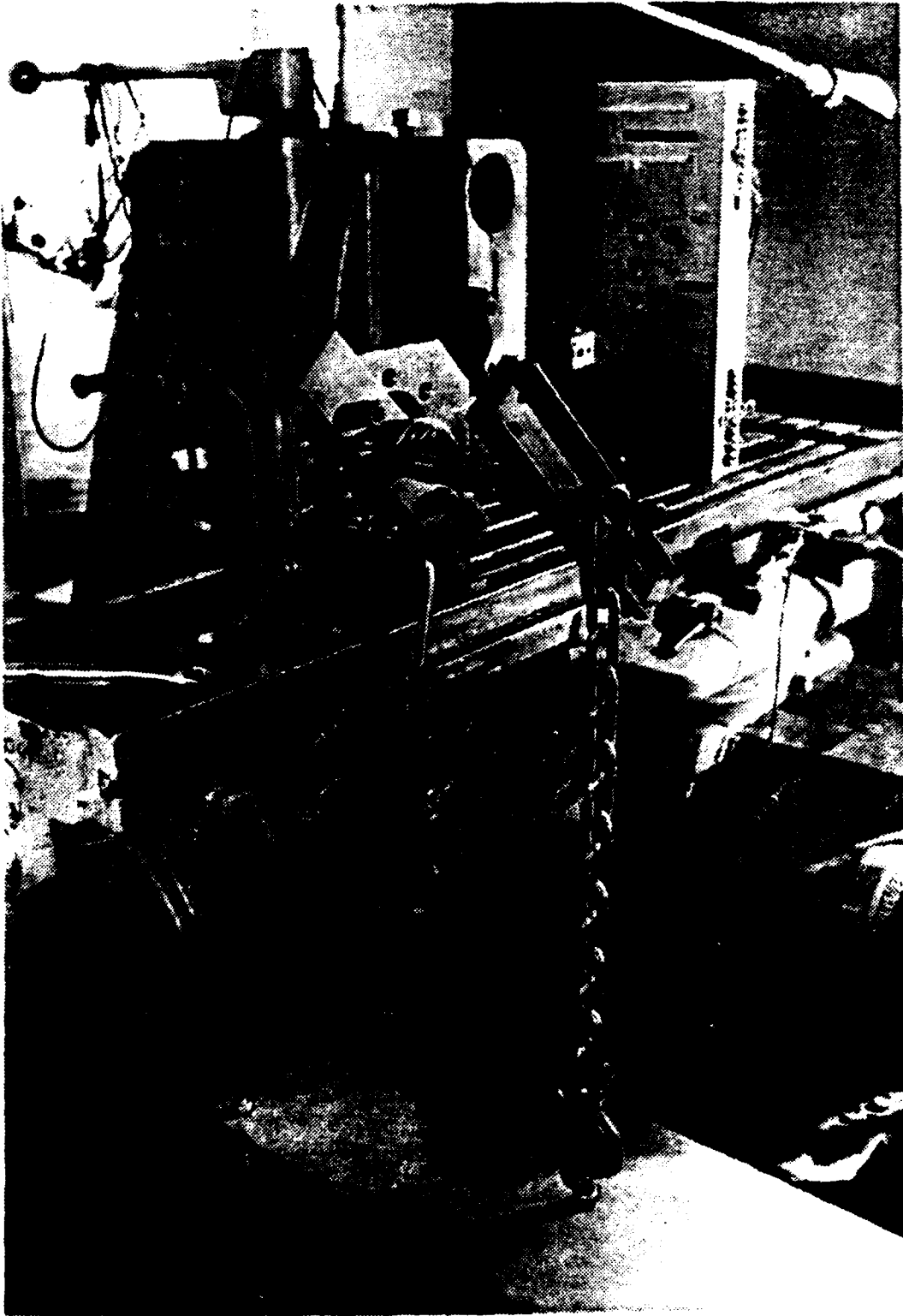
Figure 17. F_1 and F_3 Static Loading

117

support structure. Figure 18 illustrates the problem encountered when a load was attempted along the Z-axis. To overcome this obstacle, an angle position indicator was used to measure the angles between the orthonormal axes and the line of action of the static loads. Only two of the three angles were measurable and the following relationship was used to determine the third angle:

$$1 = \sqrt{\cos^2\alpha + \cos^2\beta + \cos^2\delta}$$

The component of the static load acting on each of the orthonormal axes was then determined using the following relationships:

$$F_1 = F \cos \alpha$$

$$F_2 = F \cos \beta$$

$$F_3 = F \cos \delta$$

As can be seen from Table III, each of the forces is equal to a strain quantity times a constant, i.e,

$$F_1 = [\varepsilon_{Y_B}(L_{22}) - \varepsilon_{Y_B}(L_{21})]*constant$$

$$F_2 = [\varepsilon_{Y_A}(L_{21}) + \varepsilon_{Y_C}(L_{21})]*constant$$

$$F_3 = [\varepsilon_{Y_A}(L_{22}) - \varepsilon_{Y_A}(L_{21})]*constant$$

118
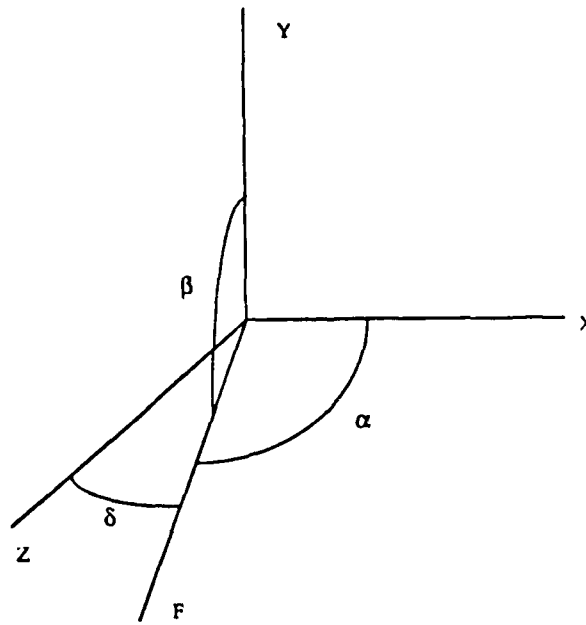
Figure 18. Static Force Line of Action

Therefore, in comparing the measured versus calculated values, these strain quantities were used to determine the accuracy of the analytical strain equations.

2. Static Loading Results

Figure 19 shows the plot of $[\varepsilon_{y_B}(L_{22}) - \varepsilon_{y_B}(L_{21})]$, both measured and calculated, versus an applied F_1 static load of 30.74 to 99.65 pounds. As can be seen from the figure, there is a negligible difference between the measured and calculated values. Figures 20 and 21 show the plots of the F_2 and F_3 component forces with their respective strain quantities. The substantial difference shown in the later figures will be discussed below.

119
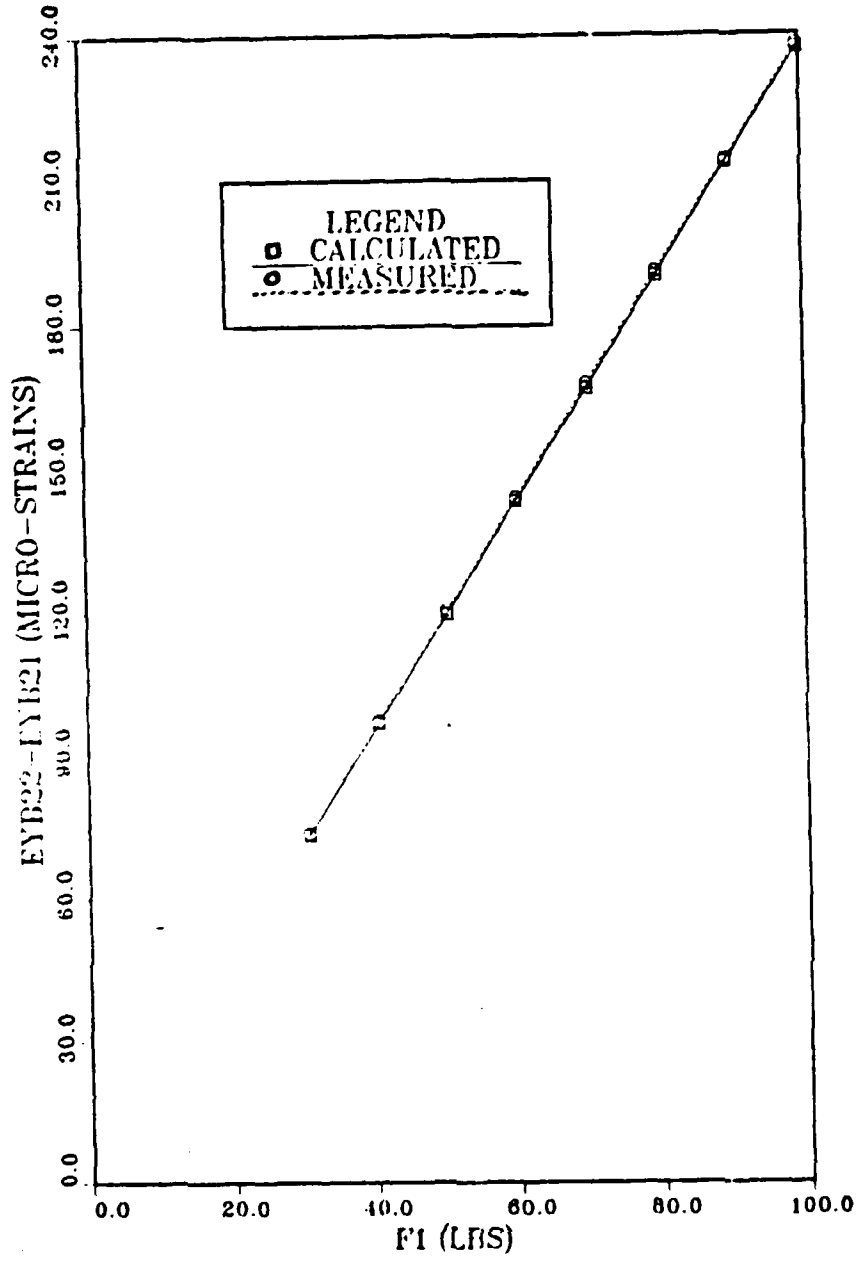
F1 STATIC TEST

Figure 19. F$_1$ Load, F$_1$ Plot

120
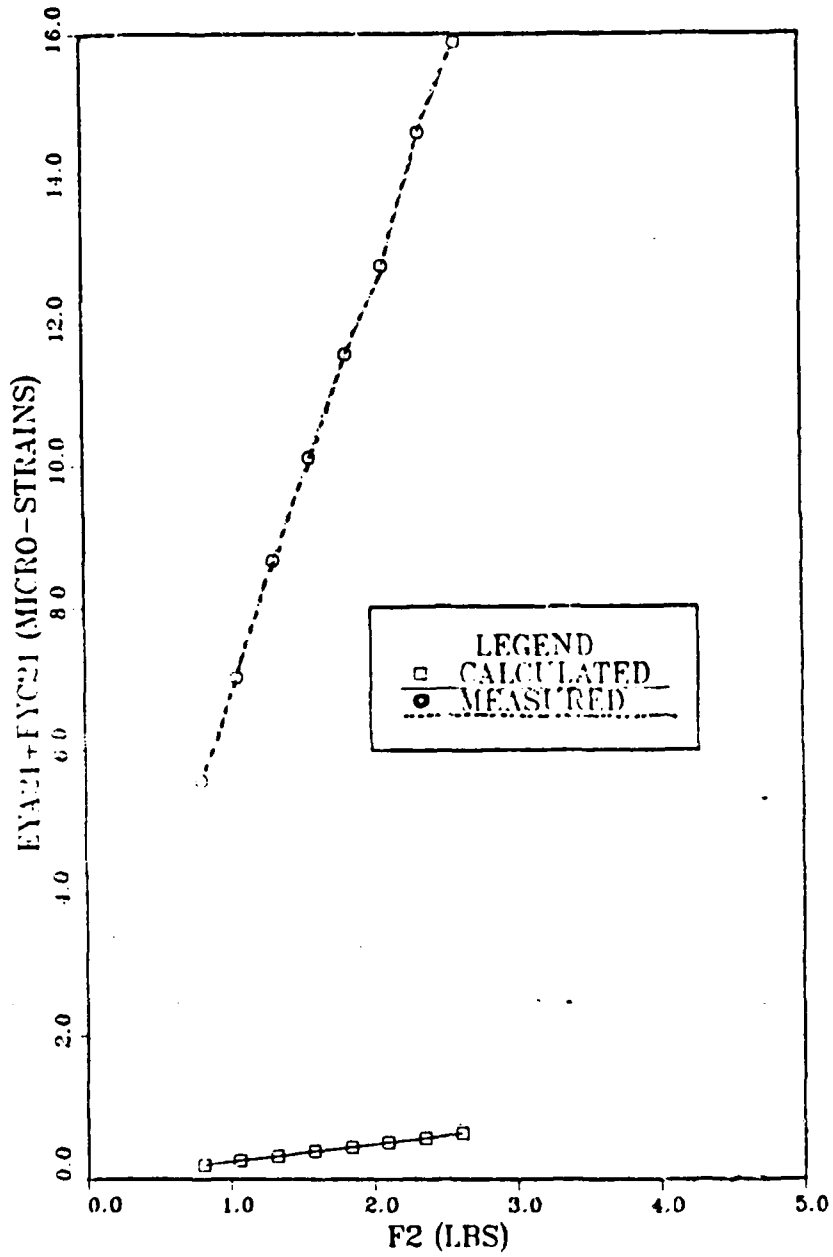
F1 STATIC TEST

Figure 20. F_1 Load, F_2 Plot

F1 STATIC TEST
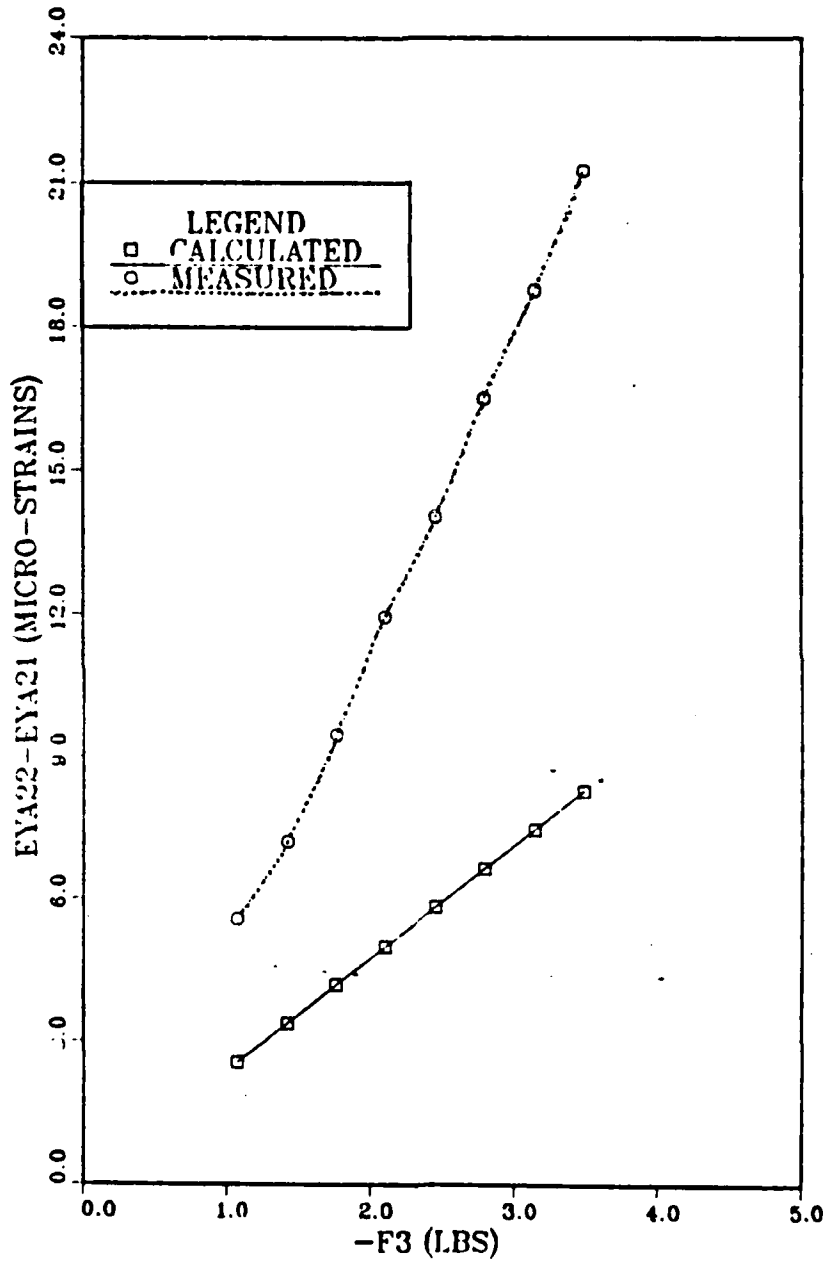
Figure 21. F_1 Load, F_3 Plot

122

Figure 22 shows the measured versus calculated strain plot for an F_3 load of from 30.77 to 198.66 pounds. Again the measured and calculated values of the principal strain quantity correlate well. Figures 23 and 24, for the transverse force components, exhibit the same disporportion- ate errors as was found with the F_1 static load.

Figures 25 and 26 show the plots for major X and Z axis loading. This loading was accomplished by placing the support fixture at an angle of 44.5 degrees with respect to the load line of action. Therefore, a static load of 30.77 to 198.66 pounds produced F_1 and F_3 loads of 22.83 to 147.42 pounds and 20.61 to 133.06 pounds respectively. Again the strain equations produced results very close to the measured values with the exception of the transverse F_2 force, as shown in Figure 27.

The results of applying an F_2 static load are shown in Figure 28. F_2 loading was accomplished by placing weights of 10.0 to 100.02 pounds directly on top of the support fixture. In this test, there were considerable differences in the measured and calculated values.

3. Sources of Error

The errors encountered with the transverse force components and F_2 loading are attributed to the nonsymmet- ric shape of the tube, the nonrigidity of the tube, and the nonhomogeneous tube material. These factors all contribute to change the centroidal axis location.

F3 STATIC TEST
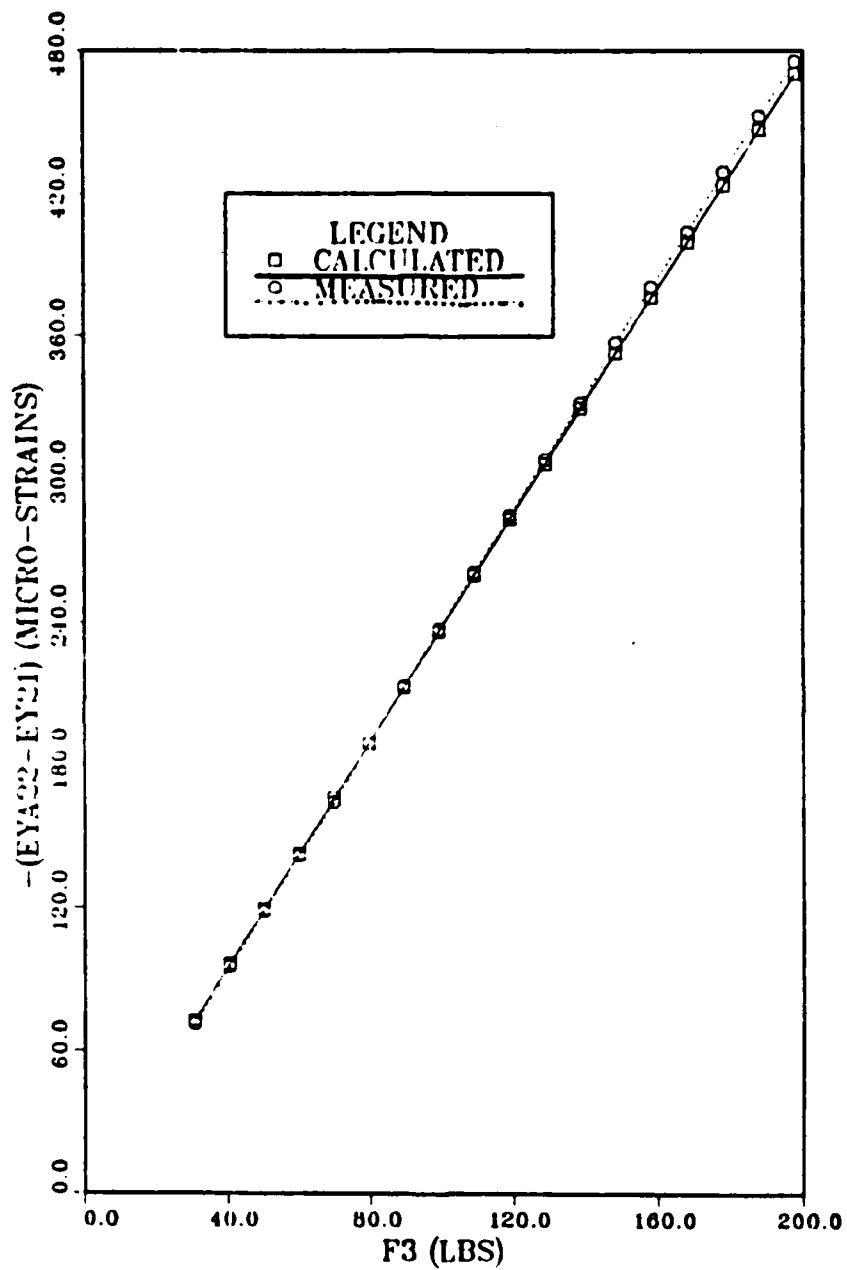
Figure 22. F_3 Load, F_3 Plot

124
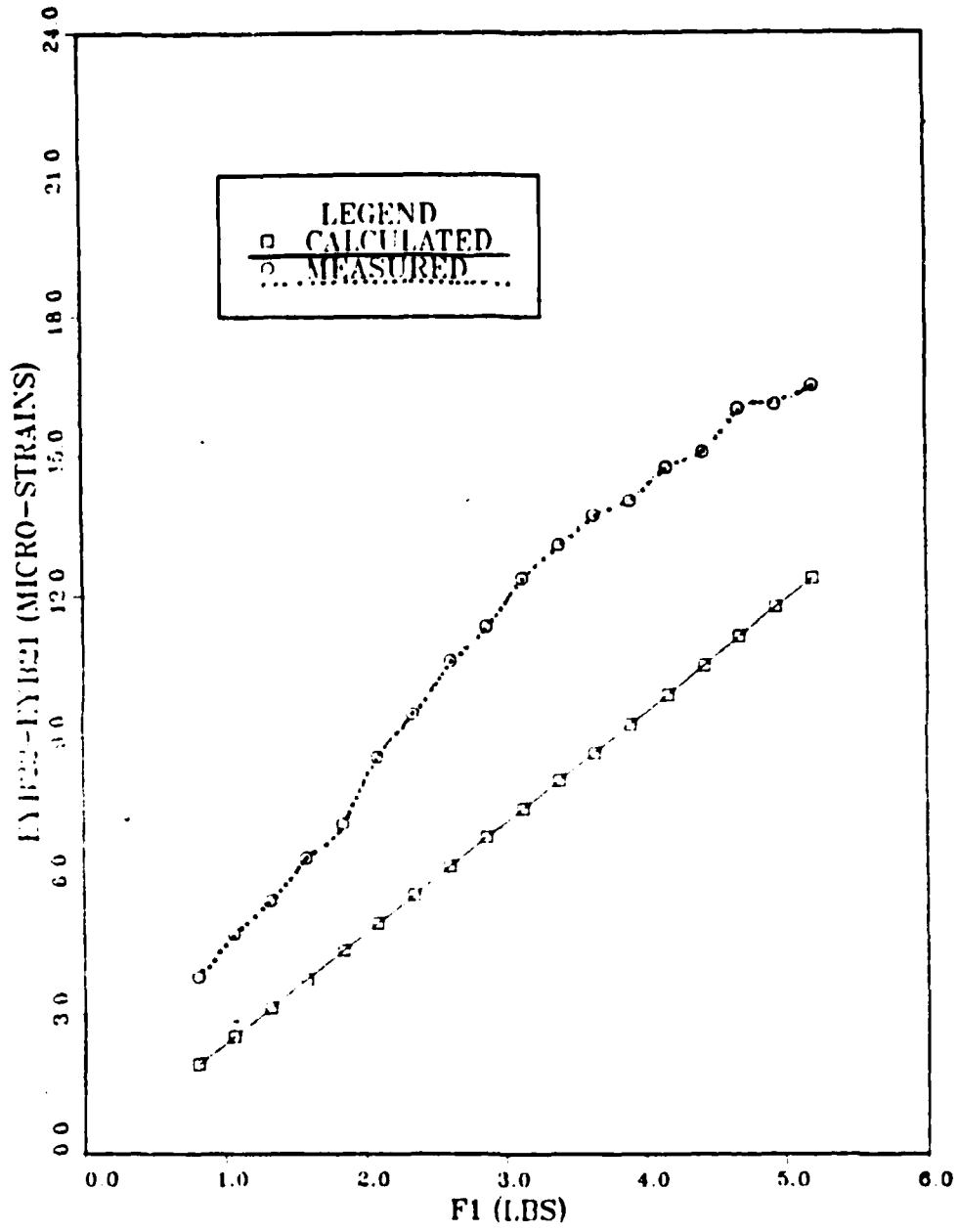
F3 STATIC TEST

Figure 23. F_3 Load, F_1 Plot

125
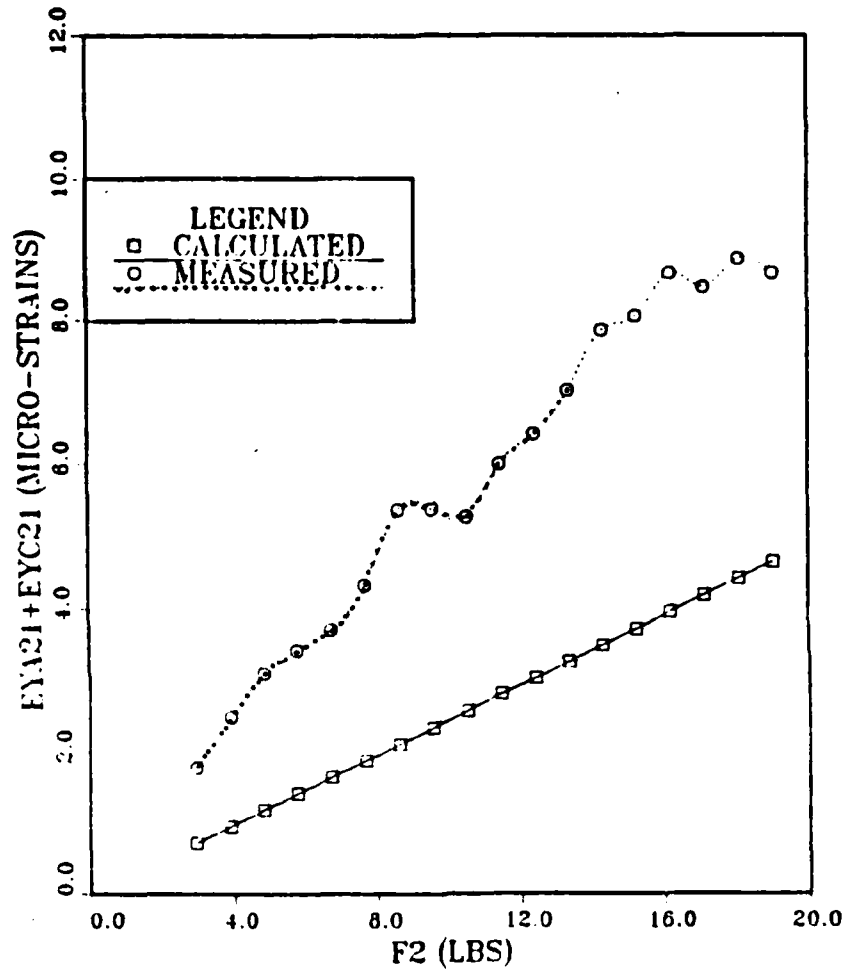
F3 STATIC TEST

Figure 24. F_3 Load, F_2 Plot

126

F1 AND F3 STATIC TEST
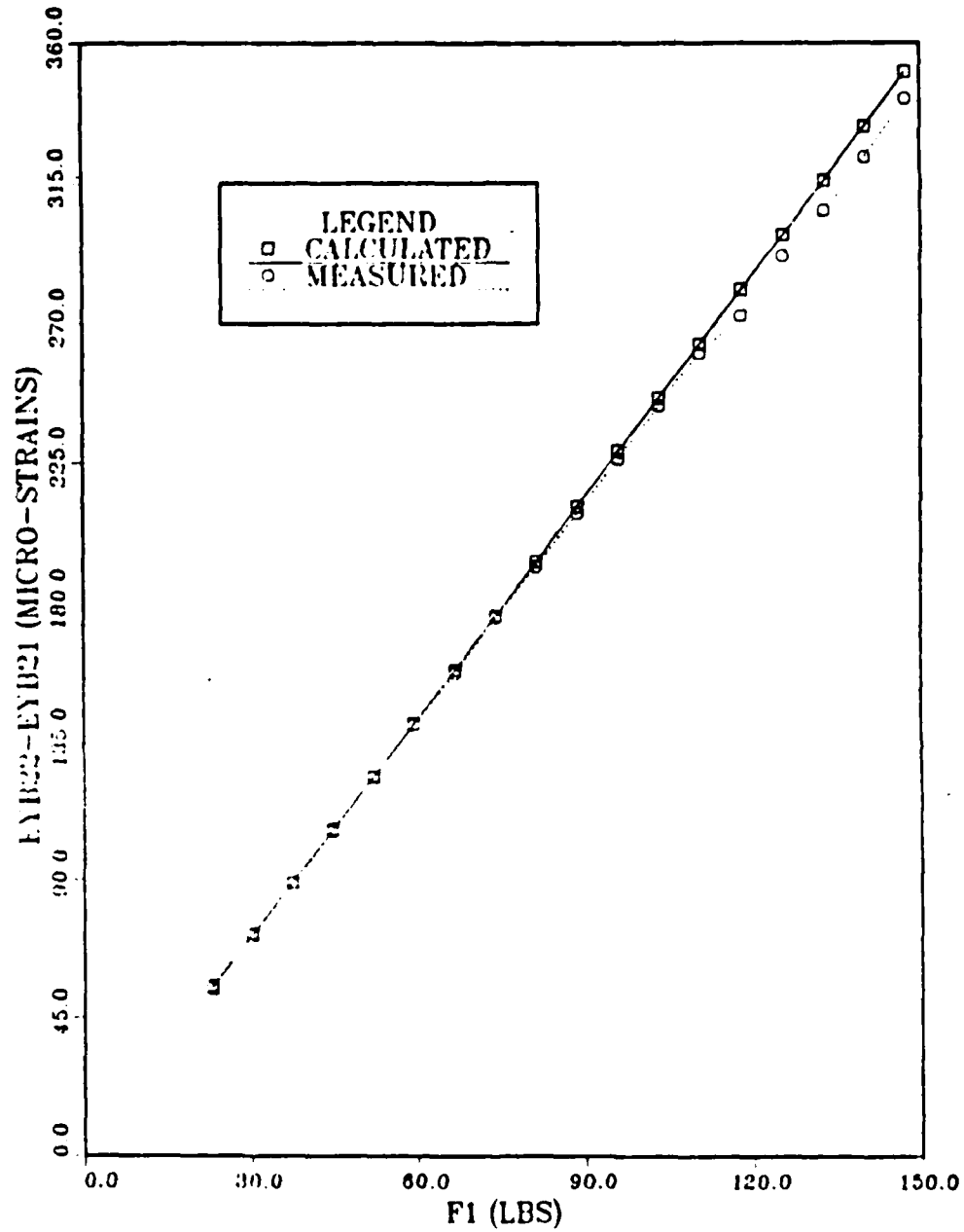
Figure 25. F_1 and F_3 Loads, F_1 Plot

F1 AND F3 STATIC TEST
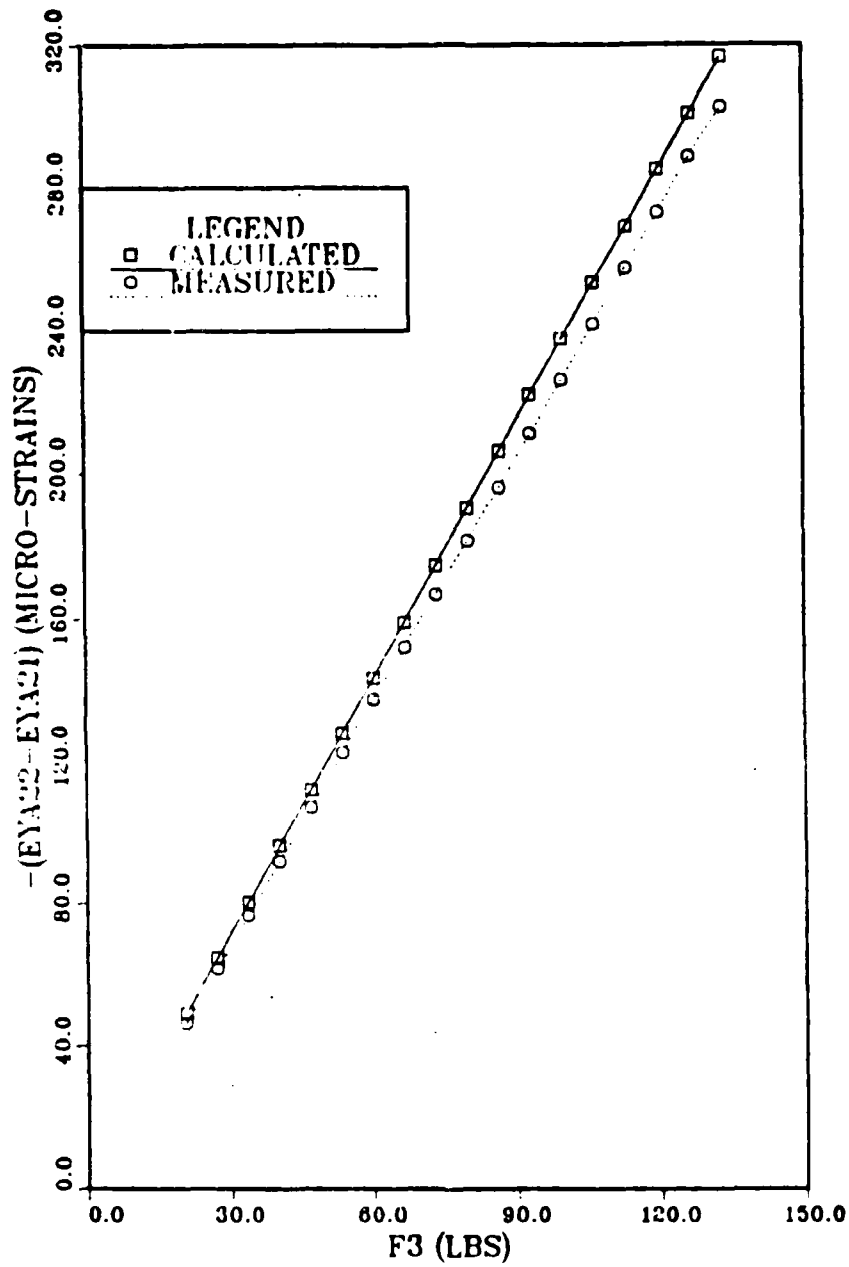
Figure 26.   F$_1$ and F$_3$ Loads, F$_3$ Plot

128

F1 AND F3 STATIC TEST
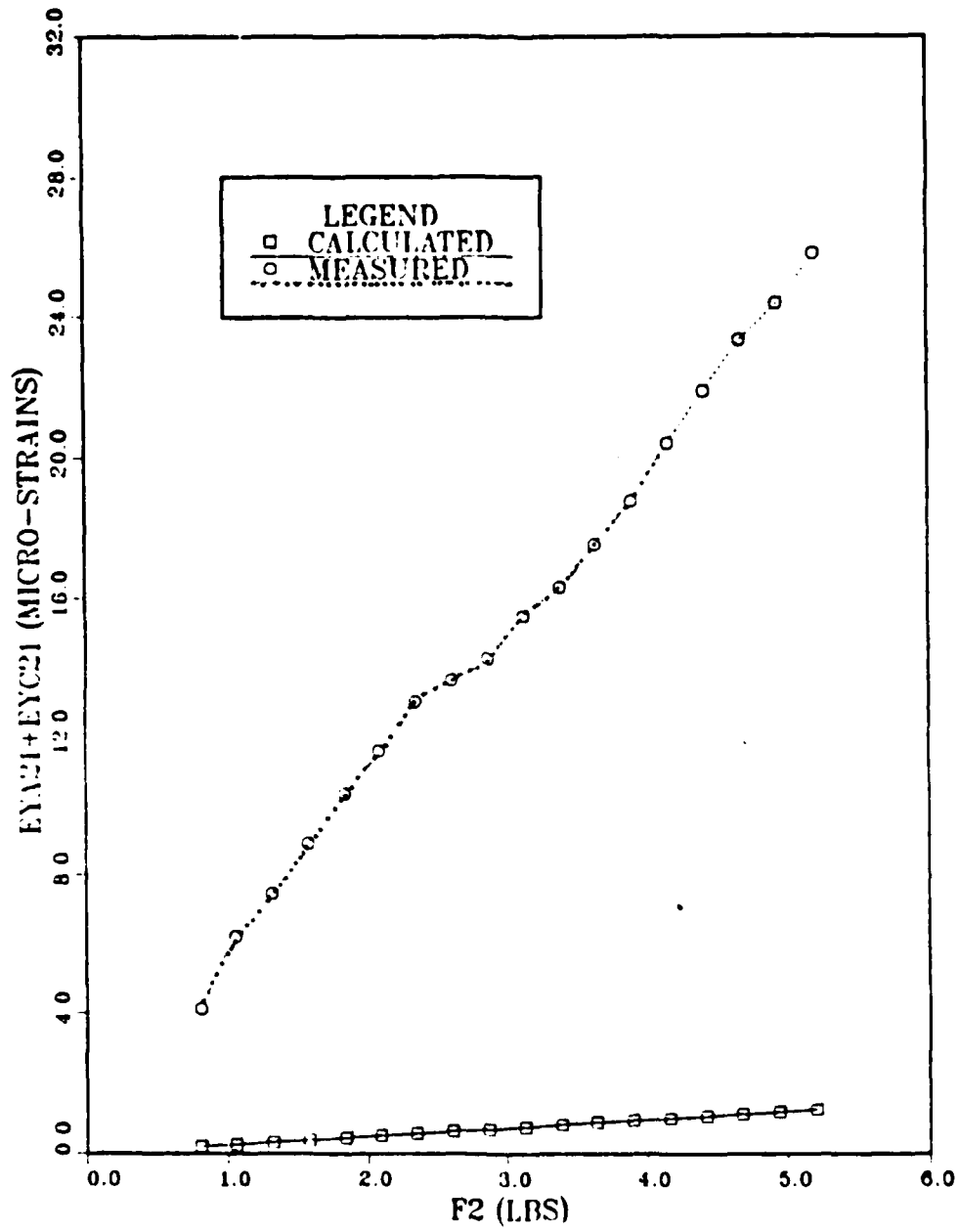
Figure 27. F_1 and F_3 Loads, F_2 Plot

129

F2 STATIC TEST
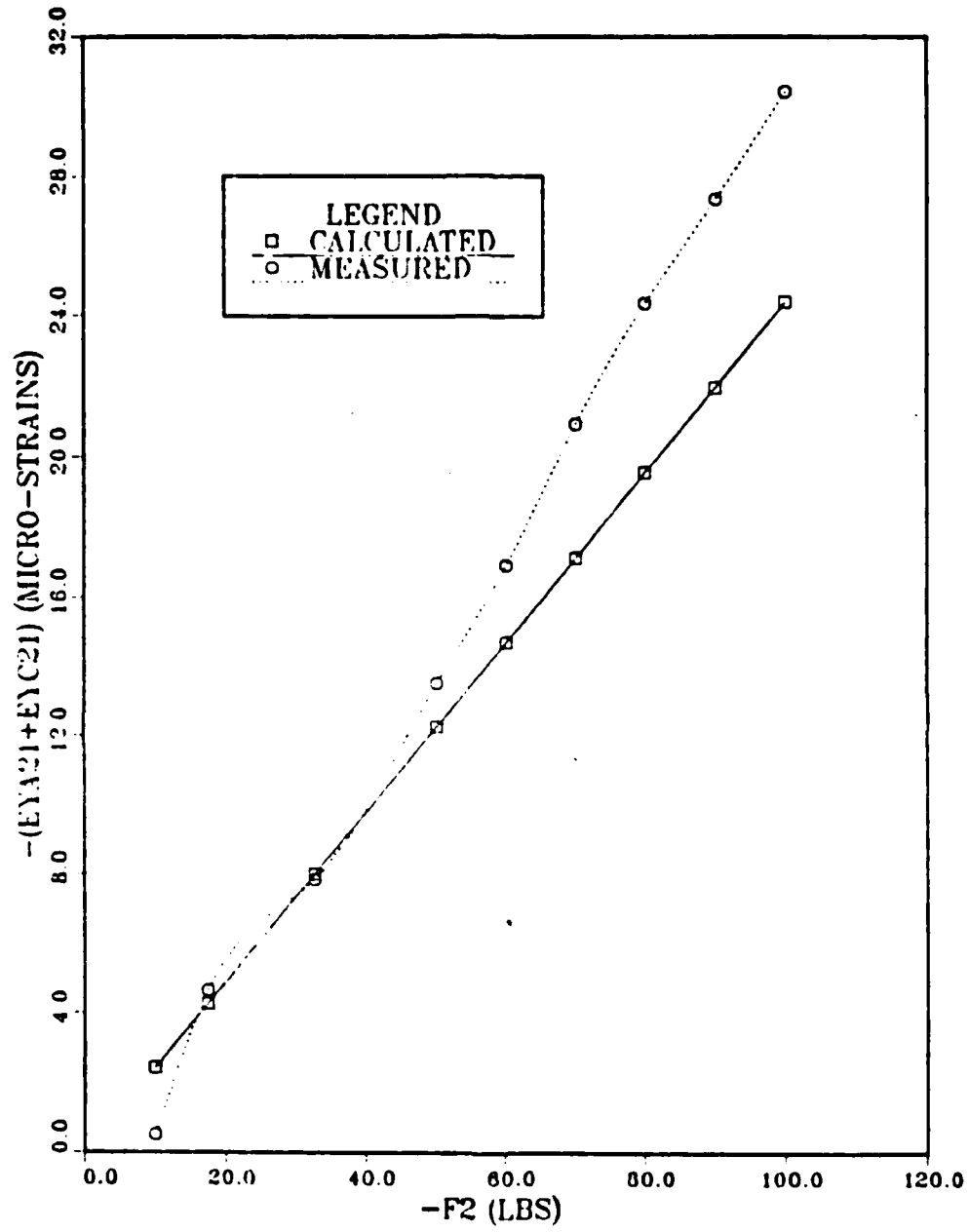
Figure 28. F_2 Load, F_2 Plot

As can be seen in Figures 6 and 7 the location of the neutral axis for the bending moments coincides with the centroidal axis. Also, the magnitude of the stress is directly proportional to the distance from the neutral axis, and the stress distribution is symmetrical about it. These facts operate with the non-ideal, real tube discussed above to create a changing location of the centroidal axis and, consequently distort the stress distribution. As shown in the transverse force component plots, the change in centroidal axis has a substantial impact on the stress distribution and, consequently, the reliability of the strain equations to determine the loading. But due to the relative magnitudes shown in the preceding figures, these errors were considered negligible in predicting the dynamic loads during a drilling operation.

Similarly, the stress distribution resulting from an F_2 loading, Figure 11, was nonuniform with a change in the centroidal axis location, yet agreement was good.

IV. DRILLING OPERATION AND RESULTS

A. EXPERIMENTAL PROCEDURES

The strain gage amplifier assembly and strip chart recorder were energized and given a one hour warm-up period prior to commencement of recording data. The air compressor was started one-half-hour prior to the drilling operations to allow sufficient time to pressurize the accumlator to 167 psig. After the one hour warm-up period, the amplifiers were calibrated to 4.84 volts per 10,000 micro-strains. The penetrator trigger was taped in the full open position and air flow was controlled by an in-line valve. The penetrator was positioned via the milling machine's two motors to permit the penetrator an angle of attack of 8.48 degrees and a three diameter separation between drill hole centers.

At the commencement of a drilling operation, the in-line air valve was fully opened and the Z-axis motor of the milling machine energized to a bed speed of 14 inches per minute. All systems were stopped after the penetrator's drill had completed drilling the hole.

The strip chart recordings were then converted to micro-strains. A sample of the strip chart readings is shown in Figure 29. Since the conclusions of this work are to be used in the design of the penetrator support structure, a worst-case set of data was needed. Therefore,

132
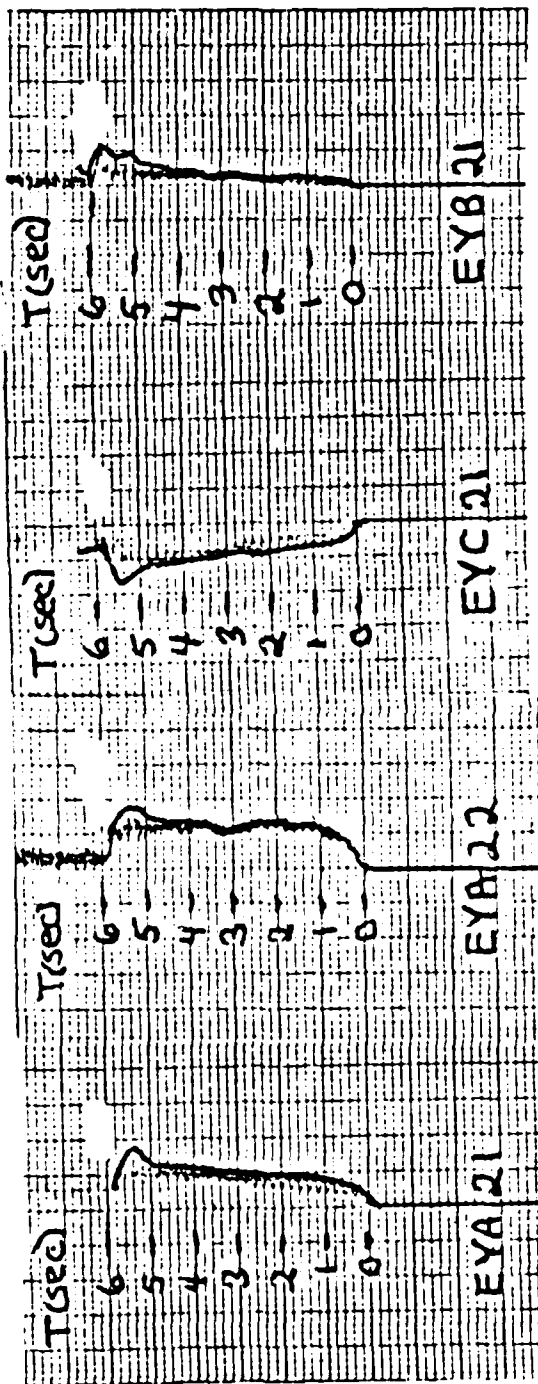
Figure 29. Sample of Strip Chart Recording

133

a french curve was used to curve-fit the maximum values of the recorded strains. To accurately reflect the continous time effects of the drilling, data at every 0.2 seconds was used. The micro-strain data was then entered into the static analysis Fortran program of Appendix B, which is the computer code equivalent of the force/moment equations of Table III and Table IV.

B. AIR SUPPLY PRESSURE

To obtain viable data, it was essential that the penetrator successfully complete the hole drilling without binding. The previous work used an operating pressure for the penetrator of 100 psig [Ref. 2]. In the present work, a pressure regulator was initially installed in the air line to reduce the accumulator pressure from 167 to 100 psig. With 100 psig supply pressure, the penetrator was unsuccessful in completing a drilling operation without binding. The supply pressure was increased in steps of 25 psig from 100 to 150 psig and no run was achieved without experiencing binding. Therefore the pressure regulator was removed from the system and runs were achieved without binding with pressures of 158 and 164 psig.

As drillings were accomplished, the accumulator supply pressure decreased from 167 to 150 psig, at which point the compressor would recharge the accumalators. During the experimental process it was noted that any attempts to drill with supply pressures of less than 158 psig binding occured.

134

C. DRILLING DATA RESULTS

Three drilling operations were conducted with supply pressures of 158, 164, and 164 psig. For the plots, the drillings are differentiated by their duration times as illustrated in Table V.

TABLE V

LOAD RESULTS DESIGNATION

Run No.	Pressure (PSIG)	Duration Time (sec)	Functions
1	158	6.0	$F_1(6.0), F_2(6.0), F_3(6.0),$ $M_1(6.0), M_2(6.0), M_3(6.0)$
2	164	7.2	$F_1(7.2), F_2(7.2), F_3(7.2)$ $M_1(7.2), M_2(7.2), M_3(7.2)$
3	164	10.0	$F_1(10.0), F_2(10.0), F_3(10.0),$ $M_1(7.2), M_2(7.2), M_3(7.2)$

1. Forces

The force loads consist of a thrust component, F_3, acting along the axis of the drill and two transverse components, F_1 and F_2, acting in a plane perpendicular to the axis of the drill.

As can be seen on Figure 30, the force F_3 was always in the positive direction, i.e., pushing against the drill. The graphs indicate the values of F_3 are fairly consistent no matter what the drilling time was. For instance, the maximum values were 89.34, 88.47, and 98.01 pounds for the

135

three runs. Also, the data shows that F_3 increases to a peak as the drill penetrates, then drops in magnitude prior to increasing to a final maximum peak. The data relates to the geometry of the drill tip (Figure 31) as the drill penetrates. The first peak is caused by the knuckle, the second by the trailing edge.

The transverse forces on the other hand, vary in direction from one run to the next (Figures 32, 33). The direction change is attributed to the movement of the drill tip prior to stablizing in a drilling configuration; i.e., seating into the test panel. If the initial biting movement of the drill tip is referred to as "walking," then the direction and distance of the walking contribute to both the magnitude and direction of the transverse loads. Once a stable configuration was achieved in a run the force direction for that individual run did not change. In run 1, the direction of the drill was down and to the left on the surface of the test panel. While for run 2, the direction was up and to the left; for run 3, the direction was down and to the right. The maximum values were for F_1: -24.28, -13.66, and 44.67 pounds; and for F_2: -50.76, 42.35, and -42.31 pounds. The maximum values for F_1 occured at the end of the drill run and for F_2 at the beginning of the run. Therefore, F_2 was the governing transverse force in determining the stablized configuration. The F_1 force was

# F3: Z AXIS FORCE
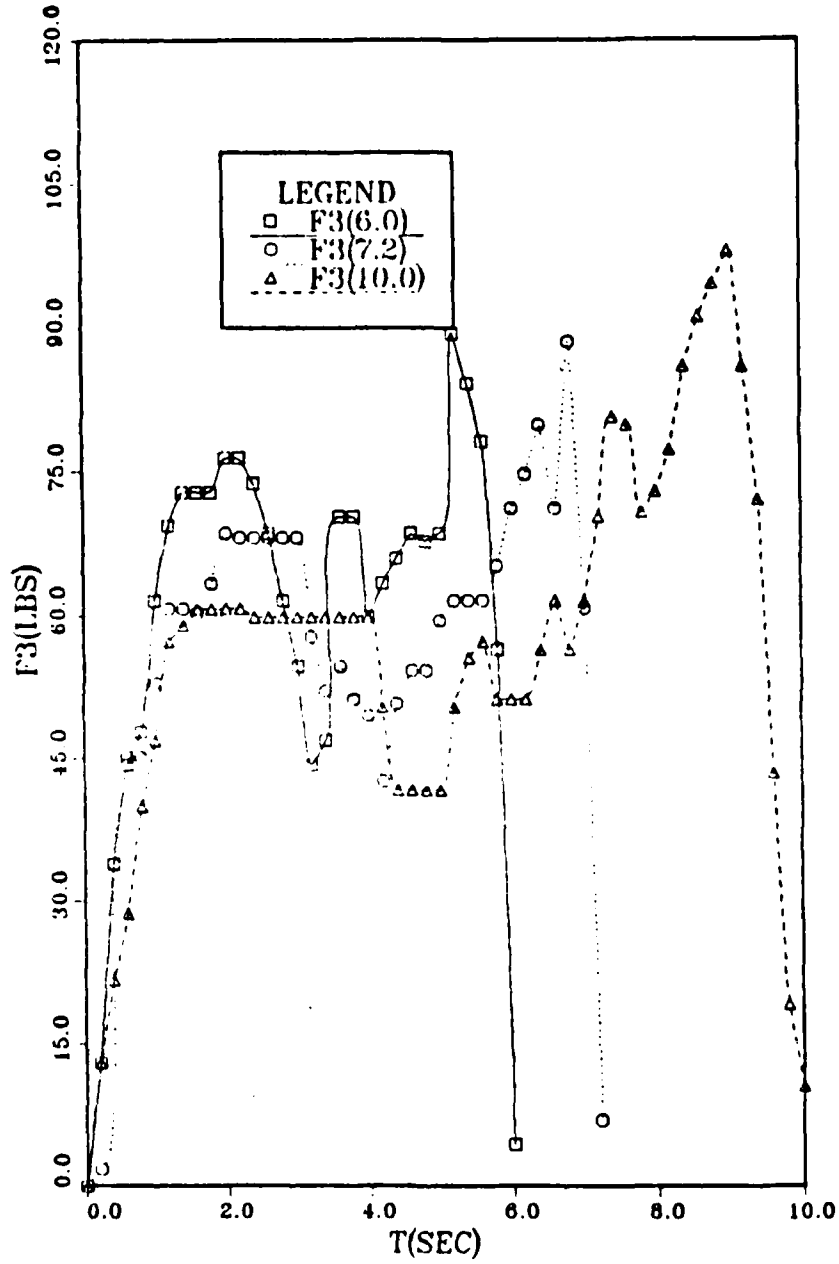
Figure 30. Drilling Results for F_3 Plot
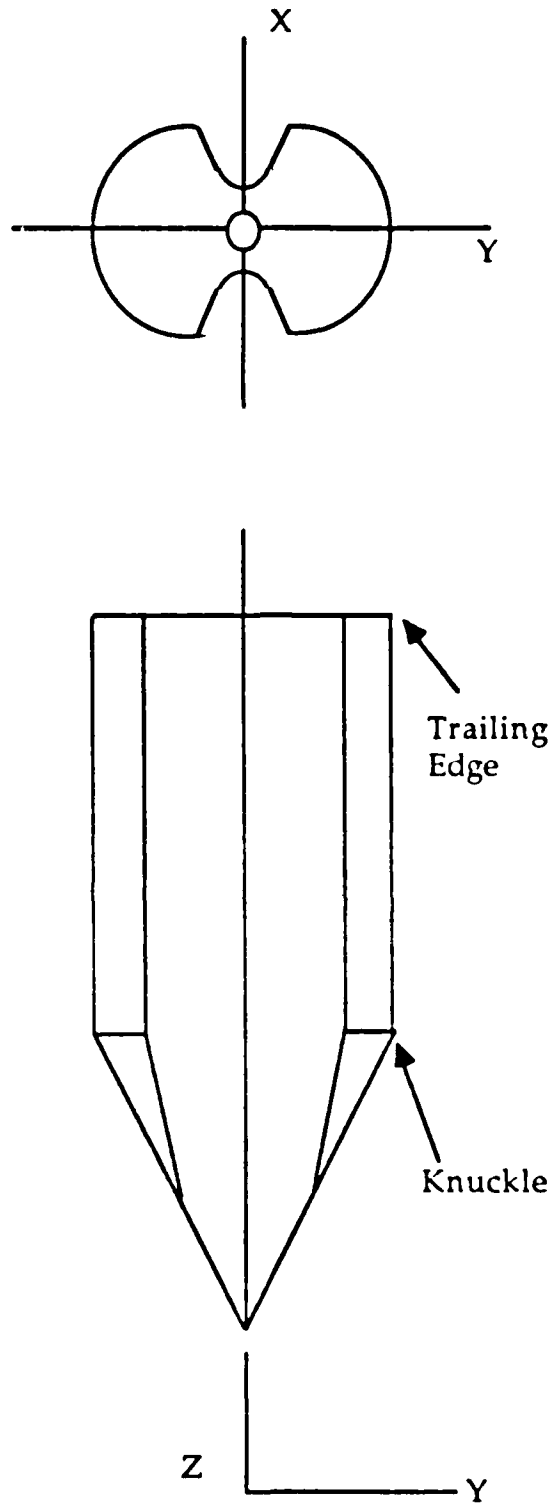
Figure 31.   Drill Bit Schematic

F1: X AXIS FORCE
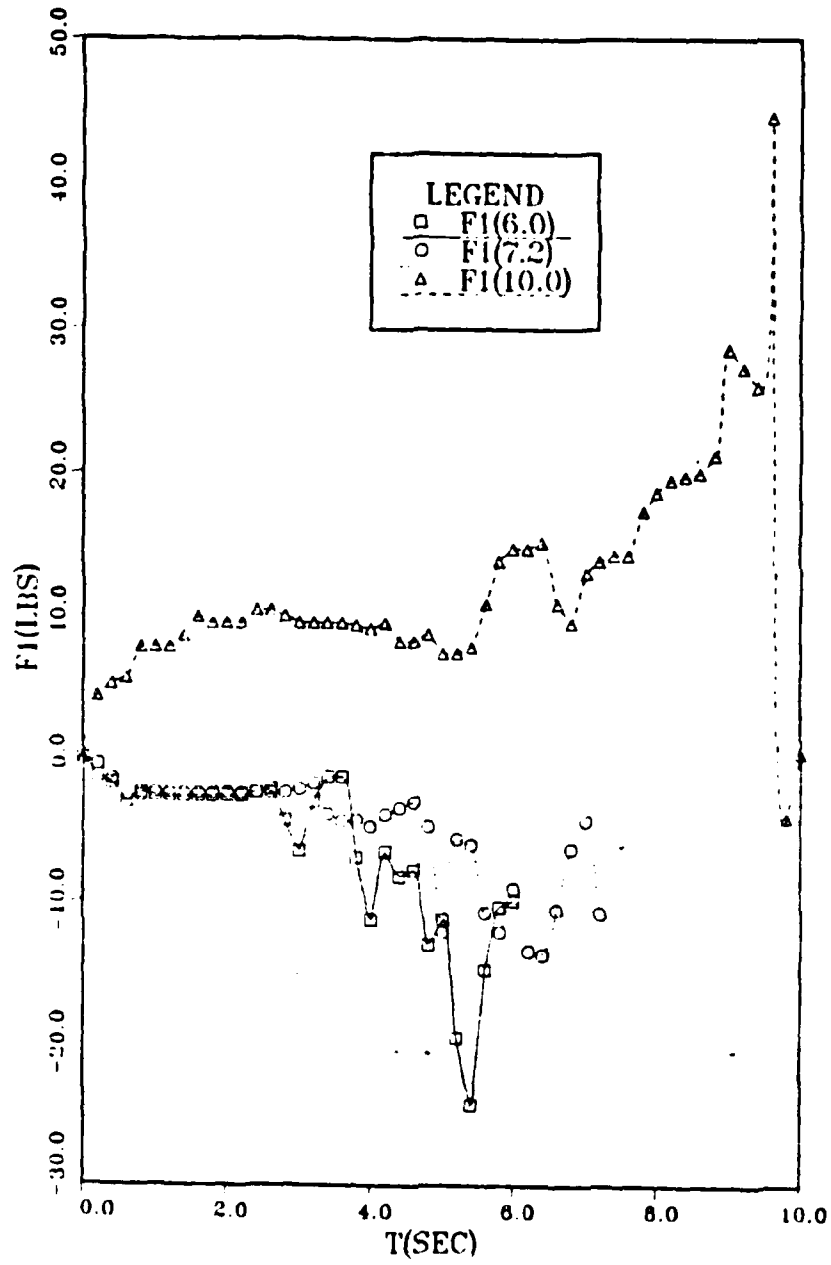
Figure 32.   Drilling Results for F_1 Plot

139

F2: Y AXIS FORCE
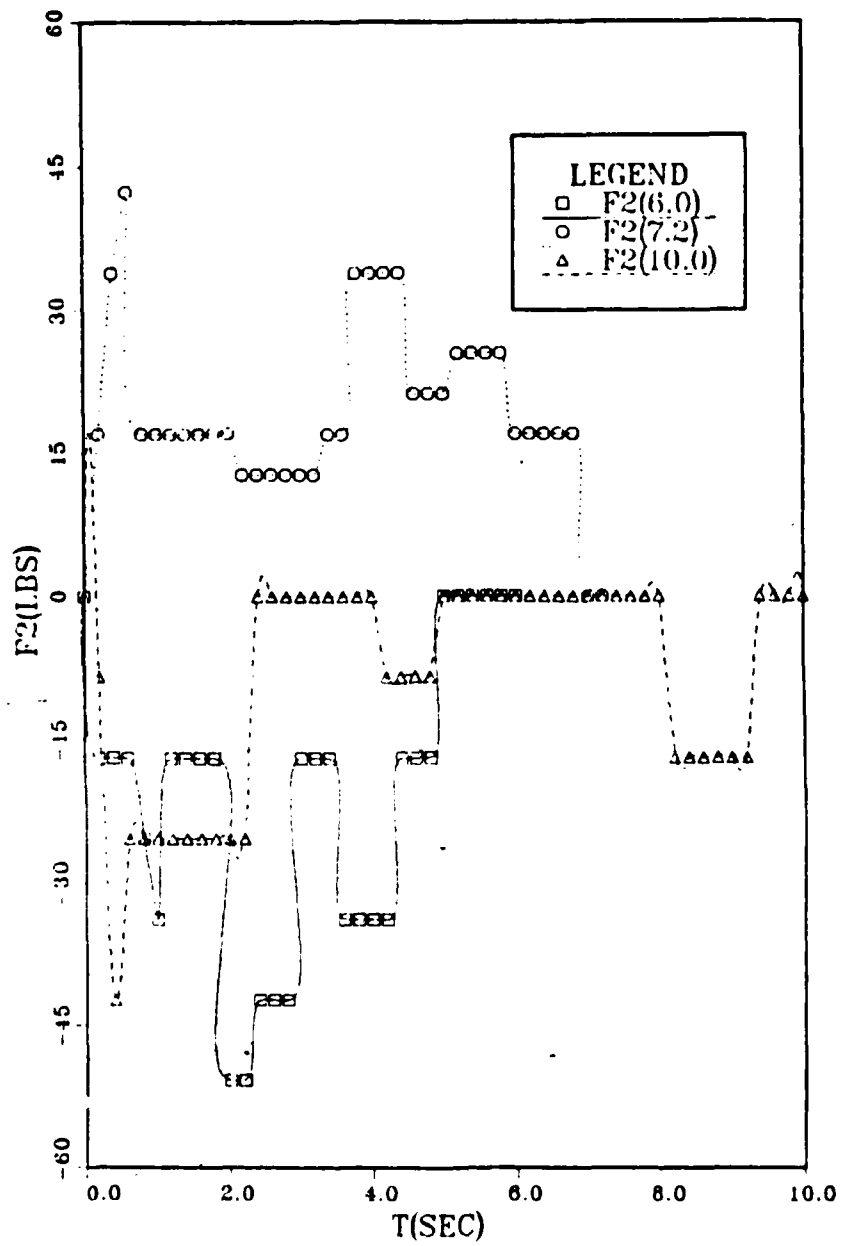
Figure 33.   Drilling Results for F_2 Plot

140

characterized by increasing magnitude as the drill's trailing edge was approached. The F_2 force exhibits sharp, momentary increases in magnitude followed by relatively long periods at constant value.

2. Moments

The direction and magnitude of the moments were coupled to the effects of the transverse load seating conditions. For run 1, the M_1 moment about the X axis was positive with a maximum value of 1137.88 inch-pounds (Figure 34), and for run 2, M_1 was negative with a maximum value of -996.75 inch-pounds. While for run 3, the value of M_1 varied from -37.53 to 1003.91 inch pounds. Each time, the maximum values occured at the beginning of the drilling.

The M_2 moment about the Y axis oscillated between negative and positive values in all three runs (Figure 35). The ranges of values were as follows:

Run 1:   -427.45 to 72.28 inch-pounds

Run 2:   -147.11 to 47.99 inch-pounds

Run 3:   -309.63 to 803.71 inch-pounds

The peak values were at the trailing edge of the drill bit.

The M_3 moments about the Z axis were also oscillatory, but were, for the most part, positive in nature (Figure 36). This positive nature correlates to the fact that binding did not occur for these runs. The range of values obtained were:

M1: X AXIS MOMENT
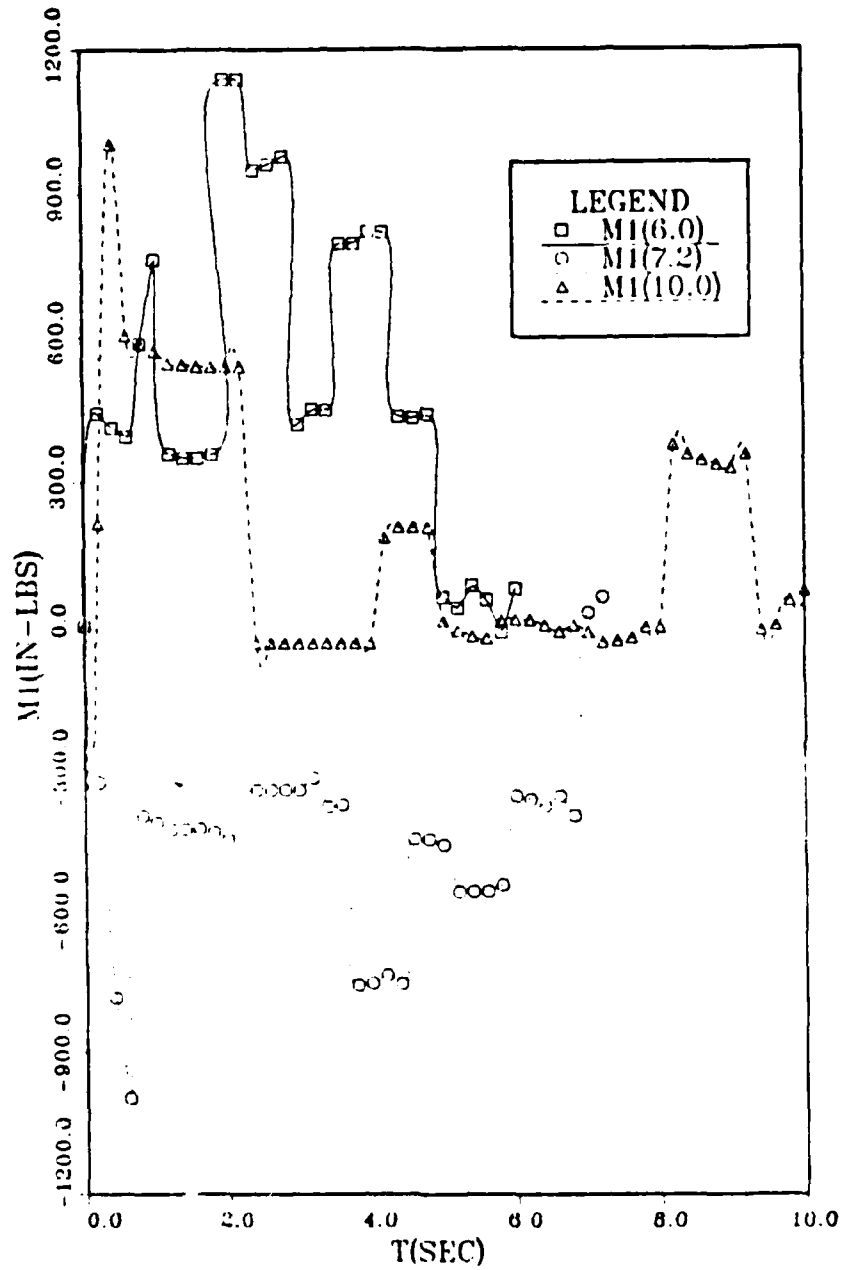
Figure 34. Drilling Results for M_1 Plot

M2: Y AXIS MOMENT
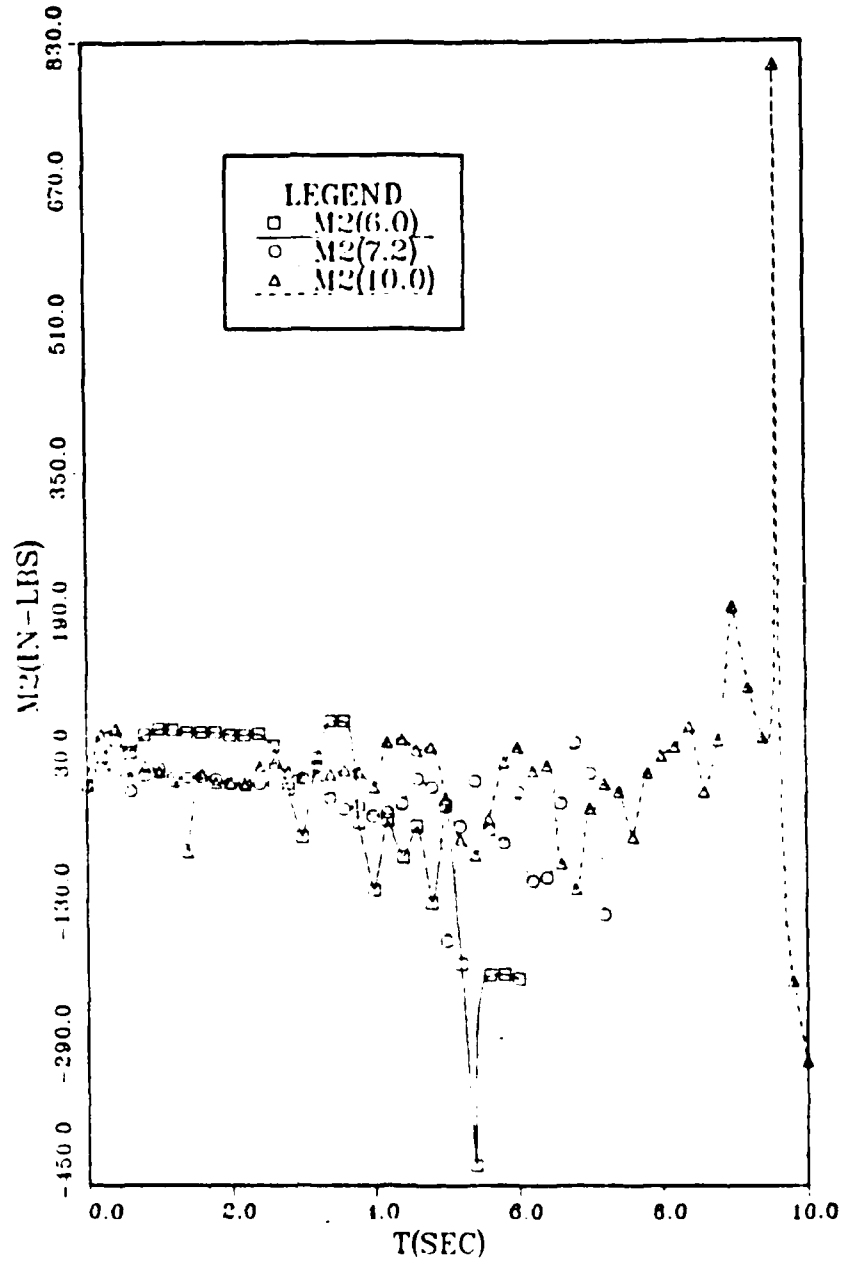
Figure 35.   Drilling Results for M_2 Plot

M3: Z AXIS MOMENT
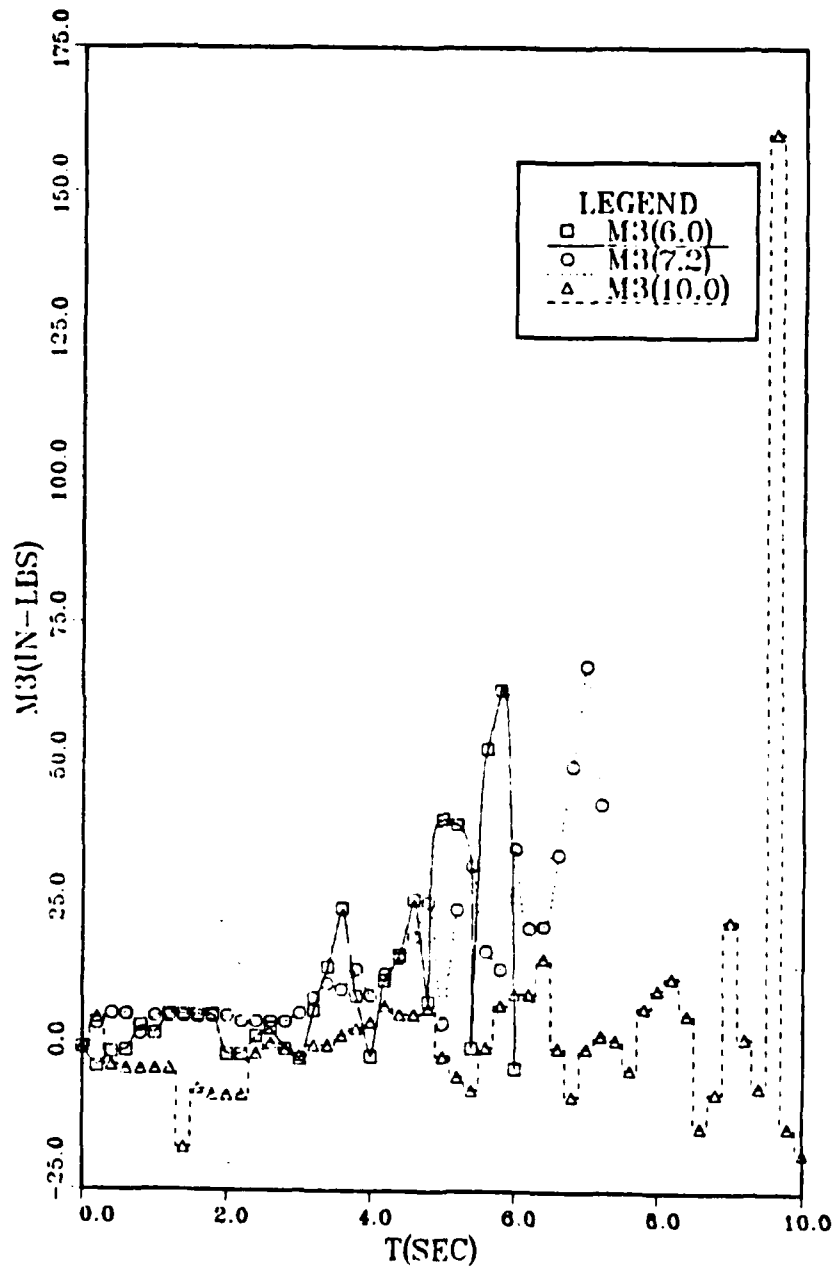
Figure 36. Drilling Results for M_3 Plot

144

Run 1:   -3.37 to 63.23 inch-pounds

Run 2:   0.0 to 67.55 inch-pounds

Run 3:   -18.03 to 160.52 inch-pounds

As with M_2, the peak values were at the drill's trailing edge.

D. COMPARISON WITH PREVIOUS WORK

Figures 37 through 45 are plots which compare the results of this work to the forces/moments computed using the equations of the previous work in Table IV. In the plots, various quantities are differentiated by a PW preceeding values of the previous work. The values of F_3, L_1*F_1, and M_3 correlated fairly well for the two studies and thus complement each other's validity.

The differences in the F_3 force are due mainly to the assumption in the previous work omitting the M_1 and L_1*F_2 bending moments which contribute to the state of strain at point A.

Similarly, the twisting moment at point B is not only a function L_1*F_1 but also the moment M_2 which, depending on its direction, adds or subtracts from L_1*F_1. The normal strain at point B, is not only a function of M_3, but also the bending moment caused by L_2*F_1.

E. ERROR ANALYSIS

For the strip charts, a one-half of a division error equates to the following accuracies for the forces:

145

F3: Z AXIS FORCE (M1=M2=F2=0)
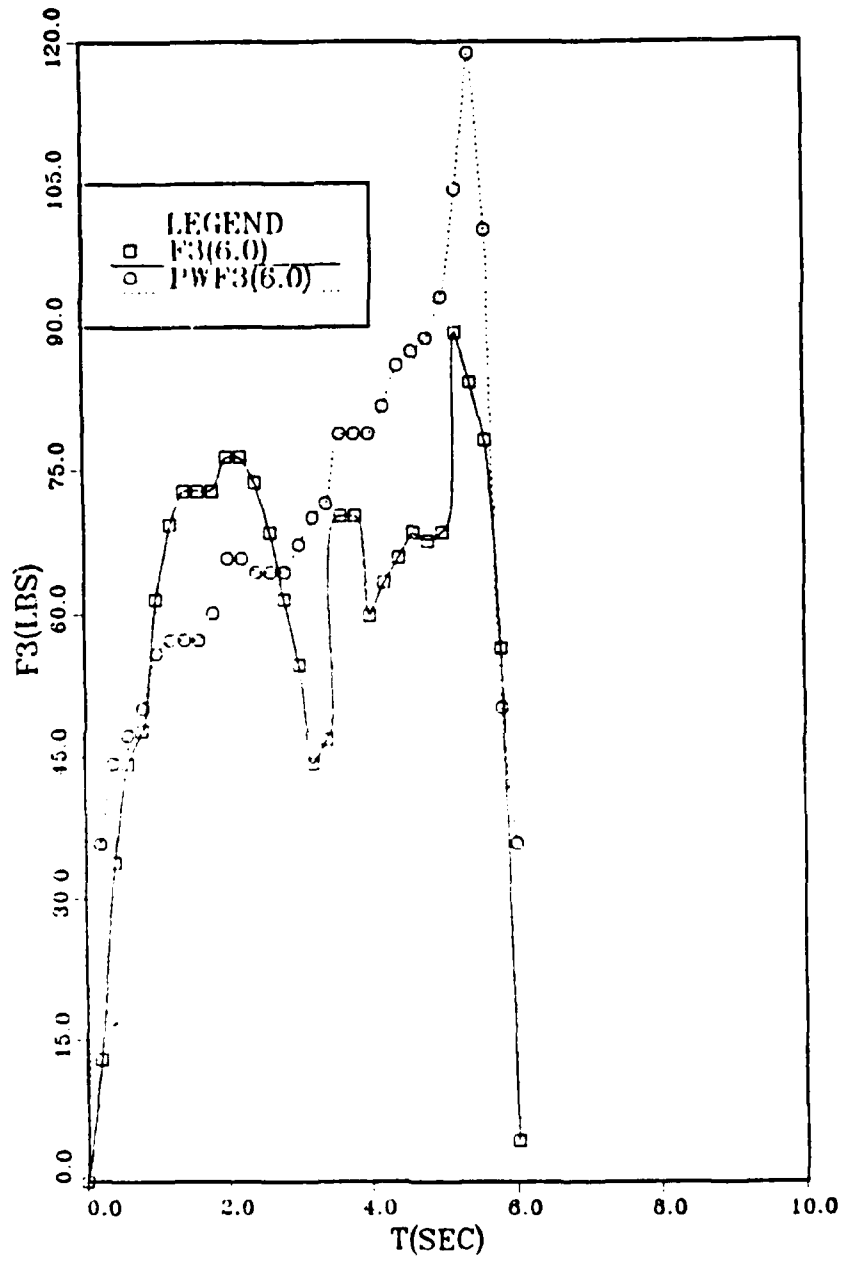
Figure 37.   Current Versus Previous Work: F_3 Plot 1

146

F3: Z AXIS FORCE (M1=M2=F2=0)
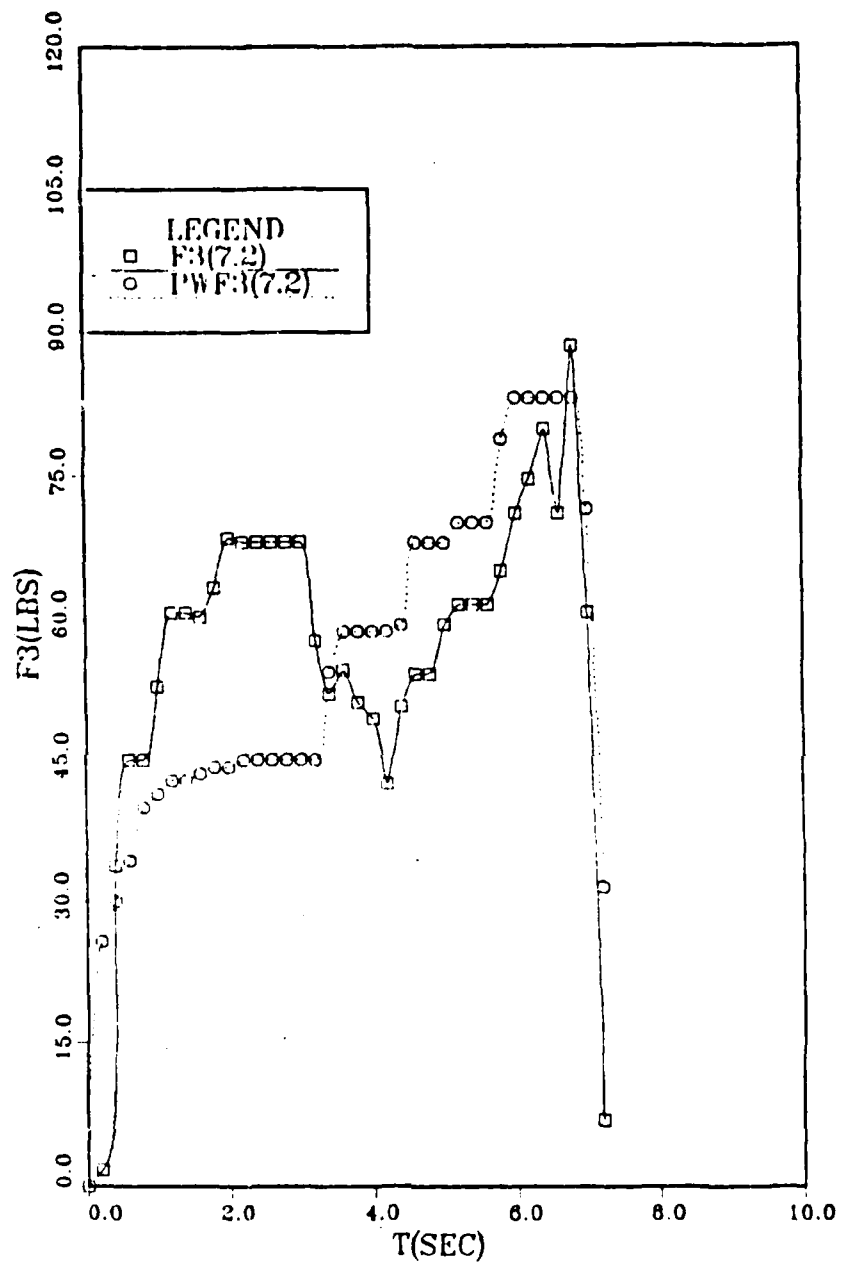
Figure 38.   Current Versus Previous Work: F_3 Plot 2

147

F3: Z AXIS FORCE (M1=M2=F2=0)
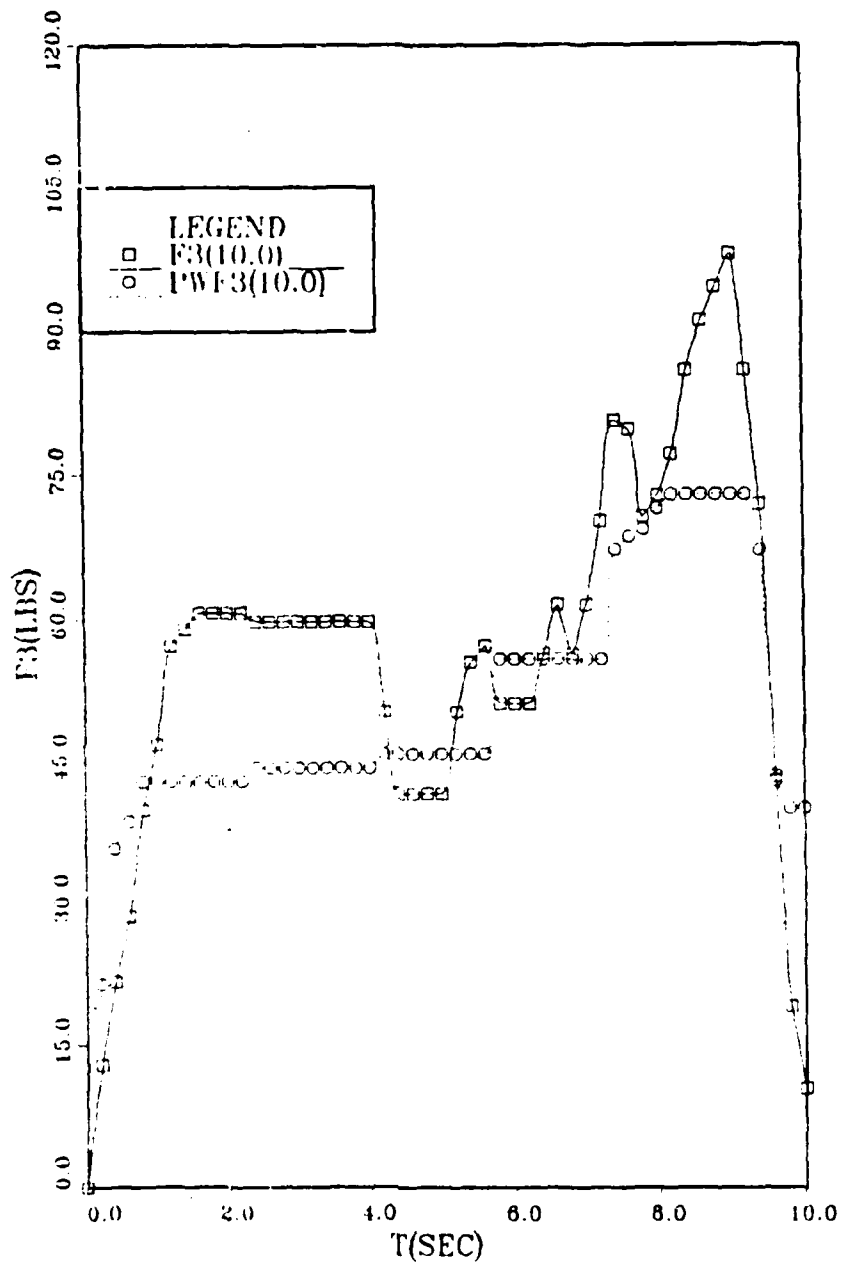
Figure 39. Current Versus Previous Work: F_3 Plot 3

148

L1*F1:Y AXIS MOMENT(M1=M2=F2=0)
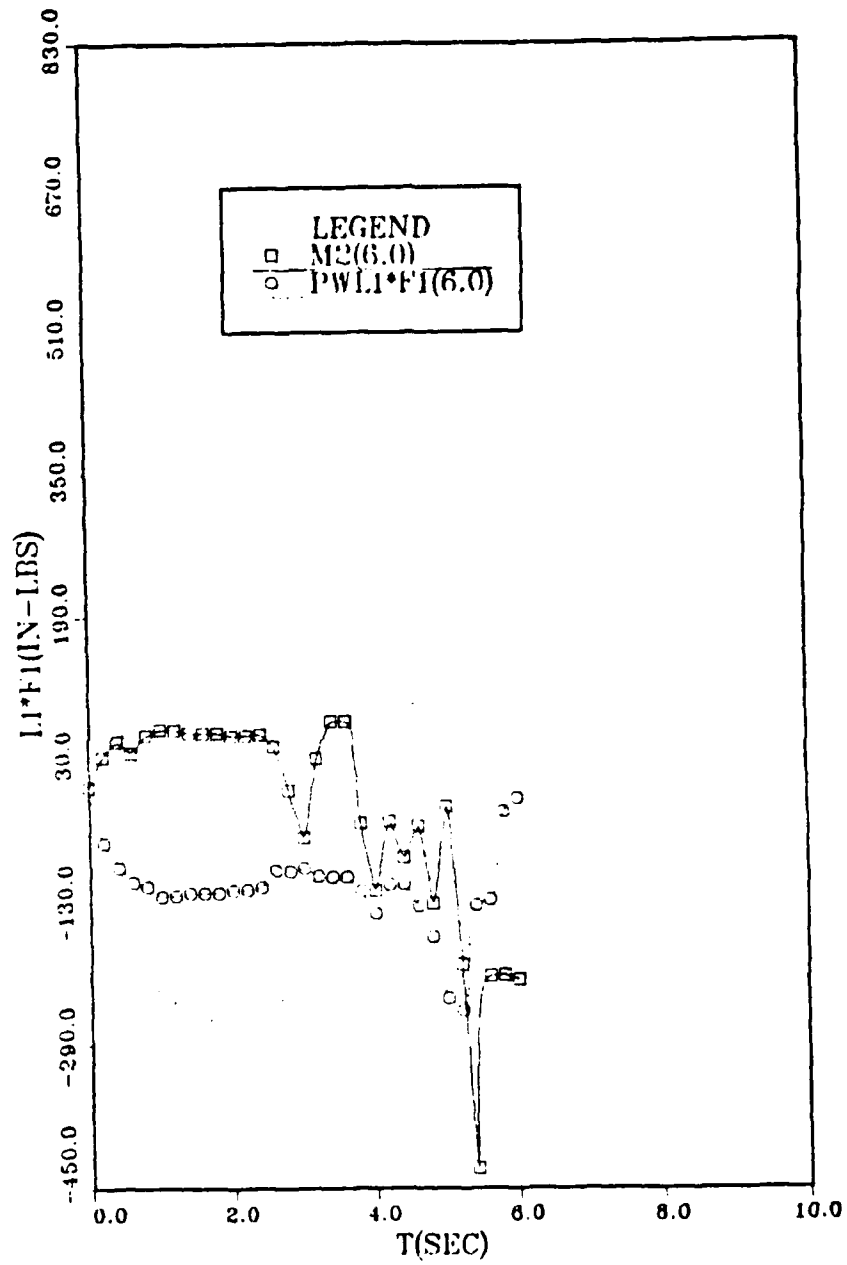
Figure 40. Current Versus Previous Work: M_2 Plot 1

149

L1*F1:Y AXIS MOMENT(M1=M2=F2=0)
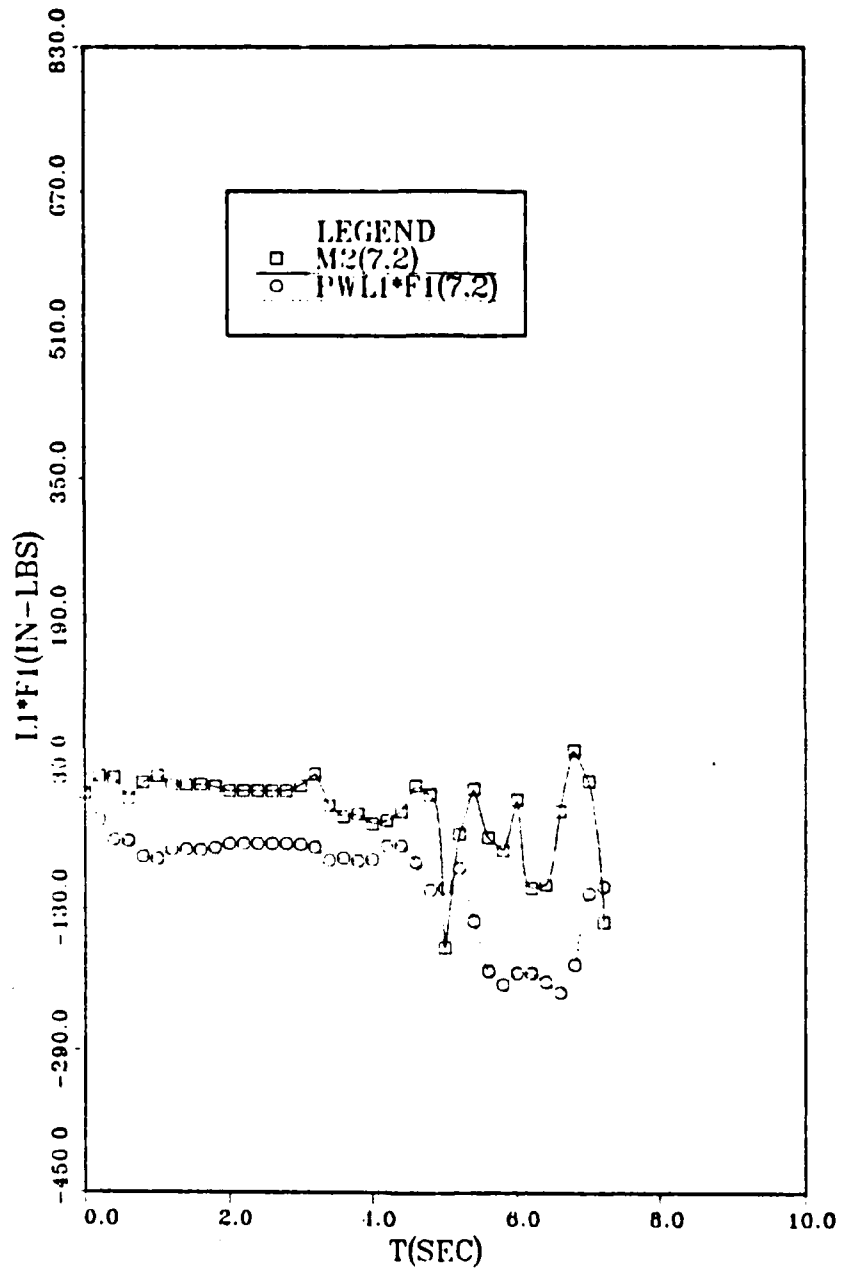
Figure 41. Current Versus Previous Work: M_2 Plot 2
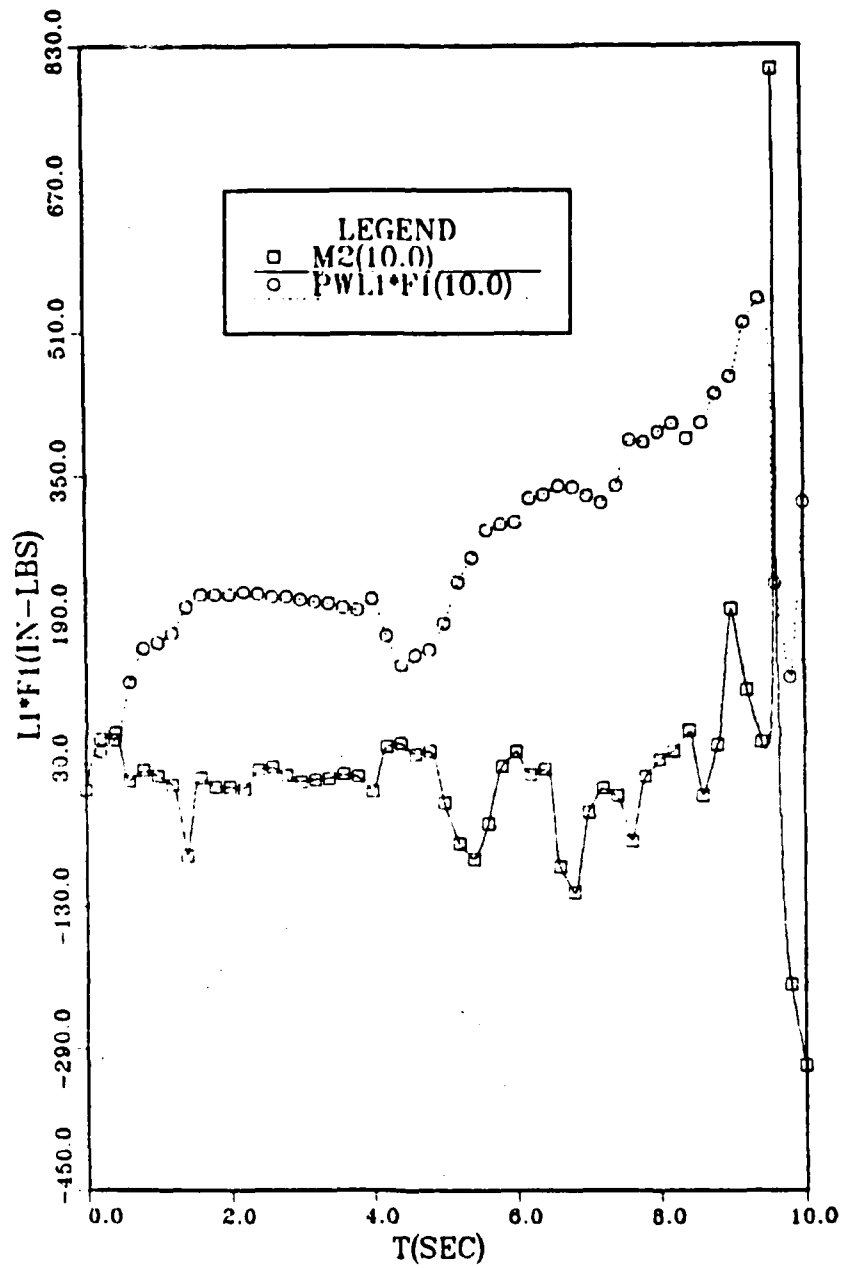
Figure 42.   Current Versus Previous Work: M_2 Plot 3

151

M3: Z AXIS MOMENT(M1=M2=F2=0)
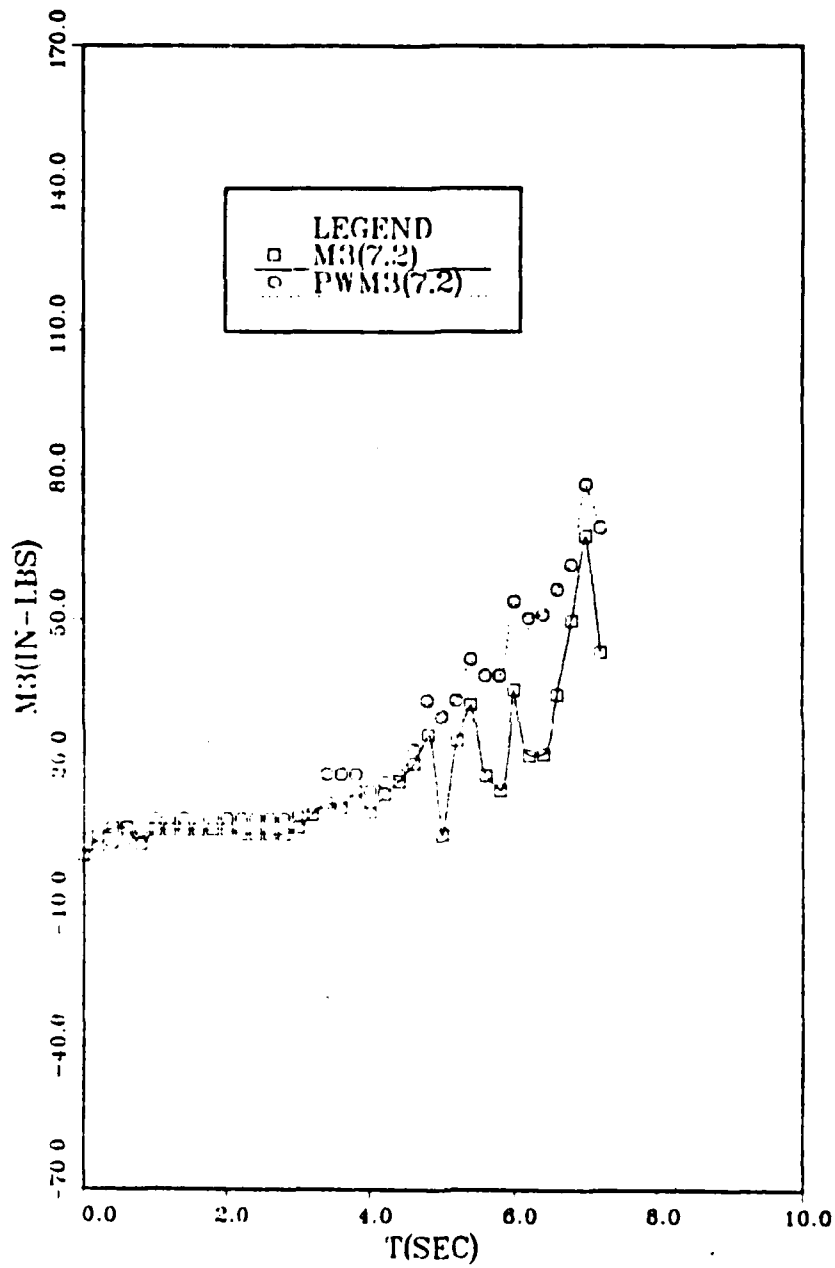
Figure 44.   Current Versus Previous Work: M_3 Plot 2

M3: Z AXIS MOMENT(M1=M2=F2=0)
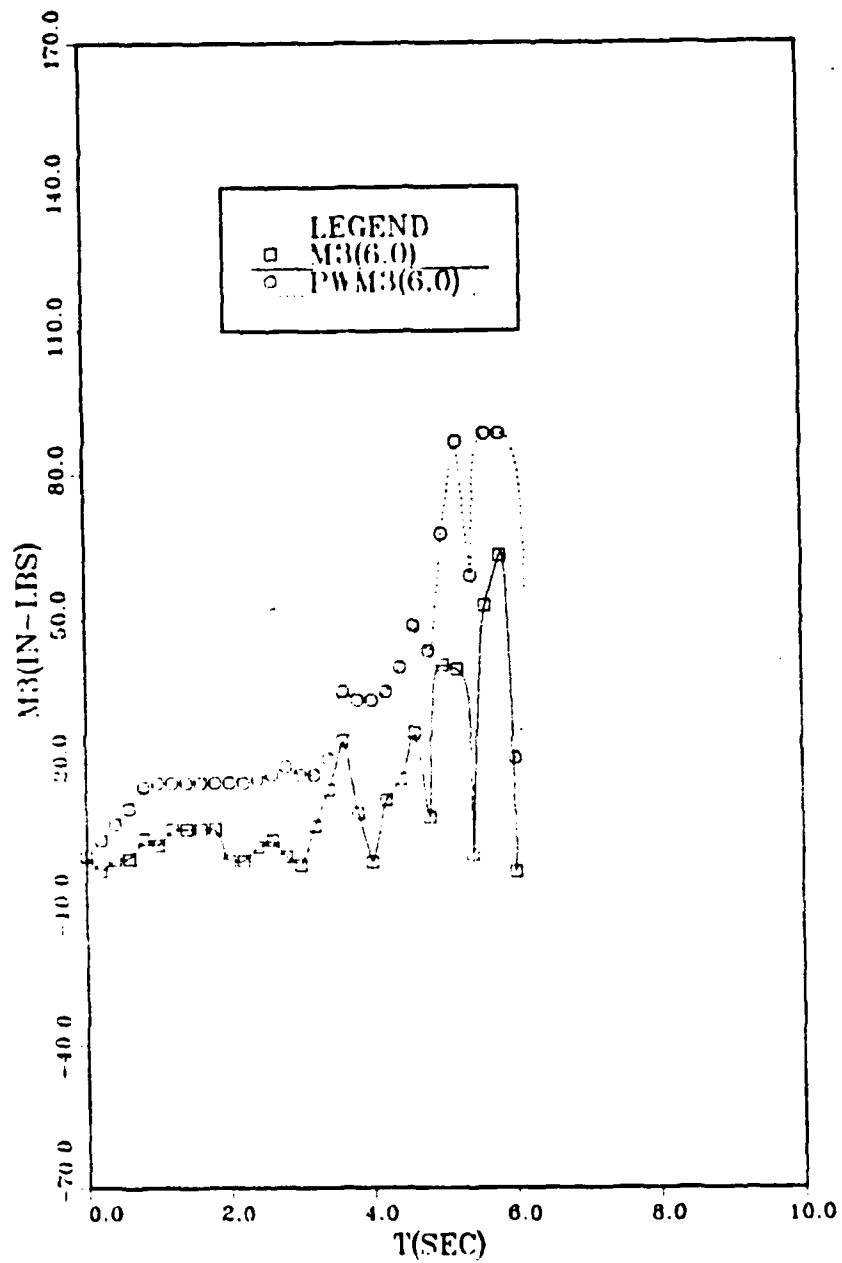
Figure 43.   Current Versus Previous Work: M_3 Plot 1

153

M3: Z AXIS MOMENT(M1=M2=F2=0)
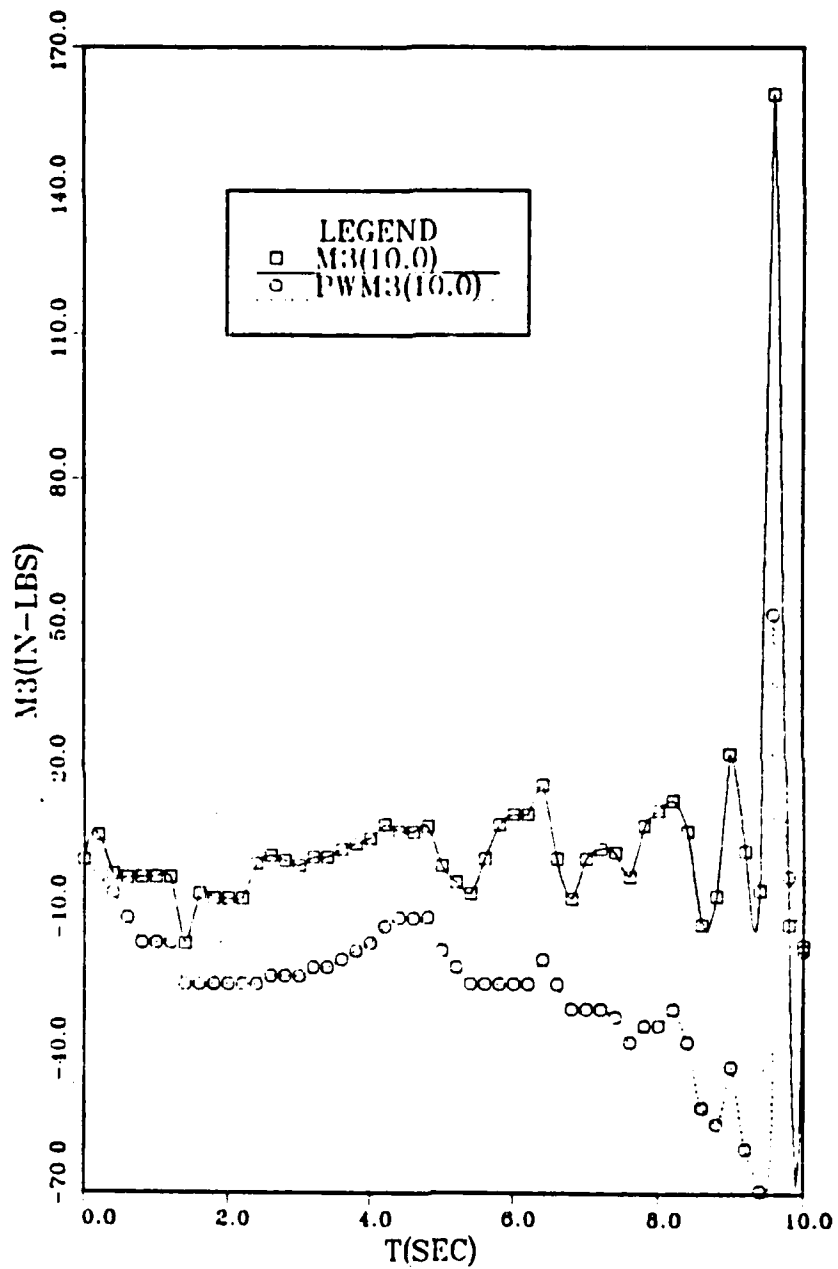
Figure 45.   Current Versus Previous Work: M_3 Plot 3

154

F1:   +/- 2.17 pounds

                    F2:   +/- 42.31 pounds

                    F3:   +/- 8.67 pounds

    The results of the static tests of the equations yielded

the following maximum error percentages for measured versus

calculated values:

                    F1:   +/- 0.4 %

                    F2:   +/- 10.2 %

                    F3:   +/- 1.1 %

V. CONCLUSIONS

An investigation of the requirements for a robot arm to manipulate an aircraft skin penetrator/applicator was conducted. The penetrator was a USAF-developed device which was designed to penetrate the fuselage of an aircraft and inject a gaseous fire fighting agent (Halon) into the interior of the aircraft to extinguish fires. Experiments were designed to identify worst-case drilling loads, and a test apparatus was used to mimic the drilling. Test data were collected on the effects of drilling through sheet aluminum alloy. Forces and moments were measured by strain gages during actual drilling.

The test data indicates that the loads at the drill tip are significantly influenced by drill walking prior to stabilizing and penetrating of the drilling surface. This is attributed to significant transverse load forces (F_1 and F_2) which act in a plane perpendicular to the drill axis. These transverse forces act with the length of the penetrator to exert significant moments on the support structure. Significant factors in the walking phenomenon include: the age and condition of the drill tip; the type of material to be drilled; and the angle of attack between the drill axis and the drilling surface, all of which contribute to the direction and the magnitude of the drill

walking prior to penetration. The drill walking in turn determines the directions and magnitudes of the transient loads.

The following is a summary of the maximum forces and moments for each of the runs recorded:

	Run 1	Run 2	Run 3
F_1 (lbs)	-24.28	-13.66	44.67
F_2 (lbs)	-50.76	42.35	-42.31
F_3 (lbs)	89.34	88.47	98.01
M_1 (in-lbs)	1137.88	-996.75	1003.91
M_2 (in-lbs)	-427.45	-147.11	803.71
M_3 (in-lbs)	63.23	67.55	160.52

From this summary, a negative F_2 results in a positive M_1 moment on the drill tip where the reverse case is true for positive F_2. As for F_1, its direction effects the resulting moment M_2. The direction of M_2 is positive when F_1 is positive and vice versa. With regard to M_3, F_1 is the dominant transverse force, but not to the extent it was for M_2, this is true because the moment arm in the M_3 case is the distance from the centerline of the drill to a point on the support structure which is much less than the length of the penetrator in the M_2 case. But as can be seen above, the magnitude of M_3 is significantly higher for run 3 where a positive F_1 was realized vice the other runs when a negative F_1 resulted from the drill walking.

157

With regard to the previous study of Reference 2, the effects of drill wear are an increased axial force and/or torque requirement. The location and nature of the wear governs which symptom dominates. Chisel edge wear results in increased axial force, land wear results in increased torque, and wear at the corners results in increases of both [Ref. 4]. The thrust (F_3) and torque (M_3) of the previous work for an 8 degree angle of attack were of the magnitudes, respectively, of 280 pounds and 475 inch-pounds for 100 psig supply air, and 205 pounds and 255 inch-pounds for 140 psig supply. Therefore, the combination of the different wear effects discussed above combined with an increase of supply air pressure to 160 psig, would explain the higher thrust and torque required for the worn drill used in the previous study and the lower requirements determined in this study. This was also visually evident in the resulting sharp, clean holes for the current study and the rough, jagged holes drilled with the worn drill. Another contributing factor to the differences in the torque moment, is the fact that the previous study did not deduct the bending effects caused by F_1 times the length from the centerline of the drill to the strain gage location. Similarly, the previous assumption that there was no M_2 at the drill tip, just twisting of the support structure caused by F_1 times the length of the penetrator, disallowed any correlation between the two studies with respect to F_1 and M_2.

VI. <u>RECOMMENDATIONS FOR FUTURE WORK</u>

Further investigation for two specific areas are required. The first is the phenomenon of the drill walking and the resulting effects it has on the drill stabilizing and penetrating. The drill has a possible choice of four quadrants in which to move. These would result from the following combinations of transverse forces:

$$F_1 \text{ and } F_2$$
$$F_1 \text{ and } -F_2$$
$$-F_1 \text{ and } F_2$$
$$-F_1 \text{ and } -F_2$$

Drilling data should be obtained for all the combinations and analyzed for drill support effects and repeatability.

The second area of concern is the life cycle of the penetrator drill. The thrust and torque requirements are both a function of drill wear. In view of the fire fighting mission of the device, a definitive useful life cycle for the drill bit should be identified.

With regard to the experimental procedures, the methodology of this study is sufficient but improved data recording is required for further work. A process for directly converting the continuous time output of the strain gages into an input for the strain-to-load conversion computer program should be developed.

APPENDIX A

STRAIN EQUATIONS FORTRAN COMPUTER CODE

```
**************************************************************************
* LAWRENCE, D.A.
* DRILL1 PROGRAM CLACULATES THE RESULTING STRAINS GIVEN THE APPLIED
* MOMENTS AND FORCES AT THE DRILL TIP.
* VARIABLES USED ARE:
*     TH: RADIAL THICKNESS (IN)
*     RO: OUTSIDE CYLINDER DIAMETER (IN)
*     RI: INSIDE CYLINDER DIAMETER (IN)
*     E: YOUNGS MODULUS OF ELASTICITY (LBS/IN**2)
*     POI: POISON RATIO
*     PI
*     G: SHEAR MODULUS OF ELASTICITY (LBS/IN**2)
*     D: MEAN DIAMETER (IN)
*     L21: DISTANCE FROM CENTERLINE OF DRILL TO STRAIN GAGE (IN)
*     L22: DISTANCE FROM CENTERLINE OF DRILL TO STRAIN GAGE(IN)
*     L1: DISTANCE FROM DRILL TIP TO CYLINDER CENTROID (IN)
*     F1: X AXIS LOAD (LBS)
*     F2: Y AXIS LOAD (LBS)
*     F3: Z AXIS LOAD (LBS)
*     M1: MOMENT LOAD ABOUT X AXIS (IN-LBS)
*     M2: MOMENT LOAD ABOUT Y AXIS (IN-LBS)
*     M3: MOMENT LOAD ABOUT Z AXIS (IN-LBS)
*     EYA21: NORMAL STRAIN AT POINT A DISTANCE L21
*     EYA22: NORMAL STRAIN AT POINT A DISTANCE L22
*     EYB21: NORMAL STRAIN AT POINT B DISTANCE L21
*     EYB22: NORMAL STRAIN AT POINT B DISTANCE L22
*     EYC21: NORMAL STRAIN AT POINT C DISTANCE L21
*     SYZB21: SHEAR STRAIN AT POINT B DISTANCE L21
*     EZB21: NORAML STRAIN AT POINT B DISTANCE L21
*     EYZB21: Y-Z PLANE STRAIN ON 45 DEGREE ROSETTE LEG DISTANCE L21
*     X(I):CONSTANTS INCLUDE I,Q,RO,D,PI,G,E
*     A(I,J): REPEATED CALCULATIONS IN EQUATIONS
**************************************************************************
      DOUBLE PRECISION RO,RI,TH,E,POI,PI,G,D,L21,L22,L1,X1,X2,X3,X4
     + A1,A21,A22,B21,B22,EYA21,EYA22,EYB21,EYB22,EYC21,EYZB21,EZB21,
     + SYZB21,F1,F2,F3,M1,M2,M3,Y1,Y2,Y3
      INTEGER J
*DEFINE KNOWN PARAMETERS
      RO=0.5
      TH=0.1
      RI=RO-TH
      E=29000000.0
      POI=0.29
      PI=4.0*ATAN(1.0)
      G=E/(2.0*(1.0+POI))
      D=(2.0*RO)-TH
      L21=2.424
      L22=6.424
      L1=0.0
*CALCULATE CONSTANT TERMS IN EQUATIONS
      X1=PI*TH*D*E
      X2=4.0*RO/(PI*E*(RO**4-RI**4))
      X3=8.0*(RO**3-RI**3)/(3.0*G*PI*(TH**2)*(D**3))
      X4=G*PI*TH*(D**2)
*INPUT THE LOADS
      DO 10 J=1,4
      READ(14,*) F1,F2,F3,M1,M2,M3
```

160

```fortran
        A1=F2/X1
        A21=-(L21*F3+L1*F2+M1)*X2
        A22=-(L22*F3+L1*F2+M1)*X2
        B21=(L21*F1-M3)*X2
        B22=(L22*F1-M3)*X2
*CALCULATE THE STRAINS
        EYA21=(A21+A1)
        EYA22=(A22+A1)
        EYB21=(B21+A1)
        EYB22=(B22+A1)
        EYC21=(-A21+A1)
        SYZB21=(-2.0*(L1*F1-M2)/X4)+(X3*F3)
        EZB21=-POI*EYB21
        EYZB21=(EYB21+EZB21+SYZB21)/2.0
*PRINT LOADS FOR INPUT TO EASYPLOT

        OPEN(UNIT=21,FILE='DATA1',STATUS='OLD')
        WRITE(21,5)
5       FORMAT(T5,'F1',T13,'F2',T21,'F3',T29,'M1',T37,'M2',T45,'M3'/)
        WRITE(21,15) F1,F2,F3,M1,M2,M3
*PRINT OUTPUTS OF STRAINS AND LOADS
15      FORMAT(6F10.2//)
        WRITE(21,25)
25      FORMAT(T5,'EYA21',T18,'EYA22',/)
        WRITE(21,35)EYA21,EYA22
35      FORMAT(2E12.4/)
        WRITE(21,45)
45      FORMAT(T5,'EYB21',T18,'EYB22',T30,'EYZB21',T42,'EZB21'/)
        WRITE(21,55) EYB21,EYB22,EYZB21,EZB21
55      FORMAT(4E12.4/)
        WRITE(21,65)
65      FORMAT(T5,'EYC21'/)
        WRITE(21,75) EYC21
75      FORMAT(E12.4//72('+')//)
*PRINT STRAINS TO FILE FOR CALIBRATION PLOTS
        EYA21=1000000*EYA21
        EYA22=1000000*EYA22
        EYB21=1000000*EYB21
        EYB22=1000000*EYB22
        EYZB21=1000000*EYZB21
        EZB21=1000000*EZB21
        EYC21=1000000*EYC21
        WRITE(20,*) EYA21,EYA22,EYB21,EYB22,EYZB21,EZB21,EYC21
        Y1=EYB22-EYB21
        Y2=EYA21+EYC21
        Y3=EYA22-EYA21
        OPEN(UNIT=22,FILE='DATA2',STATUS='OLD')
        OPEN(UNIT=24,FILE='DATA3',STATUS='OLD')
        OPEN(UNIT=25,FILE='DATA4',STATUS='OLD')
        WRITE(22,85) F1,Y1
        WRITE(24,85) F2,Y2
        WRITE(25,85)F3,Y3
85      FORMAT(2F10.2)
10      CONTINUE
        STOP
        END
```

161

APPENDIX B

LOAD EQUATIONS FORTRAN COMPUTER CODE

```
***************************************************************************
* LAWRENCE, D.A.
* THIS PROGRAM CALCULATES THE THE LOADS AT THE PENETRATOR DRILL TIP
* BASED ON MICRO-STRAIN INPUTS. ALSO THE PROGRAM CALCULATES THE LOADS
* USING THE ASSUMPTIONS THAT F2,M1,AND M2 ARE ZERO MADE IN THE PREVIOUS
* WORK.
* VARIABLES USED ARE:
*       T:TIME (SEC)
*       TH: RADIAL THICKNESS (IN)
*       RO: OUTSIDE CYLINDER DIAMETER (IN)
*       I: MOMENT OF INERTIA (IN**4)
*       E: YOUNGS MODULUS OF ELASTICITY (LBS/IN**2)
*       POI: POISON RATIO
*       PI
*       G: SHEAR MODULUS OF ELASTICITY (LBS/IN**2)
*       D: MEAN DIAMETER (IN)
*       L21:DISTANCE FROM CENTERLINE OF DRILL TO STRAIN GAGE (IN)
*       L22:DISTANCE FROM CENTERLINE OF DRILL TO STRAIN GAGE (IN)
*       L1:DISTANCE FROM DRILL TIP TO CYLINDER CENTROID (IN)
*       F1: X AXIS LOAD FORCE(LBS)
*       F2: Y AXIS LOAD FORCE(LBS)
*       F3: Z AXIS LOAD FORCE(LBS)
*       M1: MOMENT LOAD ABOUT X AXIS(IN-LBS)
*       M2: MOMENT LOAD ABOUT Y AXIS(IN-LBS)
*       M3: MOMENT LOAD ABOUT Z AXIS(IN-LBS)
*       EYA21: NORMAL STRAIN AT POINT A DISTANCE L21
*       EYA22: NORMAL STRAIN AT POINT A DISTANCE L22
*       EYB21: NORMAL STRAIN AT POINT B DISTANCE L21
*       EYB22: NORMAL STRAIN AT POINT B DISTANCE L22
*       EYC21: NORMAL STRAIN AT POINT C DISTANCE L21
*       SYZB21: SHEAR STRAIN AT POINT B DISTANCE L21
*       EZB21: NORMAL STRAIN AT POINT B DISTANCE L21
*       EYZB21:Y-Z PLANE STRAIN ON 45 DEGREE LEG ROSETTE DISTANCE L21
*       X(I): CONSTANTS INCLUDE I,Q,RO,D,PI,G,E
*       A(I,J):REPEATED CALCULATIONS IN EQUATIONS
*       YF3:F3 LOAD EQUATION OF PREVIOUS WORK (LBS)
*       YM3:M3 LOAD EQUATION OF PREVIOUS WORK (LBS)
*       YM2:M2 LOAD EQUATION OF PREVIOUS WORK (LBS)
***************************************************************************
        DOUBLE PRECISION RO,RI,TH,E,POI,PI,G,D,L21,L22,L1,X1,X2,X3,
     +  A1,A21,A22,B21,B22,EYA21,EYA22,EYB21,EYB22,EYC21,SYZB21,EZB21,
     +  EYZB21,F1,F2,F3,M1,M2,M3,T
        INTEGER J
*DEFINE KNOWN PARAMETERS
        RO=0.5
        TH=0.1
        RI=RO-TH
        E=29000000.0
        POI=0.29
        PI=4.0*ATAN(1.0)
        G=E/(2.0*(1.0+POI))
        D=(2.0*RO)-TH
        L21=2.75
        L22=6.75
        L1=23.125
*CALCULATE CONSTANT TERMS IN EQUATIONS
        X1=PI*TH*D*E
```

```fortran
      X2=4.0*RO/(PI*EX(RO**4-RI**4))
      X3=8.0*(RO**3-RI**3)/(3.0*G*PI*(TH**2)*(D**3))
      X4=G*PI*TH*(D**2)
      T=0.0
      DO 10 J=1,51
*INPUT MICRO-STRAIN VALUES
      READ(8,*) EYA21,EYA22,EYB21,EYB22,EYZB21,EZB21,EYC21
      EYA21=.000001*EYA21
      EYA22=.000001*EYA22
      EYB21=.000001*EYB21
      EYB22=.000001*EYB22
      EYZB21=.000001*EYZB21
      EZB21=.000001*EZB21
      EYC21=.000001*EYC21
*CALCULATE FORCE AND MOMENT LOADS

      F1=(EYB22-EYB21)/(X2*(L22-L21))
      F2=X1*(EYA21+EYC21)/2.0
      F3=(EYA22-EYA21)/(X2*(-L22+L21))
      A1=F2/X1
      A21=(L21*F3+L1*F2)*X2
      A22=(L22*F3+L1*F2)*X2
      B21=-(L21*F1)*X2
      B22=-(L22*F1)*X2
      M1=((A1-EYA21)/X2)-L21*F3-L1*F2
      M3=((A1-EYB21)/X2)+L21*F1
      SYZB21=2.0*EYZB21-EZB21-EYB21
      M2=(X4*(SYZB21-X3*F3)/2.0)+L1*F1
*PRINT LOADS TO FILE FOR INPUT TO EASYPLOT
      WRITE(14,2) T,F1,F2,F3,M1,M2,M3
2     FORMAT(7F10.2)
*CALCULATE LOADS BASED ON PREVIOUS WORK ASSUMPTIONS
      YF3=-EYA21/(X2*L21)
      YM3=-EYB21/X2
      YM2=X4*(X3*F3-SYZB21)/2
*PRINT OLD AND NEW LOADS QUANTITIES TO FILE FOR EASYPLOT
      WRITE(15,3) T,F3,YF3,M2,YM2,M3,YM3
3     FORMAT(7F10.2)
*PRINTED OUTPUT OF STRAINS AND LOADS
      OPEN(UNIT=23,FILE='DATA5',STATUS='OLD')
      WRITE(23,5)
5     FORMAT(T5,'EYA21',T18,'EYA22'/)
      WRITE(23,15) EYA21,EYA22
15    FORMAT(2E12.4/)
      WRITE(23,25)
25    FORMAT(T5,'EYB21',T18,'EYB22',T30,'EYZB21',T42,'EZB21'/)
      WRITE(23,35) EYB21,EYB22,EYZB21,EZB21
35    FORMAT(4E12.4/)
      WRITE(23,45)
45    FORMAT(T5,'EYC21'/)
      WRITE(23,55) EYC21
55    FORMAT(E12.4/)
      WRITE(23,65)
65    FORMAT('T',T5,'F1',T13,'F2',T21,'F3',T29,'M1',T37,'M2',T45,'M3'/
     + 48('*')/)
      WRITE(23,75) T,F1,F2,F3,M1,M2,M3
75    FORMAT(7F10.2/72('+')//)
      T=T+0.2
10    CONTINUE
      STOP
      END
```

LIST OF REFERENCES

1. Naval Air Systems Command: Serial ESL-TR-84-12, _Aircraft Skin Penetrator and Agent Application, Working Model Development and Construction_, Volumes I and II, Final Report, November 1984.

2. Naval Postgraduate School, Monterey, California, _Manipulator Load Forces in a Robot Firefighter_, R.L. Yobbs, April 7, 1986.

3. Gere and Timoshenko, _Mechanics of Materials_, Second Edition, PWS Publishing, 1984.

4. Kaczmarek, J., _Principles of Machining_, Wydawnictwa Naukowo-Techniczne, Warsaw, 1976, pp. 226-250.

Initial Distribution List

165

END

FEb.

1988

DTIC